DANISH METEOROLOGICAL INSTITUTE

SCIENTIFIC REPORT

03-05

Atmospheric Water Vapour Detection using Satellite GPS Profiling

by

Jakob Grove-Rasmussen

Ph.D. thesis 2002

Copenhagen University, Faculty of Science
Niels Bohr Institute for Astronomy, Physics and Geophysics

Study carried out at the Danish Meteorological Institute

COPENHAGEN 2003

ISSN-Nr. 0905-3263
ISSN-Nr. 1399-1949 (Online)
ISBN-Nr. 87-7478-476-5

Contents

Preface

This thesis is based on research done at DMI during the three years from summer 1999 to summer 2002. The study has been carried out supervised by Per Høeg at Danmarks Meteorologiske Institut (Danish Meteorological Institute) and Aksel Walløe Hansen at Københavns Universitet (University of Copenhagen), Niels Bohr Institutet for Astronomi, Fysik og Geofysik, under the Ph.D. school COGCI (COpenhagen Global Change Initiative), financed by Statens Naturvidenskabelige Forskningsråd (National Science Foundation).

Even though, the radio signals from the Global Positioning System for years have been used to probe the Earth's atmosphere both from ground and from space borne receivers, the quality and reliability of the measurements from space are still to be examined. Hence the questions raised in this work regarding water vapour:

- Is the precision of the derived water vapour profiles better than the least of 20% and 1 hPa without bias?
- Is the success rate 100% (all potential occultations being measured)?
- Do all profiles reach the ground?

The answers are partly given by earlier works about temperature and refractivity statistics of the atmosphere, but in this work focus will be on the ability of the method to probe the water vapour in the lower troposphere. Because water vapour is highly variable and causes large gradients in the global atmospheric refractivity field, the questions raised can be extended to search for the occurance of critical gradients in the atmosphere.

The main motivations for measuring water vapour at all are that water vapour is a strong greenhouse gas, which might lead to positive feedback in case of global temperature increase, and water vapour contains large amounts of latent heat, important for the energy budget of the atmosphere. These factors enter issues of both meteorology and climate research, and as water vapour is difficult to measure and a highly variable constituent of the lower atmosphere, the potential of new methods has to be examined.

This thesis is in mainly four parts, starting out with an overview of the radio occultation method and the development of the method to the present stage. Section two is about water vapour as part of the atmosphere, mainly with a climatological perspective. In section three the method and problems involving water vapour

retrieval in specific is examined, with examination of a realistic global refractivity field. Finally section four is concerned with data from the GPS/MET and CHAMP occultation experiments.

Jakob Grove-Rasmussen
E-mail: jgr@dmi.dk

Dansk resume

Jorden omkredses af et system af mindst 24 satellitter som kontinuert udsender radiosignaler ved to frekvenser med en bølgelængde på hhv. 19 cm og 24 cm, fra en højde af 20200 km over jordoverfladen. Systemet hedder Global Positioning System og er etableret af det amerikanske militær. Signalerne benyttes hovedsageligt til positionsbestemmelse ved samtidigt at observere signaler fra mindst fire satellitter således at den rumlige position samt tiden kan beregnes af en modtager. Det har i mange år været kendt af geodæter, at Jordens atmosfære gør positionering unøjagtig da atmosfærens brydningsindeks er en smule større end 1 - i størrelsordenen 300 ppm. Denne unøjagtighed kan tolkes som et alternativt signal der indeholder information om atmosfærens fysiske parametre.

Udstyres en satellit i lav bane omkring Jorden (ca. 700 km) med en GPS-modtager vil forskellen i baneperiode mellem modtageren og GPS satellitterne afstedkomme at radiosignalerne fra tid til anden skærer gennem atmosfæren som tangent til Jorden, optimalt sker dette ca. 500 gange i døgnet pr. modtagersatellit. De indbyrdes hastigheder gør at atmosfæren scannes fra top til bund (eller omvendt) indenfor et til to minutter med typisk 50 samples per sekund. Det radiosignal der modtages kan analyseres for at beregne den ekstra strækning som signalet har tilbagelagt, sammenlignet med hvis atmosfæren ikke havde været tilstede. Denne ekstra strækning kan omregnes til en vinkel som radiosignalet er blevet afbøjet fra start til slut, samt strålens minimale højde over jordoverfladen. Vinklen er ganske lille, maksimalt ca. 1°, men den afstedkommer alligevel en ekstra strækning af op til ≈ 1 km da den totale strækning er af størrelsesordenen 25000 km. Afbøjningsvinklen for et sample indeholder information om brydningsindekset i alle atmosfærelag over den laveste strålehøjde, således at brydningsindekset kan beregnes ved at foretage en Abel transform af hele afbøjningsvinkel profilen.

Brydningsindekset er i atmosfæren, for mikrobølger, en funktion af tryk, temperatur og vanddamptryk - samt bidrag fra ionosfæren og div. partikler i atmosfæren. Ionosfærebidraget kan korrigeres da det er frekvensafhængigt og der måles ved to frekvenser i GPS systemet. Ved anvendelse af relationen for refraktivitet i sin tørre version kan en temperaturprofil beregnes ved antagelse af idealgas ligningen samt hydrostatisk ligevægt. Denne temperatur er således kun fysisk relevant i højder uden vanddamp, mens den i højder med vanddamp undervurderer temperaturen. Størrelsen af undervurderingen (som kan estimeres udfra f.eks. en tilsvarende profil fra en vejrmodel) er et mål for mængden af vanddamp, og den reelle mængde kan beregnes enten iterativt ved at antage at vejrmodel-temperaturen er helt sand, eller alternativt ved at assimilere okkultationsmålingerne i en model og bagefter trække vanddampmængden ud af modellen.

Okkultationsmetoden er et glimrende supplement til eksisterende meteorologiske målinger da en passende modtager er relativt lille og billig, og målingerne er relateret til tid og ikke signalstyrker, hvilket gør dem meget præcise og stabile over lang tid samt mellem forskellige instrumenter. Desuden gennemtrænger mikrobølger skyer og regn på grund af den relativt store bølgelængde, og der er global dækning.

Vanddamp er en ofte miskendt bestanddel af Jordens atmosfære da det ikke kan ses, og sjældent omtales i den offentlige klimadebat. Men vanddamps indflydelse på energiregnskabet og dynamikken i atmosfæren er stor - af flere årsager. Vanddamp er bl.a. en yderst kraftig drivhusgas. Dette betyder at den er medvirkende til at opretholde en menneskevenlig temperatur på Jordens overflade ved at holde på den infrarøde varmestråling fra Jorden, men der er også potentiale for en positiv feedback da en øget temperatur øger fordampningen og den mængde vanddamp der kan være i atmosfæren. Desuden indeholder vanddamp latent varme fra fordampningen. Denne energi kan således flyttes rundt i atmosfæren og frigøres til kinetisk energi ved kondensation ved f.eks. skydannelse. Kunne al vanddamp i atmosfæren kondenseres ville det blive til et globalt dække af 2,5 cm tykkelse, hvilket er forsvindende i forhold til oceanernes vandmængde som tilsvarende ville resultere i et globalt dække i kilometer-tykkelse. Tidsskalaen for variationer i vanddampfordelingen er meget kort, i gennemsnit 'udskiftes' al vanddamp i atmosfæren hver niende dag.

Denne afhandling gennemgår baggrunden for inversionen af GPS okkultationsdata helt frem til vanddamp-profiler, med illustrerende eksempler på profiler i de forskellige processeringstrin. Inversionen er anvendt på observationsperioder fra det amerikanske GPS/MET eksperiment (det første eksempel på anvendelse af GPS okkultationsteknikken) og den tyske CHAMP satellit. Data analyseres for de geometriske forhold vedrørende den globale fordeling samt dybden profilerne når ned i atmosfæren. Præcissionen af temperatur- og fugtighedsprofilerne beregnes relativt til en global vejrmodel. Desuden analyseres et globalt refraktivitetsfelt dannet udfra en global vejrmodel. Feltet undersøges for optiske fænomener med relevans for okkultationsmålinger i forbindelse med kraftige vertikale gradienter. Til slut omtales områder indenfor forskningen i metoden, hvor der stadig er potentiale for udvikling.

Chapter 1

Radio occultation principle

1.1 Occultation and GPS

The basic principle behind occultation measurements, is that an atmosphere acts as an optical device with an altitude dependent refractive index, n. Indirect observations of n can be inverted to the atmospheric properties, density, pressure, temperature and the amount of water vapour.

As electromagnetic radiation passes through the atmosphere from a transmitter to a receiver, the - non-unity - refractive index of the air slows the signal, and the gradient of the refractive index affects the direction of the radiation. Knowing the exact position of the transmitter and receiver enables calculation of the refraction* of the signal as function of height. This can be inverted e.g. through the Abel † transform to an expression for the refractive index as function of height. Using an equation relating the refractive index, temperature and pressure, and assuming the ideal gas equation and hydrostatic equilibrium, profiles of the meteorological parameters density, pressure and temperature can be derived. Furthermore the amount of water vapour in the atmosphere can be determined if additional information is used, e.g. knowledge of the temperature from numerical weather models. Alternatively, the amount of water vapour in the atmosphere can be determined from models via assimilation of occultation measurements into an atmospheric model.

In principle the same refraction phenomenon is experienced with the GPS radio waves as with the sunlight at sunset: when we see the Sun set, it is already below the horizon if a pure geometric consideration is made, because of the optical properties of the atmosphere we can look below the horizon. Furthermore, the shape of the Sun is distorted due to irregularities in the atmosphere - correspondingly, distortions of the GPS signals are observed.

*In the geometric optical approach the refraction is analogous to the bending of the rays

†Niels Henrik Abel, August 5th 1802 - April 6th 1829. Norwegian mathematician

Since the early planetary missions, the ability of inverting limb soundings, which is also referred to as occultations, of planetary atmospheres and rings has been refined. The occultation method is one of the only methods of obtaining profiles of the atmosphere of the planets with a high vertical resolution without landing probes. The very first limb soundings were made as observations of stars fading as they were occulted by planets (e.g. (Elliot, 1979)). This occurs on regular basis and is still observed. In stellar occultations the amplitude (strength) of the signal is measured, whereas in the GPS radio occultation method the phase of the signal is the main measurable[‡].

The first such radio occultation measurement was performed on Venus (Fjeldbo et al., 1971; Lipa and Tyler, 1979) and later on the other planets Mars (Kliore et al., 1972), Jupiter (Hinson and Tyler, 1982), Saturn (Lindal et al., 1985) and its rings (Marouf et al., 1986), Uranus (Lindal et al., 1987) and Neptune (Tyler et al., 1989; Lindal, 1992) and its moon Triton (Tyler et al., 1989), with only the planets Mercury, Pluto, Earth remaining along with many moons. More recently a larger number of occultation measurements have been performed on Mars by Mars Global Surveyor (Hinson et al., 1999; Hinson et al., 2001). These measurements revealed atmospheric waves, CO_2-condensation at the North-pole along with estimates of winds and other meteorological phenomena.

Besides the atmospheric measurements from occultations, also gravitational parameters and geometric dimensions of the planets can be determined by the measurements (Eshleman et al., 1977).

All in all the radio occultation method has given a vast amount of information on planetary atmospheres, sizes, shapes and masses.

The occultation method used at the planetary missions was realized to be applicable to Earth with the establishment of the Global Positioning System (GPS) (Parkinson and Spilker, 1996). The GPS consists of (at least) 24 satellites, operated by the American military, continuously transmitting radio signals enabling position determination to within ≈ 10 m with of-the-shelf receivers and within centimetres for advanced receivers. The signals are transmitted at two frequencies ($L_1 = 1.57542$ GHz and $L_2 = 1.2276$ GHz, roughly corresponding to wavelengths of 19 cm and 24 cm), and carry coded information on satellite identification, time, position and status for each satellite, along with parameters for a simple ionospheric model used for correction of the signals. Several codings are used: the civil C/A

[‡]The complex signal, i.e. both phase and amplitude, is measured, but so far most inversions have made use of only the phase data, see e.g. (Sokolovskiy, 2000).

(coarse acquisition) which is on L_1 and well known, the P1 on L_1 which is military (i.e. not available for civil users) and P2 on L_2 which is also military. In order to determine the position of a receiver (which is the main objective of the GPS) four or more satellites have to be observed simultaneously in order to constrain both position (three degrees of freedom) and time (one degree of freedom). The 24 GPS satellites are arranged in six orbital planes with an inclination of 55°. This orbit configuration insures that at all time at least four (and often many more) satellites are visible within 2π sr at any position on Earth. As a result the receiver position can always be determined (if there is open sky view). Fortunately the GPS signals are emitted at so wide angles that even satellites can make use of them. This is widely used for orbit determination.

In January 1999 a third civil frequency was decided to enter the GPS system, being $L_5 = 1.17645$ GHz ($\lambda_5 = 25.5$ cm) with just a little longer wavelength than L_1 (Dierendonck and Hegarty, 2000). This frequency is added to the system with the next satellite generation, called Block IIF planned for launch from 2005.

The standard retrieval of atmospheric parameters is basically as outlined above, only does the atmosphere of the Earth often contain a significant amount of water vapour below the tropopause. As water vapour makes large contributions to the refractive index, the inversion is complicated by the ambiguity expressed in equation 1.8 between the partial pressure of the moist and dry atmosphere and the temperature. This ambiguity is often solved by using additional temperature information from a global weather model (e.g. from ECMWF - European Centre for Medium-range Weather Forecast), enabling retrieval of the two partial pressures. Further details are found in sect. 1.1.4.

Meteorological measurements from the GPS radio signals are not only obtained in an occultation setup with the receiver in orbit. Also ground based GPS receivers play an important role as they are cheaper and easier to maintain. Furthermore, the meteorological product is an additional benefit from receivers anyway installed for geologic/geodetic measurements. Unfortunately ground based receivers only deliver integrated values of the atmosphere between the GPS satellite and the receiver, but combining large numbers of line-of-sight measurements through a tomographic inversion (see e.g. section 3.4) enables mapping.

The phase refractive index n of a medium is defined as:

$$n \equiv \frac{c}{v}$$

where $c \equiv 2.99792458 \cdot 10^8$ m s^{-1} is the speed of light in vacuum, and v the speed

of the phase of electromagnetic waves in the medium.

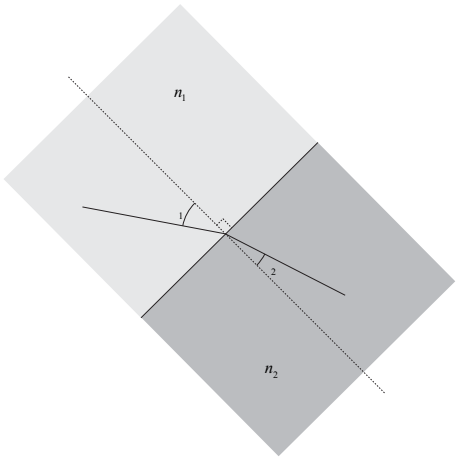

Figure 1.1: Ray-path through an interface between two media of different refractive index n_1 and n_2. The ray is symbolised by the solid line and the normal to the interface by the dashed line. In this example $n_1 > n_2$.

As the refractive index n for atmospheric air is very close to unity, the more convenient term 'refractivity' N is often used:

$$N \equiv 10^6(n-1)$$

For the Earth's atmosphere this results in values between 0 and 450 (see figure 1.6), with the high values close to ground because of the approximate exponential growth of air density towards the ground.

Electromagnetic radiation passing from a medium with refractive index n_1 to a medium with refractive index n_2 changes direction as stated by Snell's law[§]: $n_1 \sin\theta_1 = n_2 \sin\theta_2$, where the θ's are the angles relative to the interface-normal (see fig. 1.1 for illustration of the simple case). The expression can be generalised to an infinite number of spherical symmetric interfaces, changing Snell's law into Bouguer's formula[¶]:

$$nr \sin\theta = \text{const}$$

r is the distance from the centre of symmetry. The law states that a ray path is confined to maintain this constant when passing through media interfaces.

Below the three atmospheric main contributors to the signal changes are reviewed, i.e. the ionosphere, the neutral atmosphere consisting of both a dry contribution and a water vapour contribution. Focus will be on the neutral constituents,

[§]Willebrord van Roijen Snell, 1580 - October 30th 1626. Dutch mathematician.

[¶]Pierre Bouguer, February 16th 1698 - August 15th 1758. French mathematician, appointed his first professorship at the age of fifteen.

assuming that the ionosphere is properly corrected for. This assumption is reasonable as temperature errors at large heights resulting from non-complete ionospheric correction are damped exponentially downward (e.g. (Steiner, 1998)). Temperature errors at low heights from non-complete ionospheric correction are small as the ionospheric residual refractivity is small compared to the neutral refractivity at low heights.

1.1.1 Geometry

In the following the geometrical optics approach is applied. This approach implies that changes in the medium are on scales much larger than the probing (GPS) wavelength. This is valid as the majority of atmospheric phenomena is on (at least) kilometre-scale, only water vapour irregularities reaching into and below the hekto-meter regime through turbulence. Because of the general behaviour of rays in a spherical symmetric medium with increasing refractive index inwards (Born and Wolf, 1980), the geometry of the occultation is as in figure 1.2, with the rays bending towards the centre of symmetry. The illustration is of the geometry in the occultation plane, i.e. the plane defined by the centre of the Earth and the position of the receiver and the transmitter. The transmitter is to the left at velocity $\vec{v}_T$ and the receiver to the right with velocity $\vec{v}_R$, and respective distances r_T and r_R to the centre of curvature (to a first approximation the centre of the Earth). The angles θ_T and θ_R are between the radius vectors and the transmitted/received ray directions, γ the angle between the two radius vectors, and α the bending of the ray or the change in the ray direction vector. a is the perpendicular ray distance - the impact parameter - and r the tangent point height.

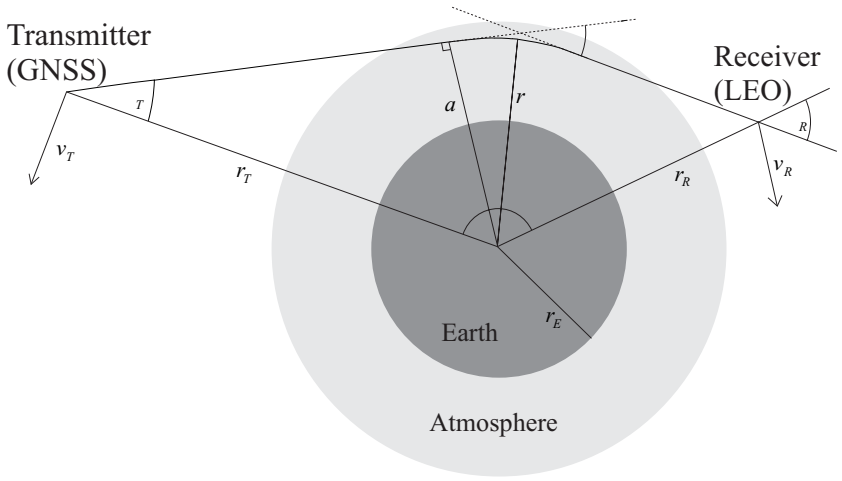

Figure 1.2: The occultation geometry projected onto the occultation plane. For description of signatures, see text.

All the contributions are assumed to be in the occultation plane, indicating that there are no variations perpendicular to the occultation plane (meaning no horizontal gradients). This assumption is not always valid as many atmospheric phenomena such as fronts (Kuo et al., 1998) and high/low pressure areas results in horizontal pressure gradients (Belloul and Hauchecorne, 1997; Ahmad and Tyler, 1999; Healy, 2001).

That the rays tend to bend towards the centre of symmetry results in the altitude of the tangent point can be negative if the straight line calculation is made, as indicated in (Sokolovskiy, 2001).

Along each ray the Doppler[‖] frequency shift Δf is depending upon the projected velocity vector $\vec{v}$ onto the ray direction (unit) vector $\mathbf{u}$. The arrow notation is for the entire vector and bold notation for corresponding unit vector. With subscripts T for transmitter and R for receiver the frequency shift is expressed as (Gorbunov and Sokolovskiy, 1993):

$$\Delta f/f = \Delta v/c = (\vec{v}_T \cdot \mathbf{u}_T + \vec{v}_R \cdot \mathbf{u}_R)/c$$

or in scalar notation with velocities and ray directions resolved into tangential and radial components (respective superscripts ϕ and r) :

$$\frac{\Delta f}{f} c = v_T^r \cos\theta_T + v_T^\phi \sin\theta_T + v_R^r \cos\theta_R - v_R^\phi \sin\theta_R \tag{1.1}$$

From geometric consideration of the relation between the numeric values of ray bending, α, ray directions, θ_T and θ_R and angle between transmitter and receiver γ, it can be established that:

$$\alpha = \gamma + \theta_T + \theta_R - \pi \tag{1.2}$$

as the angle opposite to γ is $\gamma' = \pi - \alpha$ and in general $\gamma + \theta_R + \theta_T + \gamma' = 2\pi$.
From the three equations 1.1, 1.2 and Bouguer's formula and measurement of

1. the excess phase (see below)

2. velocities

3. positions

the bending angle α can be derived as function of impact height a for each ray and each frequency (see figure 1.3).

[‖]Christian Andreas Doppler, November 29th 1803 - March 17th 1855. Austrian mathematician.

The excess phase is the difference in signal path length caused by neutral atmosphere and ionosphere:

$$\Delta L = L_{measured} - L_{straight-line-vacuum}$$

A profile of excess phase for L_1 is seen in figure 1.4.

The excess Doppler shift is expressed either as a frequency shift Δf or as a time derivative of the excess phase path ΔL, i.e. $\dot{\Delta L}$. They are related as:

$$\frac{\Delta f}{f} = \frac{1}{c}\frac{d(\Delta L)}{dt} = \frac{\dot{\Delta L}}{c}$$

In this case the atmospheric effect is measured in Hertz as compared to meters. As only constants of nature is involved in the conversion, it can be stated for the general case as 1 m s^{-1} $\sim$ 5.25 Hz for L_1 and 1 m s^{-1} $\sim$ 4.09 Hz for L_2. The excess Doppler shift is no real Doppler shift, but the pure contribution by the atmosphere as all effects of velocities and clock-errors are removed from the received signals (for details see (Hocke, 1997; Gorbunov and Sokolovskiy, 1993)). An example of an excess Doppler shift profile is in figure 1.4.

The bending angle α is in (Fjeldbo et al., 1971) expressed as:

$$\alpha = \alpha(a_0) = 2\int_{a_0}^{\infty} d\alpha = 2a_0 \int_{a_0}^{\infty} \frac{d\ln(n)}{da}\frac{1}{\sqrt{a^2 - a_0^2}}da \tag{1.3}$$

with $a = rn$ being the impact height and a_0 the smallest impact height of the ray, indicating a smallest ray height of $r_0 = a_0/n(a_0)$. The second equality is based on the assumption of symmetry around the tangent point, and the third on the spherical symmetric geometry.

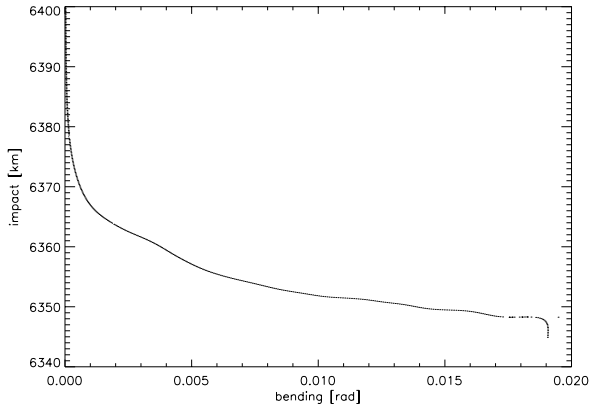

Figure 1.3: Bending angle profile from GPS/MET occultation 458 on February 9th 1997 (tangent point located at 13S, 141W).

Equation 1.3 can mathematically be inverted by the Abel transformation to give the index of refraction as function of impact height a assuming local spherical symmetry:

$$\ln(n(a_0)) = \pi^{-1} \int_{a_0}^{\infty} \frac{\alpha(a)}{\sqrt{a^2 - a_0^2}} da. \tag{1.4}$$

An example of a profile resulting from such an inversion is shown in figure 1.5.

Now, given excess phase and geometry during an occultation, a profile of the index of refraction can be derived as function of height e.g. above a standard ellipsoid or geoide. For meteorological use the heights can be transformed into geopotentiel heights as in (Leroy, 1997). Complications arise due to the oblateness of the Earth, but it can be solved geometrically (Syndergaard, 1998).

The geometry of the involved orbits (transmitter and receiver) determines the global pattern of occultations. Selecting a specific orbit can probe a certain region many times (Yan et al., 1999) if required.

In reality an occultation rarely is in the same plane throughout the occultation, resulting in drift of the tangent point. The definition of the position of the retrieved profile hence can be done in several ways. In this study the profile position is defined to be the position of the tangent point for the last straight line connecting GPS and low Earth orbit (LEO) satellite without penetrating the Earth, as this is where most of the bending takes place and hence most information is contained, especially when considering the water vapour. Other definitions of the profile position could e.g. be an average over the entire occultation or the tangent point of the lowest occultation sample. Or the position could be calculated for each altitude in the profile. This last approach could seem most correct, but as many inversion techniques assume

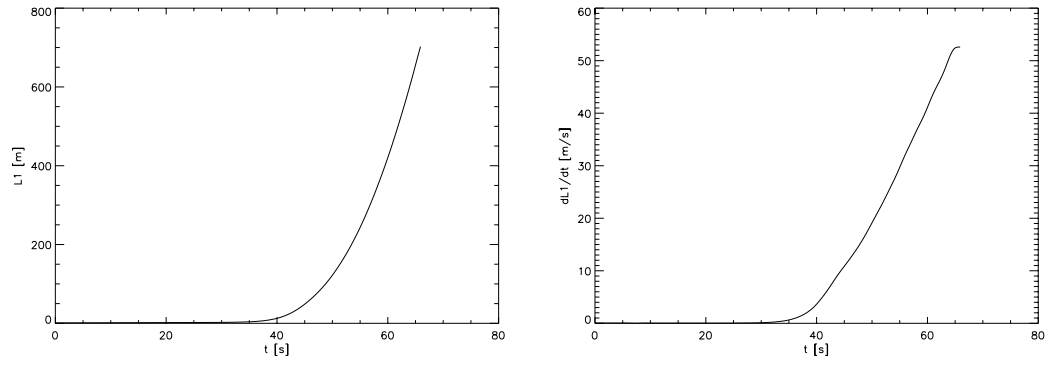

Figure 1.4: L_1 excess phase (left) and excess Doppler shift (right) for occultation parameters as in figure 1.3. Excess Doppler shift is expressed in m/s. The change in inclination of the excess Doppler curve at the very end is discussed in section 3.2.

spherical symmetry close to the tangent point, the individual positions are of no relevance. The drift of an occultation tangent point can be hundreds of kilometres if the LEO satellite is moving perpendicular to the line of sight (side viewing occultation), or very short if they have parallel velocities both towards or away from the tangent point (head on occultation).

1.1.2 The Ionosphere

The first (and last) part of the atmosphere affecting the GPS radio signals in an occultation situation is the ionosphere, which is found above ≈ 80 km and consists of charged particles (ions and electrons) produced by solar radiation exciting and ionising neutral atoms. Electrons affect radio signals in a dispersive way, meaning that the refractive index of the ionosphere is frequency dependent, as described by the Appleton-Hartree equation** (Fälthammar, 1992):

$$n^2 = 1 - \frac{X(U-X)}{U(U-X) - \frac{1}{2}Y_T^2 \pm [\frac{1}{4}Y_T^4 + Y_L^2(U-X)^2]^{1/2}} \tag{1.5}$$

with the standard notation of Union Radio-Scientifique Internationale (URSI) of X, Y and Z. For most use the terms involving the collision frequency ν (all Z-terms) and geomagnetic field B (all Y-terms) are ignored because of the low plasma-density and the weak geomagnetic field, leaving us with:

$$n^2 = 1 - X$$

where $X = (\frac{\omega_N}{\omega})^2$, ω being the angular frequency and $\omega_N = \sqrt{\frac{n_e e^2}{\epsilon_0 m_e}}$ the plasma frequency, depending upon some constants (electron charge e [not to be confused with

**Sir Edward Victor Appleton, September 6th 1892 - 1965. British physicist, Nobel Price winner in 1947.
Douglas Rayner Hartree, March 27th 1897 - February 12th 1958. British mathematician.

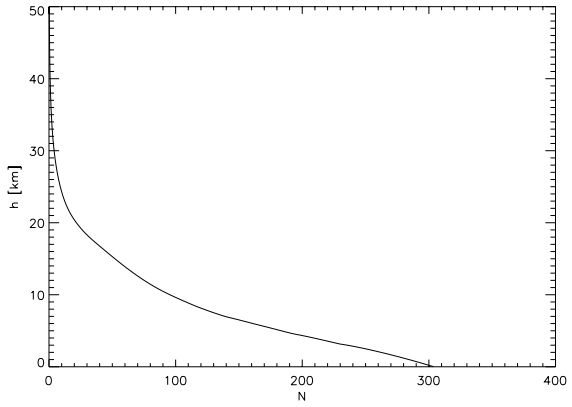

Figure 1.5: Refractivity profile, occultation parameters as in figure 1.3.

the water vapour partial pressure using the same notation], free space permittivity ϵ_0 and electron mass m_e) and the - variable - plasma electron density n_e.

As GPS signals are emitted at two frequencies f_1 and f_2, the ionospheric contribution to the phase delay (through the integrated electron density) can be removed to first order by a linear combination of the two phases (Syndergaard, 2000):

$$L_c = \frac{f_1^2 L_1 - f_2^2 L_2}{f_1^2 - f_2^2}. \tag{1.6}$$

The correction has to be performed for samples with the same time-stamp and it is assumed that the two rays have followed the same paths (which is not exactly true).

An alternative correction is performed on the bending angles (Vorob'ev and Krasil'nikova, 1994):

$$\alpha_c = \frac{\alpha_1 f_1^2 - \alpha_2 f_2^2}{f_1^2 - f_2^2} \tag{1.7}$$

In this case, the correction has to be performed at the same impact heights for α_1 and α_2. This can be achieved by sorting and/or interpolation to common impact heights, e.g. the impact heights of one of the signals.

Higher order contributions from the ionosphere remains in the signals, but as errors in the profile are damped exponentially almost no ionospheric error is present at tropospheric heights which is the main topic of this work. For studies of the atmosphere between 10 and 50 km more care has to be taken regarding the ionospheric contribution, e.g. applying further constraints by climatologic models (so-called statistical optimisation (Hocke, 1997)) and including more terms in the ionospheric correction (Syndergaard, 2000).

Instead of just removing the ionospheric contribution to the phase delay, information on the electron content of the ionosphere can be derived. Along each ray the total electron content (TEC) can be determined. Applying the Abel transform to these measurements results in an electron density profile. Such electron density profiles have been compared to other ionospheric measurements to a large degree showing agreement. Furthermore, ionospheric occultations have been combined in a tomographic algorithm, enabling mapping of the ionosphere (Rius et al., 1997)

1.1.3 The neutral and dry atmosphere

The neutral, dry atmosphere consists of several gases, such as N_2, O_2 and CO_2. These gases are well mixed because they are not produced or destroyed at a measurable rate. On the other hand, molecules as water and ozone (H_2O and O_3) are supplied to and removed from the atmosphere at significant rates, making their distribution very irregular.

In the neutral atmosphere (only containing gases and no particles or liquid water), the refractivity can be expressed as (Thayer, 1974):

$$N = k_1 \frac{p}{T} + k_2 \frac{e}{T} + k_3 \frac{e}{T^2} \tag{1.8}$$

where p is the atmospheric partial pressure of dry air, e the partial pressure of water vapour and T the atmospheric temperature. The constants k_{1-3} are determined both experimentally (results collected in (Bevis et al., 1994)) and theoretically (Foelsche, 1999), and take values close to 77.6 K hPa, 64.8 K hPa and $3.73 \cdot 10^5$ K^2 hPa respectively (see sect. 3.3).

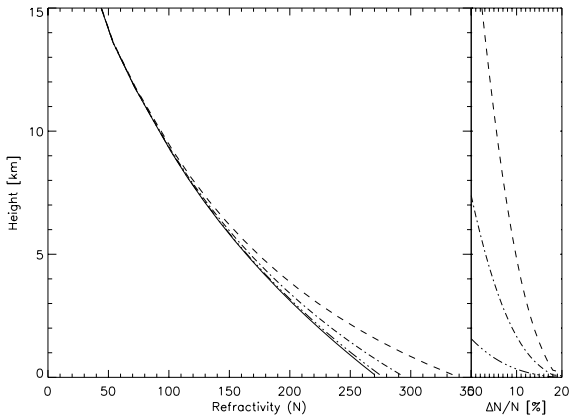

Figure 1.6: Variations of the refractivity, based on US Standard 76 atmosphere, water vapour with scale height of 2.3 km and $e = [0, 1, 5, 15]$ hPa at $h = 0$ km (solid, dash-dot-dot-dot, dash-dot and dash respectively).

A temperature can be derived directly from the refractivity if the atmosphere is assumed completely dry ($e = 0$). In this case the ideal gas equation ($p = \rho RT$, with ρ being gas density and $R = 8.31$ J mol^{-1} K^{-1} the gas constant) together with the reduced dry version of equation 1.8 combines to an expression for the density:

$$\rho = \frac{N}{R\, k_1}$$

Having a density profile the pressure can be derived from the hydrostatic equation:

$$p(h) = \int_h^\infty \rho(r) g(r) dr$$

where g is the acceleration of gravity. Some consideration has to be payed to the upper boundary as the measurements do not reach infinity (e.g. (Hocke, 1997)). Now at each height the temperature can be calculated from the dry version of equation 1.8:

$$T = k_1 \frac{p}{N}$$

This temperature is often referred to as the 'dry temperature', but it has no physical connection to the real temperature where water vapour is present.

In figure 1.7 the result of such an inversion can be seen. The discrepancy between the dry temperature and the ECMWF model is a measure of the amount of water vapour present in the atmosphere, which can be inverted to a real physical water vapour measurement as is shown in section 1.1.4.

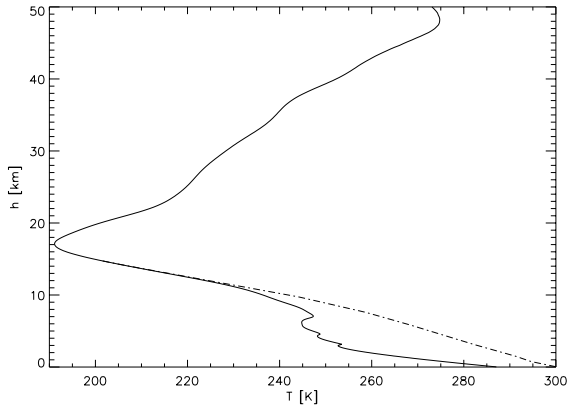

Figure 1.7: Temperature profile of occultation (parameters as in figure 1.3) in solid line, and corresponding ECMWF temperature profile as dashed line.

Many details are present in the retrieved profiles, most of them containing physical information as both the vertical resolution and the temperature precision are high. On the other hand the signal is integrated over more than hundred kilometres horizontally, over which the atmosphere is expected to change, resulting in some average temperature profile.

1.1.4 Water vapour

Water vapour is, contrary to many other constituents of the atmosphere, not smoothly distributed. This feature is a result of the continuously production and destruction in the atmosphere of the gas, at time-scales shorter than required by the movements of the atmosphere to smoothen the distribution. A nonuniform distribution is also found for other constituents created and destroyed in the atmosphere, such as ozone (O_3) and methane (NH_3).

As stated in equation 1.8 the refractivity of the atmosphere is depending on both the temperature and pressure. This dependency, combined with the common scale heights for atmospheric pressure ($\approx$ 7 km (Salby, 1996)) and water vapour partial

pressure ($\approx$ 2.3 km (Luntama, 1997, p. 82),(Black and Eisner, 1984)) tells us that at a height above approximately 15 km the contribution to the refractivity from water vapour is negligible due to the fast decrease of water vapour pressure and the (almost linear) temperature increase, which enters the refractivity equation as inverse square in the most significant water vapour contribution. Above this height (approximately the tropopause) the temperature and the water vapour pressure are so low that no signature of water vapour is left for GPS occultation measurements.

Derivation of equation of state

For derivation of the dry parameters the ideal gas equation is used:

$$P = \rho RT$$

describing the behaviour of single atomic gases. For our purpose the ideal gas approximation is satisfactory as the atmosphere consists of mainly small molecules.

When deriving the water vapour pressure the equation of state has to be modified to a two-gas equation. If the two gases are assumed to be in equilibrium (same temperature), the two gases can be treated as totally separated. For the further derivations it is convenient that water vapour only makes up less than 1% of the volume of the atmosphere, hence an assumption of small relative water vapour amounts is valid. These two assumptions (separated gases and little water vapour) combines to expressions for the relative humidity q and mixing ratio r as function of molar weights m_d and m_v for dry and wet contributions:

$$q \equiv \frac{\rho_v}{\rho_d} = \frac{v_v}{v_d} = \frac{m_d}{m_v} \tag{1.9}$$

$$r \equiv \frac{q}{1-q} \approx q \tag{1.10}$$

The total pressure P is the sum of the partial pressures p_i:

$$P = \Sigma_i p_i$$

The ideal gas equation for water vapour can be divided by the ideal gas equation for dry air using the specific volumes R_v and R_d:

$$\frac{e}{p}\frac{v_v}{v_d} = \frac{R_v}{R_d} \equiv \frac{1}{\epsilon}$$

Using first assumption 1 (equation 1.9) and then assumption 2 (equation 1.10):

$$\frac{v_v}{v_d} = \frac{m_v}{m_d} \approx \frac{1}{r}$$

which can be simplified to

$$\frac{r}{\epsilon} = \frac{e}{P} \tag{1.11}$$

As the mean specific gas constant $\overline{R}$ for a mixed gas consisting of i components is:

$$\overline{R} = \frac{\Sigma_i m_i R_i}{m}$$

($m = \Sigma_i m_i$) the mixing of dry and moist air results in:

$$\overline{R} = \frac{m - m_v}{m} R_d + \frac{m_v}{m} R_v = (1-q)R_d + qR_v = (1-q)R_d + \frac{q}{\epsilon} R_d = [1 + q(\epsilon^{-1} - 1)]R_d$$

Hence a new equation of state for the mixed gas can be expressed as

$$Pv = \overline{R}T$$

or, introducing the *virtual temperature* $T_v = [1 + q(\epsilon^{-1} - 1)]T$:

$$Pv = R_d T_v. \tag{1.12}$$

Equation 1.11 is expressing a rough conversion between q and e (as $r \approx q$), depending upon the total pressure:

$$q \approx \frac{\epsilon e}{P}$$

A more precise treatment, which is valuable in the inversion of the occultation data is based the definition of q and expressions for the density of water vapour and dry air:

$$\rho_d = p/RT$$

$$\rho_w = \epsilon e/RT$$

leading to (Salby, 1996):

$$q = \frac{\rho_w}{\rho_d + \rho_w} = \frac{\epsilon e}{p + \epsilon e} = \frac{\epsilon e}{P - (1-\epsilon)e} \tag{1.13}$$

e from refractive index

The water vapour pressure e can be derived in an iterative method from the equations above with input being a dry temperature profile T_d, a refractivity profile N and a temperature profile T_t considered to be true. From an initial value of $q = 0$ g kg^{-1} at all heights, the virtual temperature T_v can be derived (to be T_d at 1st iteration), and from that a total pressure P from equation 1.12 and the hydrostatic equation. Equation 1.8 is inverted to derive the water vapour pressure e from the dry pressure. An example of the water vapour profile after each iteration is seen in figure 1.8. Usually the iterative process converges to a precision of $\Delta e < 0.01$ hPa within 3 iterations.

1.2 Resolution

In remote sensing measurements it is very important to know the resolution in order to avoid inversion artifacts and thereby use the measurements in a way that is inconsistent with their values. For users of the occultation derived profiles the resolution is of importance for meteorologists, climatologists and other with interest in the atmosphere. In this context the spherical symmetry is a key assumption.

1.2.1 Spherical symmetry

As stated early in this text the spherical symmetry is a key assumption, originating all the way back to the first inversion steps. This makes it reasonable to ask how valid the assumption is. One test is simulating the variations of the impact parameter when ray tracing through a non-spherical symmetric atmosphere model as done in (Healy, 2001). Even small variations in impact parameter along the rays transform into uncertainty of the impact height at the tangent point, with largest uncertainty close to the ground (around $2 - 4$ km height).

1.2.2 Vertical resolution

The vertical resolution of an occultation profile is depending on the inversion algorithms used, especially on the approach to the signal propagation. Usually the resolution scale used is the size of the first Fresnel[††] zone, above which the commonly

[††]Augustin Jean Fresnel, May 10th 1788 - July 14th 1827. French mathematician.

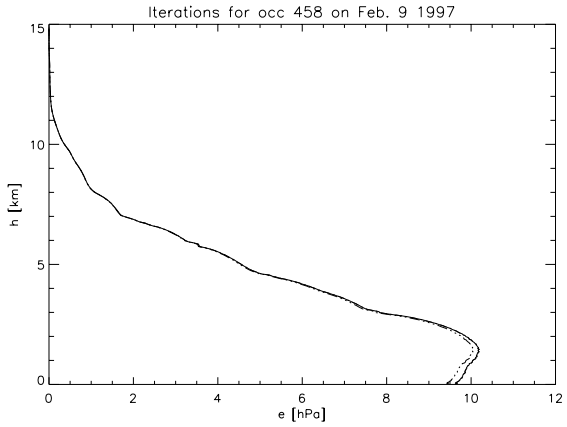

Figure 1.8: Iterations of the water vapour profile. Occultation is as in figure 1.3 and the 'true' temperature is from the ECMWF. The first iteration is dashed-dotted, the next dashed (almost not visible) and the third and final solid.

used geometric optic (GO) approach is applicable. The scale (also the vertical resolution when using the GO approach) is expressed as:

$$r_{Fresnel} = \sqrt{\lambda z}$$

with λ being the wavelength of the signal and z the distance between the receiver and the point of disturbance (see figure 1.9).

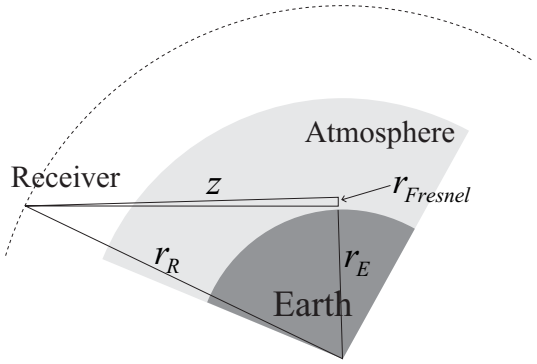

Figure 1.9: Illustration of the vertical resolution.

In the case of occultation measurements z is the distance between the LEO and the tangent point of the ray. The distance is $z = \sqrt{r_{LEO}^2 - r_{Earth}^2} \approx 3300$ km, resulting in a typical value for the Fresnel zone of 1 km. The resolution is highest at altitudes where atmospheric properties cause defocusing and lowest at altitudes with focusing properties (Fjeldbo and Eshleman, 1969), indicating that the resolution increases downwards as the bending angle in general increase exponentially downward (Luntama, 1997).

The derivation above is for a medium with weak turbulence. In the case of strong turbulence the resolution is decreased because of a large amount of stronger gradients (Fjeldbo and Eshleman, 1969).

With the Fresnel inversion the vertical resolution can be improved, with a documented minimum of around 200 m (Mortensen and Høeg, 1998). This increase in resolution is the result of using the entire received field and not just the phase information.

The intrinsic resolution r_i for occultation data can be estimated from the vertical tangent point velocity ($v_v \approx 1.5$ km s^{-1}) and the sample rate τ to $r_1 \approx 2\frac{v_v}{\tau}$ which for present $\tau = 50$ Hz receivers is on the order of $r_i \approx 60$ m.

1.2.3 Horizontal resolution

Given a vertical resolution, e.g. by the Fresnel criterion, a horizontal resolution can be estimated as the length of the line of sight through a spherical shell with the

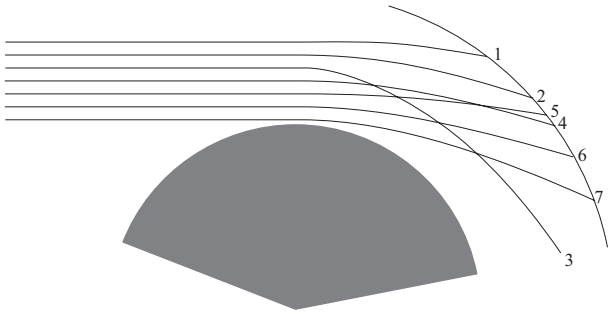

Figure 1.10: A schematic snapshot of possible ray paths. Consider the GPS to be fixed and the LEO to be at some point along the right curve. The rays are numbered to keep track of them, see text for explanation.

thickness as the Fresnel diameter. In practice this results in a horizontal resolution of about $150 - 300$ km (Luntama, 1997; Kursinski et al., 1996), best close to the ground.

An alternative horizontal resolution determination is based on the differential bending along the ray path:

$$\beta = \frac{d\alpha}{d\theta}$$

where θ is the angle between the GPS position vector and the ray path position vector. Examination of β as function of the distance travelled along the Earth's surface reveals that most of the total bending takes place close to the tangent point and the distribution is nearly similar to a Gaussian distribution. This curve shape makes it obvious to use a 'full width at half maximum' value as the horizontal resolution. This measure is examined in (Høeg et al., 1995) and results in horizontal resolution estimates of around $300 - 340$ km, worst close to the ground.

1.2.4 Critical refraction

As the rays are slightly bent towards the surface of the Earth, conditions might occur for which the rays end up on the surface of the Earth or, in the limit, follow the local atmospheric curvature. This special case is encountered when the refractivity gradient is so strong that the radius of curvature for a ray is smaller than, or equal to, the local radius of curvature of the atmosphere, R_c. The phenomenon is also referred to as super-refraction (Gorbunov et al., 1996b). Even if one ray experiences critical refraction there will still be a signal at any point along the LEO orbit, but it might be very weak due to the strong defocusing experienced close to critical refraction. In Figure 1.10 strong defocusing is present between 1 and 2, and 6 and 7. Ray 3 experience critical refraction and multi-path is present at the specified orbit for rays 4 to 5.

From (Born and Wolf, 1980, p. 131) it is seen that in a spherical medium the (scalar) curvature K (the reciprocal of the radius of curvature) for a ray is

$$K = \frac{d \ln n}{dr} = \frac{1}{n}\frac{dn}{dr} \approx 10^{-6}\frac{dN}{dr}$$

For the atmosphere the scalar curvature is $-1/R_c$ with $R_c \approx 6.4 \cdot 10^6$ m. For the ray to curve more than the atmosphere the relation:

$$\frac{dN}{dr} < -\frac{10^6}{R_c} \approx -0.156 \text{ m}^{-1} \tag{1.14}$$

has to be fulfilled.

This steep gradient in N can be compared to the general smooth decrease of about -0.02 m^{-1} (see figure 1.6). Differentiating equation 1.8 (ignoring the least significant water vapour term) with respect to r gives:

$$\begin{aligned} \frac{dN}{dr} &= \frac{k_1}{T}\frac{dP}{dr} - \frac{k_1 P}{T^2}\frac{dT}{dr} + \frac{k_3}{T^2}\frac{de}{dr} - \frac{2k_3 e}{T^3}\frac{dT}{dr} \\ &= -\frac{k_1 P}{H_p T} - \left(\frac{k_1 P}{T^2} + \frac{2k_3 e}{T^3}\right)\frac{dT}{dr} + \frac{k_3}{T^2}\frac{de}{dr} \end{aligned} \tag{1.15}$$

with H_p being the pressure scale height (see (Christensen-Dalsgaard, 1993, sect. 4.5.2)),

$$\frac{dP}{dr} = -g\rho = -\frac{P}{H_p}.$$

Filling in realistic numbers of the lower troposphere ($H_p = 7800$ m, $T = 280$ K, $P = 850$ hPa and $e = 9$ hPa) in equation 1.15 gives:

$$\frac{dN}{dr} = -0.03 \text{ m}^{-1} - 1.15 \text{ K}^{-1}\frac{dT}{dr} + 4.76 \text{ hPa}^{-1}\frac{de}{dr}$$

which reveals that in order to gain critical refraction (equation 1.14 and 1.15) the gradients are constrained to

$$\frac{dT}{dr} \geq 0.113 \text{ K m}^{-1} + 4.14\text{K hPa}^{-1}\frac{de}{dr}.$$

The required temperature gradient is far greater than what is realistic for the atmosphere, but the water vapour pressure gradient is within reach, as the average scale height of the water vapour profile is 1.4 km.

1.3 Attenuation

The GPS microwave signals are not received with a constant strength throughout an occultation, see e.g. figure 1.11. These variations are due to both (de)focusing and

damping of the signals as they travel from the transmitter, through the atmosphere to the receiver.

The refractive index contains not only the propagation velocity slowing parameter used so far, but also an amplitude reducing parameter. These two contributions are often collected in one complex refractive index:

$$n = n' - in''$$

where n' is close to unity and n'' is close to zero.

For a terrestrial atmosphere the curves of n' and n'' are plotted in figure 1.12. It can be seen that n'' changes drastically with relative humidity (RH) and that n' at a few frequencies depend strongly on the relative humidity, but otherwise is close to 0.

Most of the decrease in signal strength during an occultation is caused by defocusing (relative to attenuation, see below) which in the occultation case is the result of the atmosphere acting as a negative lens: The deeper layers of the atmosphere the rays penetrate, the more negative is the 'lens', resulting in the strongest defocusing near the surface.

Irregularities in the atmosphere can cause an even stronger defocusing, or in some cases focusing of the signal. In case of focusing the back-propagation method is used for disentangling the ray-paths as this situation is also known as multi-path as more rays reach the receiver at the same time, see section 3.5. Any deviations from a steady increasing refractivity gradient will result in multi-path at some point,

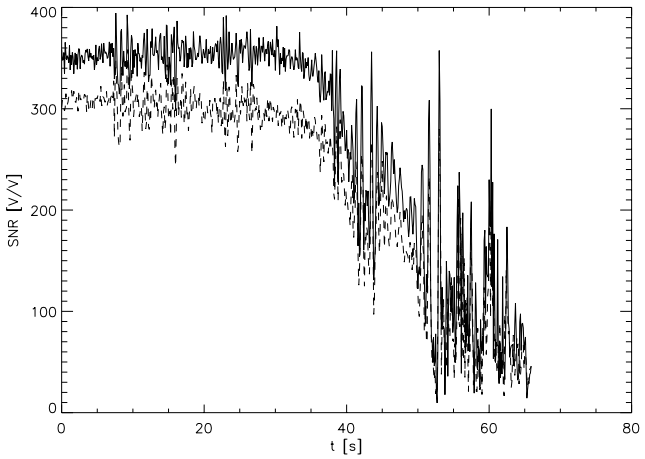

Figure 1.11: Signal to noise ration of the two frequencies L1 (solid line) and L2 (dashed line) for occultation parameters as in figure 1.3. Notice the steep drop when the neutral atmosphere is being sounded and the fast variations due to irregularities in the atmosphere.

which might not be inside the receiver orbit.

In the microwave regime below 10 GHz the dry air is very close to transparent (Liebe, 1989) except for some oxygen lines. When water vapour is added to the atmosphere several new lines emerge. The main microwave transitions in the water vapour molecule is around 22.235 GHz (1.35 cm) which is far away from the GPS L band signals. More strong lines are found around 183, 550 and 750 GHz.

It must be concluded that at the used frequencies not much information on water vapour can be gained from the signal damping, even when correcting for the (strong) defocusing. But the humidity information could be extracted if using several signals at frequencies close to the mentioned water vapour lines, where the attenuation can reach many dB per kilometre of transversed atmosphere. Also in this respect is the 22 GHz line interesting as the attenuation is only at the order of 1 dB km^{-1} which makes the signal survive through the atmosphere at a detectable level. This is used for the proposed ACE+ satellite, which is to probe the atmosphere with a LEO-LEO microwave link (Høeg and Kirchengast, 2002). But applying signals at this frequency changes the vertical resolution. As the wavelength goes down by a factor of ≈ 15 the Fresnel radius decrease by a factor $\sqrt{15} \approx 4$.

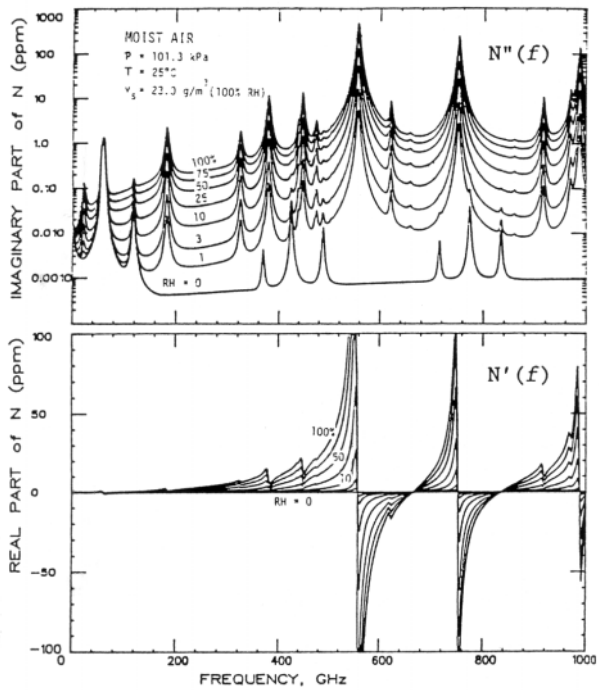

Figure 1.12: Curves of real (n') and imaginary parts (n'') of refractive index as function of frequency and relative humidity (Liebe, 1989). The GPS L-band frequencies are found to the far left at ≈ 1.5 GHz.

1.4 Assimilation into NWP's

From the point of view of a data user, it can be convenient to distinguish between data at the different processing stages and name them after the level of processing performed. In this terminology low level data are least processed (e.g. phases) and high level data most processed (e.g. temperature and humidity profiles).

Some effort has been put into methods of assimilating GPS occultation measurements into numerical weather prediction models (NWP), both at various level of processing (e.g. (Eyre, 1994)) and more recently also as low level products (phases or bending angles (Zou et al., 1999)). The more processed product assimilated, the more assumptions are made and hence a more elaborate error analysis has to be performed in order to assimilate the GPS occultation data in a consistent manner. Therefore, assimilation could be preferred with the least processed products (low-level products), but the more processed products (higher level products) data are required for research on individual profiles or phenomena (e.g. fronts and gravity waves). At present the problem in assimilating data is, as stated in (Palmer et al., 2000), the missing error estimates. This is especially a problem when addressing high level products since many assumptions and processings have been made. Furthermore, a specific problem for the occultation data is the correlation between heights in the profiles. This is a result of the inversion which is performed in data scanning several heights at once, making one layer of inverted data depend on higher layers. Some of the problems in the error budgets have been addressed in (Syndergaard, 1999).

Most of the bending takes place at the tangent point of the ray (Høeg et al., 1995, fig. 19), and furthermore the bending (and hence vertical resolution) is increasing with decreasing tangent-height. This makes the measurements well suited for assimilation into NWP's as they often use pressure levels which also are increasingly dense near the ground. Also the uniform distribution of occultation measurements makes the data a potential significant contribution to the NWP's.

The ratio between the horizontal and vertical resolution can be estimated to around 300. This ratio is interesting in relation to the use of this type of data in a NWP as the models have close to the same ratio. In (Fox-Rabinovitz and Lindzen, 1993) the optimal horizontal resolution data used as input to numerical experiments is determined to be $\Delta S = 200 - 400$ km for vertical resolutions on the scale of $\Delta z = 0.75 - 1.5$ km. These numbers are very close to the resolution numbers found above for the occultation measurements, indicating the suitability of the occultation measurements for assimilation.

1.5 Climate parameters

For studies of long term climate trends of a parameter (e.g. temperature, tropopause height or geopotential height of specific pressure levels) a high precision of the parameter is required since only small variations are expected over the life time of an instrument. This is partly overcome by the GPS occultation method which requires no external calibration, but only relies on stable oscillators.

Simulations and error analysis of individual profiles reveal an error close to $\Delta T \approx 1$ K at heights between 10 and 30 km. Averaging an ensemble of m profiles in a given region and time decrease the error on the average profile by a factor $\sqrt{m}$, indicating that an error of 0.1 K can be reached with $m = 100$. With 500 profiles per satellite per day, the 0.1 K error can be reached in five zones in one day, or e.g. in 35 zones over one week with one satellite. More satellites would either decrease the error or increase the number of cells for a given times-pan and error level.

1.6 Satellites with GPS occultation capabilities

So far only rather few satellites have carried GPS occultation receivers, and none have been part of an operational system. In table 1.1 is listed names and key parameters for past, present and known future satellites.

Satellite/project	Launch	Receiver	Orbit height (km)
GPS/MET	April 3rd 1995	TurboRogue	730
Ørsted	February 23rd 1999	TurboRogue	500-850 (elliptical)
SUNSAT	February 23rd 1999	TurboRogue	800
CHAMP	July 15th 2000	BlackJack	450-300 (decreasing)
SAC-C	Nov. 2000	BlackJack	700
GRACE (2 sat's)	March 17th 2002	BlackJack	500 (decreasing)
FedSat	2002	BlackJack	803
Metop	2005	GRAS	800
ACE+ (4 sat's)	2005	GRAS+ LEO-LEO	650 and 850

Table 1.1: Names and key parameters of satellites with GPS occultation capabilities.

The TurboRogue and BlackJack receivers are made by JPL (Jet Propulsion Laboratory), and the GRAS (GNSS Receiver for Atmospheric Sounding, GNSS meaning Global Navigation Satellite System) by Saab-Ericsson Space in cooperation with EUMETSAT and ESA (European Space Agency).

Even though satellites have been equipped with similar receivers, the outcome might differ as the software usually can be altered both before launch and in orbit.

Only generations later than the TurboRogue have open loop capabilities.

1.7 Alternative frequencies

As mentioned, a third frequency is decided for the GPS system. This frequency lies very close to the L2 frequency, resulting in not much new information in the perspective of occultation measurements. A further separation would benefit the meteorological society, but because the system is designed for positioning this task still has first priority. More frequencies have been discussed and from a meteorological point of view these frequencies should be selected so that a strong signal from water vapour should be measured. A dedicated water vapour channel such as the one selected for Water Vapour Radiometers at around 22.235 GHz ($\lambda_{L5} \approx 1.3$ cm) would be highly desirable. This would make direct measurements of low water vapour possible as suggested in the ACE+ satellite proposal (Høeg and Kirchengast, 2002) which will perform occultation measurements at several frequencies close to the 22 GHz water peak.

Chapter 2

Water vapour in the Atmosphere

2.1 Water in the climate

Water is a very important participant in the meteorology and climate of Earth as all three phases of water can exist under the conditions of the atmosphere, and large amounts of energy bound or released at phase transitions. Furthermore water vapour is a very strong greenhouse gas and water is considered the basis of life. Clouds which are very important in the energy balance of the atmosphere are also made of water in the form of small drops. The exact role of the clouds is not certain, but they act both as a greenhouse gas (heating of the atmosphere) and increase the average terrestrial albedo (cooling of the atmosphere).

2.1.1 The hydrologic cycle

A cyclus is established with evaporation from ocean/land surface to the atmosphere, condensation of this humidity to rain/snow which in turn falls to the land surface/ocean as sketched in figure 2.1. The cycle is referred to as the hydrologic cycle referring to water being recycled (examples of other cycles are e.g. the carbon and nitrogen cycles). The source that makes the cycle go is mainly the solar influx of energy (and the rotation of the Earth) which on global scale on average is $\mathcal{I} \approx 340$ W m^{-2}. Of this a significant fraction (about 30%) is directly re-emitted as reflection from clouds, water and ice (this is referred to as the planetary albedo). Part of the remaining energy is tied up in evaporating water.

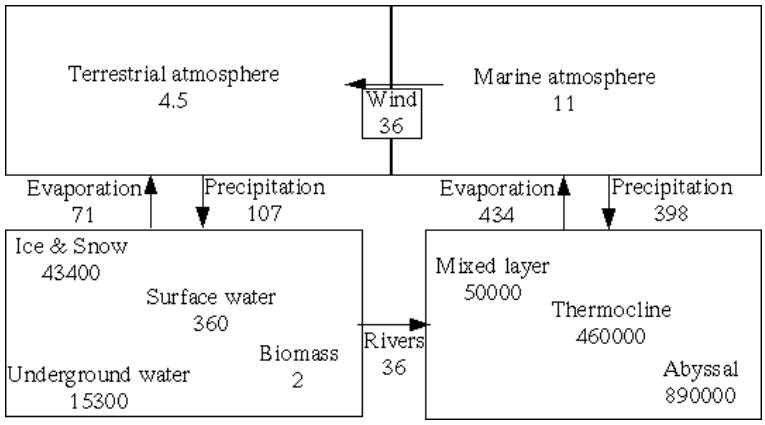

Figure 2.1: Schematic overview of the transportation of water in the atmosphere, both as liquid and gas, adapted from (Mockler, 1995). The numbers are in 10^{15} kg for the reservoirs (boxes) and 10^{15} kg yr^{-1} for the fluxes (arrows).

A time-scale τ for each water reservoir can be established as the ratio between the mass of water contained in the reservoir $\mathcal{M}$ and the average water flux $\mathcal{F}$ in (or

out) of the reservoir:

$$\tau = \mathcal{M}/\mathcal{F}$$

This ranges from the longest in the oceans (ignoring the time-scale of the ice caps, which is of the order of 10^5 yr) of several thousands of years, to the shortest in the atmosphere where the given reservoir and flux results in a time-scale of about 9 days, meaning that on average all water in the atmosphere is replaced every 9 days.

Considering the Earth being one system, it can be divided into subsystems ('spheres') interacting in the climate. The subsystems are illustrated in figure 2.2. All the subsystems contain water in various amounts and phases. Below is reflected on the distribution of the various water phases in the spheres.

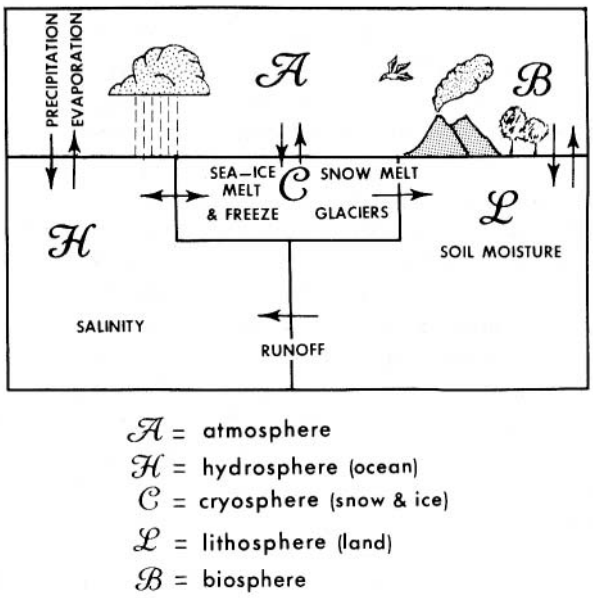

Figure 2.2: Schematics of the subsystems and their interactions regarding the Earth's climate (from (Peixoto and Oort, 1992)[fig. 2.1]).

Solid water - ice

Most of the water in the solid phase is referred to as the cryosphere. Ice is found mainly as polar ice-caps (8% on Greenland and 91.5% on Antarctica), but also to a smaller extend in other smaller glaciers (0.5%), snow and permafrosen in the ground. A very small amount is found as ice crystals at high altitudes in the atmosphere. These crystals seem to play an important role in the ozone balance as they transform inactive chlorine containing molecules into active ozone destroying molecules, hence acting as a catalyst for increased ozone destruction.

Approximately 2% of the global water is stored as ice, with the polar ice caps containing $43 \cdot 10^{15}$ m^3 ice, corresponding to $40 \cdot 10^{15}$ m^3 liquid water.

The interaction between the cryosphere and water vapour is rather weak as the ice is such a minor water reservoir.

Liquid water

Liquid water is covering more than 2/3 of the Earth's surface to an average depth of 2 km, resulting in a total of at least $7 \cdot 10^{17}$ m^3 in the oceans (the hydrosphere). Only the upper few hundred meters of the oceans is exchanging energy with the atmosphere on time-scales of a few years. The oceans contains almost all the water on Earth, about 97%. A small amount (less than one percent) is found in lakes, rivers and soil moisture in the solid Earth, the lithosphere.

An insignificant fraction (when considering mass) is found as drops in the atmosphere, forming clouds and precipitation. The significance of this liquid water increase if the point of view is the energy balance in the atmosphere as clouds are responsible for both cooling and heating of the atmosphere as mentioned above.

Gaseous water - vapour

Water in the phase of gas is one of the least acknowledged components of the atmosphere in the common public. It consists of single free water molecules and is invisible for the human eye. Only when it becomes small (liquid) drops it is visible. Unlike the generally spherical symmetrical distribution of the atmospheric constituents (nitrogen, oxygen etc), water vapour (and a few other constituents such as ozone) is distributed very irregularly. This is a result of the continuous production and destruction in different regions of the globe at different rates, and that the general motion of the atmosphere is not fast enough to homogenise the distribution. Other constituents of the atmosphere are better mixed because of the lack of production and destruction at high rates.

Because the amount of water vapour is closely linked to the temperature of the atmosphere through the Clausius-Clapeyron equation (see equation 2.1 below), the (hot) tropical region (latitude less than about 30°) contains a large amount of water vapour. Part of this is transported pole-ward by the Hadley* cells close to the equator and the Ferrell† cells at higher latitudes.

In total the atmosphere contains water vapour corresponding to a global cover of 2.5 cm liquid water (as compared to a kilometre scale layer if averaging the oceans globally).

*George Hadley, 1685 - 1768. English meteorologist.

†William Ferrell, January 29th 1817 - September 18th 1891. American mathematician and geophysicist.

2.1.2 Phase transitions

Evaporation of water requires large amounts of energy (2.45 MJ kg^{-1}) which is supplied by the solar radiation. This energy is carried with the vapour as latent heat into the atmosphere where it is released when the temperature drops below the condensation temperature. The latent energy of the vapour is then returned to the atmosphere as molecular kinetic energy. In case the amount of water vapour in the atmosphere would go up (because of an increased Solar activity, increased greenhouse effect or some other cause) the amount of latent energy would increase similarly, giving room for more strong meteorological phenomena.

Changing ice into liquid water requires somewhat less energy (333 kJ kg^{-1}, about 1/7th of the evaporation energy per mass unit).

An elaborate phase diagram of water (with two projections) is shown in figure 2.3.

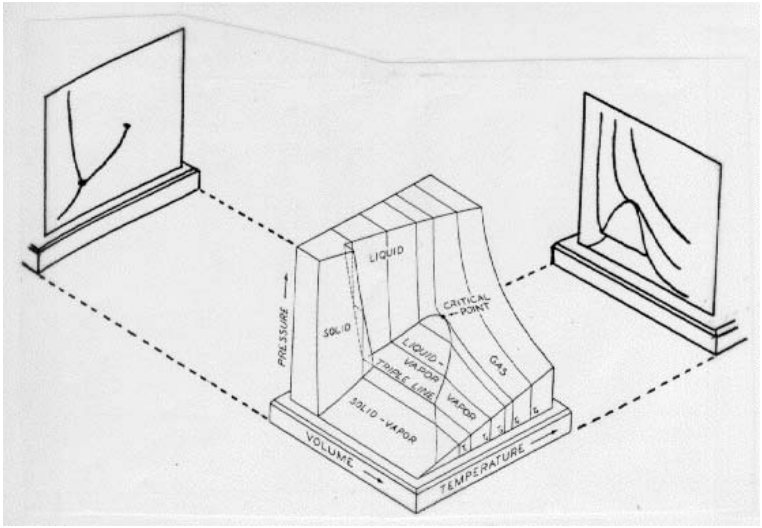

Figure 2.3: The phase diagram for water. To the left is the pressure-temperature projection and to the right the pressure-volume projection.

Several interesting features are noticed. In the pressure-temperature projection there are lines defining equilibrium conditions of the phases on each side of the line. All the lines cross in one point, the triple point, where all three phases exist in equilibrium (T = 273.16 K and p = 611.3 Pa). The line to the right from the triple-point separates the liquid and vapour phases and ends at the critical point at 647 K where the phase of water is determined by the density. In the other projection (volume-pressure) isothermal lines are plotted. For some temperatures phase transissions can take place, but above a certain temperature (the critical temperature mentioned above) real condensation does not take place.

Saturated gas

Between water vapour and any of the other two phases (liquid water or ice) an equilibrium exists where as many molecules are evaporated as are condensed or sublimated. The equilibrium is established at a specific pressure - the saturated water vapour pressure - and is depending mainly on the temperature. The pressure depends on the energy available in the system (the temperature), the geometry of the interface between the two phases and the binding energy of molecules at the interface. Hence it can be established that:

- The saturation pressure increases with temperature
- The saturation pressure is higher above a (small) sphere than above a plane surface (this effect is very small and only significant under special circumstances - as in clouds)
- The saturation pressure is higher above water than above ice

The Clausius-Clapeyron equation is describing the saturated gas pressure (the curve from bottom left to top right in the $p - T$ projection of figure 2.3) above a planar interface (Rasmussen, 1991):

$$\frac{de}{dT} = \frac{L}{T(V_g - V_l)} \tag{2.1}$$

where L is the energy needed to evaporate an amount of molecules, and V_g and V_l are the gas and liquid volumes of the same amount of molecules. This equation only contains the temperature as independent variable. The equation exists in several approximated integrated versions, a convenient one being:

$$e = 611 \cdot \exp\left(\frac{17.27T}{237.3 + T}\right) \tag{2.2}$$

where T (for once) is measured in degrees Celcius[‡] which shows an exponential growth of saturated water vapour pressure as function of temperature. In other words: the warmer the atmosphere, the more water vapour it can contain. The saturation curve is found in figure 2.4, where the effect of ice (decreased saturation pressure) is also plotted.

On the Earth the saturation pressure usually is an upper limit of the water vapour partial pressure, but in few cases the pressure is found to be over-saturated. This situation is not stable, especially not as the atmosphere is in constant movement and it contains condensation nuclei. On average the water vapour partial pressure

[‡]Anders Celcius, 1701 - 1744. Swedish astronomer.

is found to be about 75% of the saturated pressure close to the ground (Peixoto and Oort, 1992).

The condensation of saturated water vapour is triggered by condensation nuclei. These are small particles (dust, smoke, salt etc.) being suspended in the atmosphere. They range in size between 10^{-2} and 10^{3} μm and form a group of particles called aerosols. The small ones are produced in large number in smoke by human burning of oil and coal, and the larger particles are from natural corrosion (Salby, 1996).

2.1.3 The Greenhouse effect

Gases (and other substances) absorb radiation at some specific wavelengths and let the other wavevelengths pass through. The windows of transparency are found at various wavelengths for various gases depending on the atomic and molecular configuration.

The surface of the Earth is heated by incoming solar radiation, in this way converting radiation with short wavelength into radiation with longer wavelength. If the atmosphere consists of gases which absorb long wave radiation and let short wave radiation pass, the atmosphere is heated because of the wavelength-transformation (from short to long wavelengths) taking place at the surface. Gases acting in this way are named greenhouse gases[‖]. Greenhouse gases are also called infrared active gases because they are active (absorbing) in the infrared while they are inactive

[‖]except that the main reason for a greenhouse to be warm is the lack of convection (Peixoto and Oort, 1992).

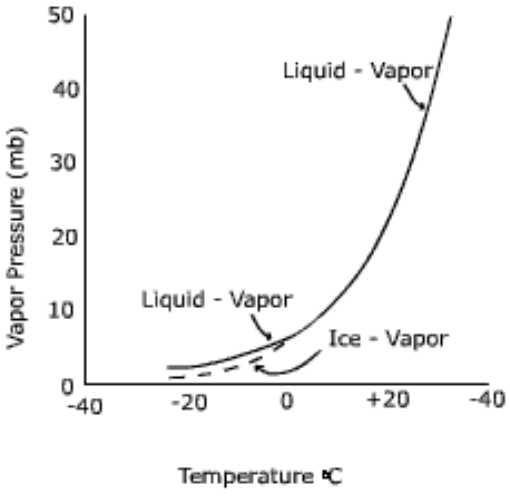

Figure 2.4: The curve of saturated water vapour pressure, both with respect to liquid and solid water[¶].

(transparent) in visual light.

The dominating wavelength of the incoming Solar radiation is determined by Wien's displacement law** (assuming the radiation being from a black-body) stating that:

$$\lambda_{max} = \frac{2.9 \cdot 10^{-3} \text{ K m}}{T}$$

resulting in $\lambda_{max} \approx 0.5$ μm for the incoming radiation (with a Solar temperature of $T = 5800$ K) and $\lambda_{max} \approx 10$ μm for the outgoing radiation with Earth surface temperature of $T = 288$ K.

For a greenhouse gas to be efficient they have to

- Have absorption lines close to the surface peak emission wavelength (≈ 10 μm
- ....and transmit around 0.5 μm
- Have absorption lines where no other atmospheric gasses have lines
- Be abundant

Several gases have these greenhouse gas properties. Most well known is probably carbon dioxide (CO_2) because of the much debated antrophogenic influence on the climate through increased emission of it since the early industrialisation. But actually water vapour is a stronger greenhouse gas because of its very strong long-wave absorption lines, arising from the roto-vibrational transitions in the free molecule. In figure 2.5 the spectra of water vapour, carbon dioxide and other well known greenhouse gases are found.

An efficient absorption line can be even more efficient close to the Earth surface due to pressure broadening. This effect moves the central line strength into the wings, and hence total absorption at a given wavelength gives a larger integrated line strength at high pressures than at low pressures. This effect is especially important for water vapour as it is produced close to the ground.

The greenhouse effect is responsible for a heating of the Earth of about 33 K relative to what would be expected if the Earth had no atmosphere (e.g. (Peixoto and Oort, 1992)[sect. 6.8.1]). The greenhouse effect can also be observed on the planets near the Earth. On Mars there is almost no atmosphere (probably due to the low gravity on the planet) and the planet has the surface temperature expected from unaffected solar radiation. In the other extreme Venus is found to have an extremely hot and dense atmosphere, probably the result of a run-away greenhouse effect. Such a phenomenon could be the result of a strong greenhouse gas being

**Wilhelm Wien, January 13th 1864 - August 30th 1928. German physicist, Nobel Prize winner 1911.

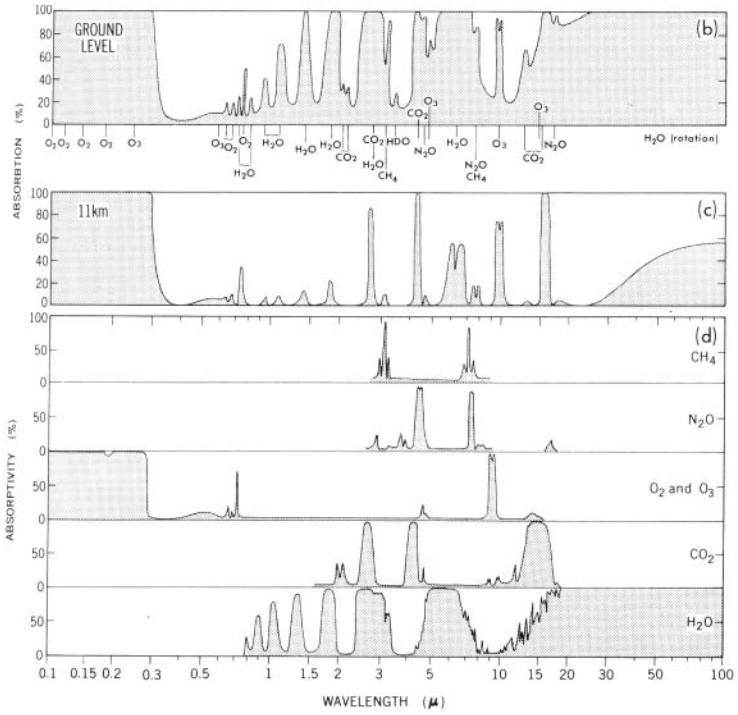

Figure 2.5: The absorption of various greenhouse gases, from (Peixoto and Oort, 1992).

released from the soil/surface as the atmosphere is heated, resulting in more and more of the gas in the atmosphere from the positive feed-back ((Peixoto and Oort, 1992)[p. 31] and (Salby, 1996)[ch. 8.7]).

Water vapour could cause a positive feed back as an increase in the water vapour content of the atmosphere increases the temperature due to the greenhouse effect. This increased temperature again increases the evaporation from the oceans, which then gives rise to more water vapour in the atmosphere and so on. This could look like a chain that could be started at any time by either natural causes (e.g. volcanic eruption or increased Solar activity) or by human activities, but fortunately other processes seem to work in the opposite direction, weakening the effect.

2.1.4 Stratospheric water

Water vapour is found not only in the troposphere. A small amount is also found in the stratosphere (e.g. (Forster and Shine, 2002)), but this small amount can not be detected by the GPS occultation method because the method roughly performs a number count of water molecules along the ray path, and the number of water molecules is below the noise level at stratospheric altitudes, where the water vapour density is 6 ppm (Forster and Shine, 2002).

Across the tropopause not much matter is transported, but a small amount of

water vapour and methane gets through. The methane is oxidate to form water vapour through the solar ultraviolet radiation. The resulting water vapour (Shindell, 2001) decrease the stratospheric temperature and increase the tropospheric temperature, making the stratospheric water vapour an interesting population.

2.1.5 Climate summary

An increase in atmospheric water vapour is the most likely result of increased atmospheric temperature. This could lead to a positive feed back with a further temperature increase, or the feedback could be weakened by cloud formation (but the result of increased cloud formation is highly uncertain) or some other mechanism. The increased amount of water vapour in the atmosphere also can be interpreted as an increased latent energy reservoir in the atmosphere, which will result in more severe weather.

These factors make precise observations of atmospheric water vapour important, on both short and long time-scales.

2.2 Atmospheric small-scale structure

The atmospheric structure on small scales is important to estimate as this influence the resolution of occultation profiles and make validity estimates on the inversion algorithms that can be applied (see e.g. (Tatarski, 1961)).

Temperature and humidity are assumed to be responsible for the small scale fluctuations from the average refractivity as pressure fluctuations are very rapidly being smoothed by sound wave propagation.

When dealing with a turbulent medium as the atmosphere, several scales become relevant. The outer scale L_0 which is the scale at which energy is added to the system - the largest 'blobs' of irregularities - on the order of 10 to 100 m. From this scale the energy cascade to smaller scales as large eddies break up into smaller and smaller ones. This cascading stops at the inner scale l_0 where viscosity dissipates the energy - this happens at l_0 =a few mm. The scheme above is in words the Kolmogorov[††] turbulence theory as illustrated in figure 2.6.

Several works have been presented on the structure of the atmosphere when approaching it through the refractive index (e.g. (Wyngaard et al., 2001; Wyngaard and LeMone, 1980; Wesely, 1976)). Often used parameters are the structure function parameters C_N, C_T and C_e which express the intensity of fluctuations in a parameter (in this case refractivity, temperature and humidity) below a given time scale. Given

[††]Andrei Nikolaevich Kolmogorov, April 25th 1903 - October 20th 1987. Russian mathematician.

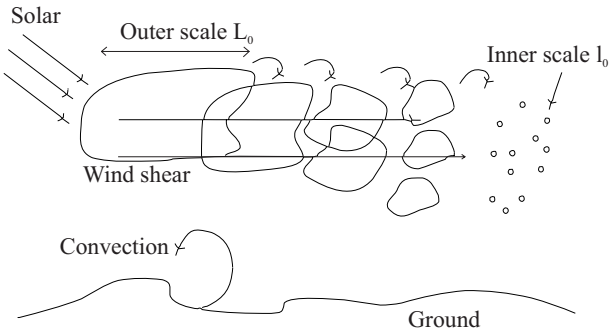

Figure 2.6: Illustration of the idea behind Kolmogorov turbulence theory. The incoming Solar energy is generating eddies at scale L_0. These eddies break up, until they reach the scale l_0 where the energy dissipates.

a parameter $f(t)$ as function of time, the difference function $F_t(\tau) = f(t+\tau) - f(t)$ is stationary for small τ. The structure function now is

$$D_f(\tau) = \langle F_t(\tau)^2 \rangle$$

$\langle\rangle$ denoting an average, in this case over time, but the equation can be adapted to spatial averaging. Corresponding functions can be made spatially, in which case the refractivity structure function can be expressed as $D_N(r) = \langle (N(x+r) - N(x))^2 \rangle = C_{N^2} r^{2/3}$ where C_{N^2} is found to have values on the order of 10^{-13}.

In (Strohbehn, 1969) the valid range of the often used geometrical optics approach to the occultation measurements is set to $\lambda \ll l_0$ and $\sqrt{\lambda L} \ll l_0$. In the occultation case both restrictions are not valid as $\lambda \approx 40 l_0$ and $\sqrt{\lambda L} \approx 1.5 \cdot 10^5 l_0$. But many of the problems arise because the theory is designed for optical electromagnetic waves with very short wavelengths as compared to the (GPS) microwaves. The very small scale eddies are insignificant for the GPS signals as they are only a fraction of a wavelength, and averaging over more samples (filtering the data) loosen the restrictions, making the geometrical optics approach valid with vertical resolution of the Fresnel scale.

Chapter 3

GPS and water vapour

3.1 Observation of water vapour

How can water vapour be observed? As stated earlier water vapour is invisible for the human eye, and we only sense the presence of it as the feeling of moist or as we see the water condensating on surfaces colder than the dew point temperature. We must turn to other regimes of the spectrum or examine at higher spectral resolution.

In order to know where in the electromagnetic spectrum water molecules might be observed, the structure of the molecule, i.e. the dimension and geometry of the rather simple molecule, has to be considered.

The chemical compound hydrogen dioxide (H_2O) can appear in the three states ice, water and vapour, but within each state many sub-groupings are possible, depending upon the physical conditions (pressure and temperature). At the transition between the liquid and vapour phases, mixtures can exist where a few molecules have bound (and still acting as a gas) might have quite different optical properties than a 'real' gas where all molecules are free.

For a start the real gas-case can be treated as in (Foelsche, 1999) starting from the Maxwell* equations. The optical properties of liquid water in the microwave range is treated in (Liebe, 1989), where it is found that almost no water lines are present in the GPS L-bands, but a weak damping might occur for heavy rainfall ($10 - 100$ mm/hour).

At a specific position in the atmosphere, several contributions are made to the refractivity. Most significant is the contribution by the dry atmosphere, but gradually the water vapour is playing a more significant role closer to the surface of the Earth. Of less noticed importance are other constituents, such as clouds, rain, snow, sand and ash. They contribute at various amounts, but the sand can be rather important (Solheim et al., 1999). The relation expressing the refractivity is (written earlier for a neutral gaseous atmosphere):

$$N = k_1 \frac{p}{T} + k_2 \frac{e}{T} + k_3 \frac{e}{T^2} - 40.3 \cdot 10^6 \frac{N_e}{f^2} + 1.4 W_l \tag{3.1}$$

Equation 3.1 is expressing the dependency of refractivity N on various atmospheric parameters such as temperature T, dry atmospheric pressure p and water vapour partial pressure e for frequencies below 20 GHz. N_e is the electron density [m^{-3}] and W_l the amount of liquid water [$\mathrm{g\,m}^{-3}$]. The three constants k_{1-3} have been determined in various works, and a compilation of the estimates is found in (Bevis et al., 1994). The constants have values close to $k_1 = 77.6$ K hPa^{-1}, $k_2 = 64.8$ K hPa^{-1} and $k_3 = 3.776 \cdot 10^5$ K^2 hPa^{-1} (see sect. 3.3). An alternative formulation of the refractivity is based on the compressibility factors which are cor-

*James Clerk Maxwell, June 13th 1831 - November 5th 1879. British physicist.

rections for non-ideal gas behaviour (Thayer, 1974).

Equation 3.1 contains five terms, each originating of a physical mechanism. Starting from the most significant, the first term is from the dry atmosphere and is of the order of 250 at the surface, where the temperature is about 300 K and the pressure about 10^3 hPa. The two water vapour terms are due to the molecular and orientation polarizability of water vapour, and of the order 3 and 60 at the surface with $e \approx 15$ hPa. Often the least significant term is ignored or absorbed into the dry term, forming a term containing the total atmospheric pressure. The last term is due to the refractivity of liquid water, of which there is very little in the atmosphere. The second last term is due to the ionosphere, and is a first order approximation to the Appleton-Hartree equation (equation 1.5), which expresses the refractivity of a thin plasma, depending upon the electron density and the magnetic field, see sect. 1.1.2.

3.2 Water vapour profiling

From the occultation observations refractivity profiles can be calculated, and from this, density, pressure and temperature can be derived assuming a completely dry atmosphere as described earlier. If some constraints can be put on the atmosphere, the amount of water vapour can be derived. A well known method is assuming knowledge of the temperature profile (often obtained from a global weather model), but alternative methods are assuming a saturated atmosphere, assuming an exponential water vapour profile or assuming a ground temperature.

In this work results are obtained by the so-called inverse method (named in (Palmer et al., 2000)) used on GPS/MET and CHAMP occultation data. With this method the error of the assumed temperature maps directly into the error of the derived water vapour. Alternatively the variational approach uses the data in a statistical optimal way. Even though, the variational derived profiles are statistical optimal, the optimal retrieval requires substantial analysis of the errors.

The occultation method unfortunately does not allow for measuring the water vapour pressure above 15 km altitude. The reason for this is that the pressure is so low that water vapour contributes insignificantly to the refractivity because the GPS-signals probe virtually the number of (free) water molecules. This also indicates that it is absolute measures that are given, such as absolute humidity and partial pressure. The relative humidity can subsequently be derived only by further calculations of saturated water vapour pressure. Conversion between the various measures of water vapour is found in Appendix A.1.

Very large gradients in the water vapour distribution is expected for instantaneous measurements, whereas averaging over longer times effectively is a smoothing of all gradients (see e.g. (Wyngaard et al., 2001) fig. 3 and 4). An occultation measurement is so fast (each sample last of the order of 0.1 s or less) that a 'snap-shot' is taken of the atmosphere, hence the effect of the large gradients can be seen.

As additional information is needed for inverting equation 1.8, either an external temperature of water vapour profile can be used since both are available from the global numerical weather models. Evaluation of the differentiated equation 1.8, assuming no error in N and P (and ignoring the k_2-term), reveals that:

$$\Delta e \approx \frac{2TN - k_1 p}{k_3} \Delta T.$$

Typical values of $N = 300$, $P = 1000$ hPa and $T = 273$ K result in

$$\Delta e = 0.23 \Delta T \text{ or } \Delta T = 4.35 \Delta e.$$

As typical errors from numerical models are around $\Delta T = 2$ K and $\Delta e = 2$ hPa the best choice is to use the temperature profile to derive a humidity profile. An example of a derived water vapour profile is shown in figure 3.1 together with the corresponding model water vapour profile.

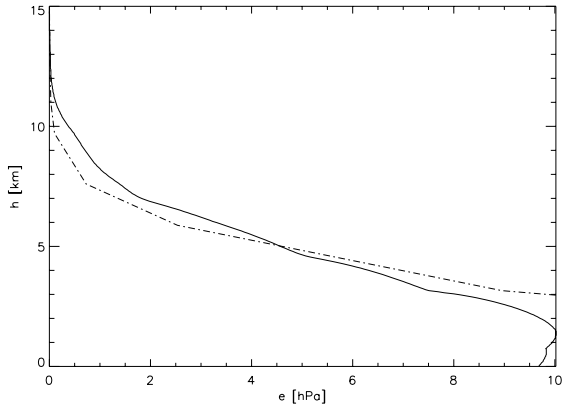

Figure 3.1: Comparison of occultation derived humidity profile (solid) and corresponding ECMWF humidity profile (dash-dot). Occultation parameters as in figure 1.3.

Below a few kilometres the discrepancy increases. This is expected to be the result of low signal to noise ratio, which makes the phase determination difficult for the receiver. The last two seconds of the occultation represent the lower 3 km, and inspecting figure 1.4 the last two seconds of the Doppler shift profile also behaves different from the trend in the curve. This further strengthens the suspicion that the

observations from the last few seconds are not reliable. If the same had happened for an occultation in more dry regions the inversion could result in a strong (unphysical) negative water vapour pressure (see section 4.1.3). A possible explanation is that the receiver has lost lock on the signal, and is performing something like a linear extrapolation of the excess phase (which would give a constant excess Doppler shift) in the search for the signal.

3.2.1 Using amplitude data

One of the very fine qualities of the GPS occultation data is that only phase measurements (corresponding to a time measurement) is used. For the more advanced inversion algorithms such as the Fresnel method also the amplitudes are used in order to reconstruct the entire electromagnetic field. Alternatively the amplitude data can be used together with the classical phase-retrieval. In this case the defocusing can be calculated and a comparison with the observed amplitude can reveal the amount of water vapour along the tracks because of water vapour attenuation. This attenuation is in general very small in the L-band (Liebe, 1989) and hence this method is rather noisy.

The amplitude data has been shown to contain sufficient information to derive temperature profiles (Sokolovskiy, 2000). In this case the defocusing is used to obtain information on the vertical structure of the atmosphere. Some problems exist in this method as the transmitter and receiver are not designed to be stable in power and gain respectively, and the multi-path occurrences have to be removed to maintain only the pure refraction effects in the signal.

3.3 Variation in refractivity parameters

Based on equation 3.1 the variations in the retrieved water vapour profile can be assessed as function of the involved retrieval parameters k_{1-3}. The accepted possible span of the retrieval parameters is found in (Bevis et al., 1994) and are listed in table 3.1. Several other atmospheric particulate constituents have been examined in (Solheim et al., 1999), with sand, clouds and heavy precipitation having potential to contribute significantly to the delay. But still, the contributions are smaller than the dry and wet gas terms of the refractivity.

As a result of inversions with various values of the retrieval parameters, the water vapour profile is examined. As expected variations in k_2 do play a minor role. Since equation 3.1 implies inter independency the variations can be calculated separately for each retrieval parameter. The variations in derived e are illustrated

Parameter	min	max	aver
k_1 (K hPa^{-1})	77.60	77.607	77.603
k_2 (K hPa^{-1})	64.79	71.6	69.05
k_3 (10^5 K^2 hPa^{-1})	3.701	3.776	3.741

Table 3.1: Possible values for the retrieval parameters k_{1-3}, as adapted from (Bevis et al., 1994).

as an envelope for one very moist occultation profile, this illustrates the maximal variations. One such curve is shown in figure 3.2, where the inversion has been performed with all combinations of max and min values from table 3.1. All the resulting profiles have been compared to find the maximum and minimum values.

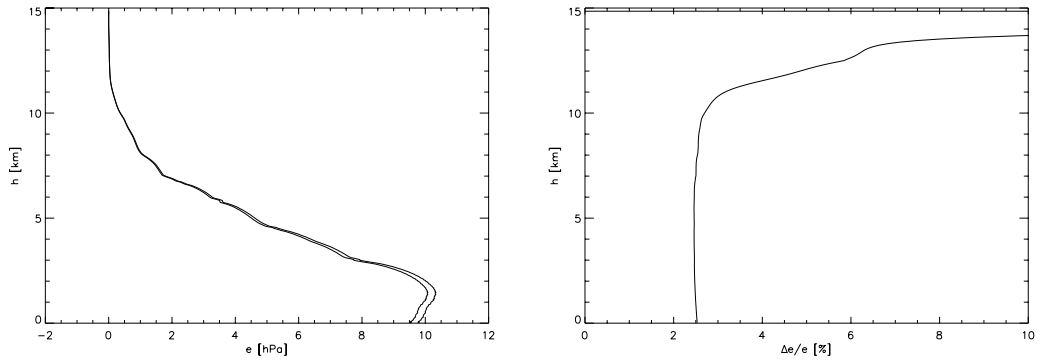

Figure 3.2: Resulting water vapour profiles from varying each of k_{1-3} according to max and min values in table 3.1. Left is the absolute values envelope and right relative. For occultation parameters as in figure 1.3, this hence being the reference. The line just below 15 km in the right figure is a numerical artefact.

The variations are seen to be rather small for the realistic variations of the refractivity parameters, on the order of 2.5% below 10 km. Above this altitude the relative variations increase, but at the same time the water vapour signal is almost 0. When comparing the importance of the various parameters, the variations in k_3 has the largest impact, even though the k_2 parameter is least certain. Some reduction in the general uncertainty of the derived water vapour profiles could be expected if the knowledge of the refractivity retrieval parameters is improved.

3.4 Tomography

Tomography is the technique of reconstructing an image of higher dimensions from observations of lower dimensions, e.g. line integrals in the same plane combined to give a 2D image of the plane (all the lines have to be 'calibrated' by crossing each

other). Well-known implementations of tomography are within medical imaging of of the human interior (see e.g. (Webb, 1988)).

In the specific case of the experiment consisting of a single GPS occultation the rays do not cross, and another coinciding occultation must be applied or coinciding ground based GPS observations must be used in order to perform a tomographic inversion. When using several occultations in one inversion at least two issues are important: The issue of the distribution of water vapour being the same at the different times of observation, and the issue of the scanning time of one occultation (approx. 100 s) being smaller than the typical quiet time of the atmosphere. Both issues involve typical scales of water vapour.

3.4.1 Temporal variations of water vapour

In order to determine the relevance of tomographic inversion the amount of changes within the probed region during an occultation measurement is to be considered. Several instruments make continuous integrated zenith measurements, e.g. ground based GPS and microwave radiometers. Mathematically the power of the structure function on different time-scales can be an indicator of this. On time-scales of 10^3 s the temporal structure function is (for both microwave radiometry and ground based GPS) found to be very small (Jarlemark, 1997), on the order of 0.5 cm^2 with an exponential decrease. This indicates that over the time of an occultation (typical at the order of 100 s) not much variation is in the atmosphere when considering the microwave regime.

3.4.2 Spatial distribution of water vapour

The spatial structure function can be linked to the temporal structure function using the average wind velocity (Jarlemark, 1997) assuming the flow to be 'frozen'. This is very fortunate, as the measurement of temporal structures is easy because it only requires a fixed instrument, where as the measurement of the spatial structure function requires instruments with different distances measuring simultaneously. The spatial structure function of the wet delay is found to be of the order of 10 to 50 cm^2 for scales between $2 \cdot 10^5$ and $2 \cdot 10^6$ m, and 0 for scales of several thousand kilometres as this is longer than the correlation distance of the water vapour distribution.

3.4.3 Applied tomography

Tomography has been applied to GPS measurements of the ionosphere for several years. The reason for the early development of GPS ionosphere tomography is that

Total Electron Content (TEC) is a direct measurement along the rays.

On the other hand performing GPS water vapour tomography involves separating the imprint of water vapour along each ray. A possible solution to the problem is to assume straight rays and at the same time assign a bending angle to each ray. Inverting this system in a discrete number of boxes/voxels will result in an image of the bending within each box, end hence indirectly the refractivity of each box. When using the ray approach it is implicit that the method used is geometric optics, and hence the vertical resolution is limited to about 1 km. The spatial scales of the water vapour and phenomena in the ionosphere are very different (with water vapour having the larger gradients). This enhances the requirement for dense observations for water vapour tomography. In order to get coverage to make tomography, the observation geometry has to be more substantial than just one occultation and one ground station because the observed rays might not cross at all. As discussed in the sections above a tomographic water vapour inversion requires several occultations to happen within ≈ 1000 s ≈ 15 min and a few 100 kilometers. For this to happen a small fleet of occultation satellites has to be available. Alternatively a reduced resolution can be applied.

The ionosphere tomography has been applied both on ground based networks and on occultation measurements. In Japan a dense network of approximately 1000 GPS receivers is continously mapping the ionosphere above Japan, as a by product of crustal observations. Similar (but smaller) networks are functioning all over Europe and USA. Space based ionosphere measurements from GPS occultation missions have also been used for tomography. This application might have a bright future for predicting space weather on routine basis.

For water vapour tomography a natural number along each ray is the integrated water vapour as the total nnumber of water molecules on the ray path maps to a delay (Bevis et al., 1994). This number is rather easily derived for ground based GPS receivers as the slant path delay, but for space borne GPS receivers it is not straight forward since there is an ambiguity between the effects of the neutral atmosphere and the water vapour in the refractivity. Reconstruction of water vapour images has been demonstrated in (Foelsche, 1999), but only from simulated ground based observations.

3.5 Multipath

The term multipath is used for the case when more rays reach the receiver at the same time after having traveled along different paths. Usually three types of multipath is considered: local multipath, atmospheric multipath and reflections. If the

receiver is of the most common type (phase locked) it will interpret the superposition of the rays as one signal with a fast changing frequency. This makes multipath observations difficult for receivers designed for tracking just one frequency, and the output is not fully reliably.

Local multipath is caused by reflections in local structures, such as antennas and solar panels. The reflections might be recognised because of their unchanging pattern relative to the receiver antenna. Atmospheric multipath is more rays reaching the receiver simultaneous due to atmospheric properties making the rays following different paths (see fig. 3.3 top and middle). The third multipath phemonenon is reflections from the surface of the Earth (see figure 3.3 bottom), most likely from water and ice surfaces as they are highly reflecting, especially under the small angle of incidence relevant in this setup.

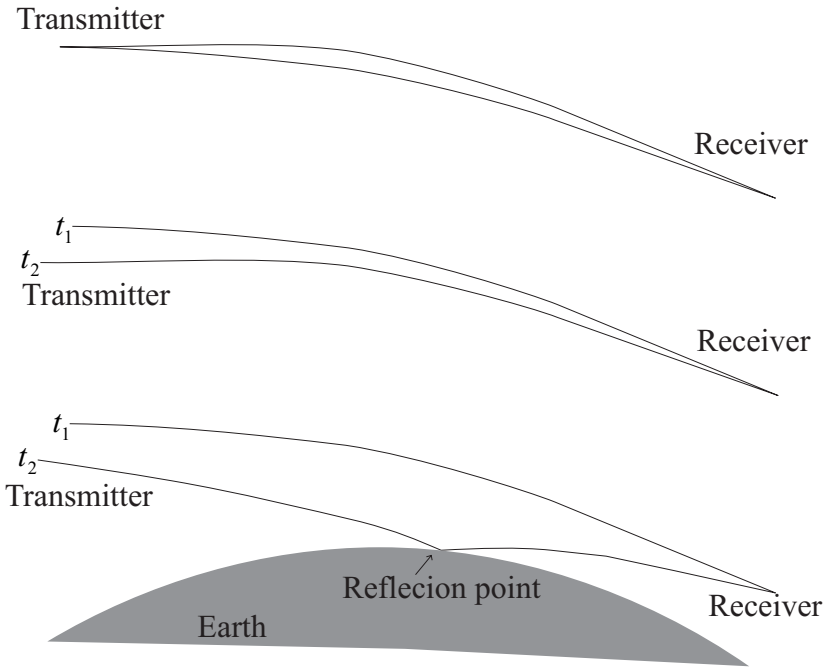

Figure 3.3: Sketch of the geometry of the three multi-path occurrence in the ray-concept. Illustrations are of atmospheric multi-path (top and middle) and surface reflection (bottom).

3.5.1 Local multipath

The local multi-path is caused by reflections in local constructions (surfaces, booms etc.). If 'local' is considered to be reflections within $R = 10$ m of the receiver, the maximal time-shift of the reflected signal is of the order of $\tau \approx 3 \cdot 10^{-8}$ s. This

short delay is often taken care of by the receiver itself, but can cause problems in the position solution.

3.5.2 Surface reflections

In recent years interest on ocean surface reflected GPS signals has grown as a tool for oceanographers to monitor the height of the ocean surfaces and measure the roughness of the oceans (a proxy for the wave height). Several articles have been published on the usability and detection of these signals (Lowe et al., 2002; Ruffini et al., 1999; Garrison et al., 2002; Igarashi et al., 2001). In (Beyerle and Hocke, 2001) actual surface reflections are reported in 28% of the L_1 occultation measurements performed by the GPS/MET experiment. At least the same relative amount of surface reflections is detected in CHAMP-data (Beyerle, private communication). Most of the surface reflections are identified to have reflection point over the oceans or polar ice-caps. The reflected signals are detected through sliding window Fourier[†] transform and appear in the spectrum as a weak straight line moving away from the centre frequency. This is seen in figure 3.4 leaving to the right of the centre frequency at around 62 s and reappearing at the left side of the figure at 75 s due to wrap-around.

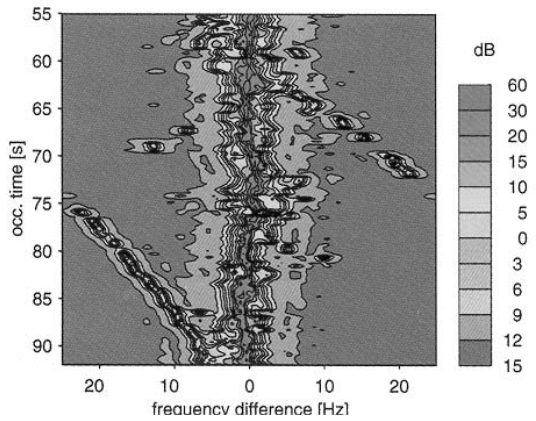

Figure 3.4: Temporal evolution of radio hologram power spectrum of GPS/MET occultation 10 from February 10th 1997. The reflection is seen as the sloped line away from the centre frequency, from (Beyerle and Hocke, 2001).

The transformation of the right hand circular polarised GPS signals into left hand circular polarised signals in a reflection is at present not used for detection of reflected signals.

[†]Jean Baptiste Joseph Fourier, March 21st 1768 - May 16th 1830. French mathematician.

3.5.3 Atmospheric multi-path

Basically atmospheric multi-path requires that the magnitude of the bending angle increases locally with height as $d\alpha/da > 0$, which is not the general case for an exponential atmosphere. This requirement states that high altitude rays bend more than low altitude rays so that more rays can cross. Even if this is fulfilled the receiver might not experience multi-path as the rays might cross further away than the receiver orbit.

Simple considerations of the geometry of a multi-path situation reveals that

$$\sin(\Delta\alpha) \approx \Delta\alpha > \frac{\Delta a}{z}$$

where $\Delta\alpha$ in the bending angle difference between the two rays performing multi-path, Δa the corresponding height difference and z the distance between the receiver and the tangent point. In differential formulation the requirement on bending angle gradients is :

$$\frac{d\alpha}{da} > z^{-1}$$

Setting $\Delta a \approx D_{fresnel} \approx 1$ km and $z \approx 3000$ km gives $\Delta\alpha \approx 3 \cdot 10^{-4} = 0.02^\circ$ which is a small fraction of the observed bending angle in the troposphere (of around 1°). Then AM could be expected to be a common phenomenon where the refractivity is high (and highly variable) as in the troposphere.

At conventional receivers atmospheric multi-path is experienced as fast changes in both phase and amplitude (possible ending up in loss of lock) but more advanced receivers, capable of open loop mode, track the signal at a broader spectrum, and is hence capable of maintaining the signal for much longer.

Inversion in case of atmospheric multi-path is in general complicated and the common geometric optical approach is not working thus other methods have to be used:

- The back-propagation method (Gorbunov et al., 1996a) is a method of recalculating the appearance of the observations at an observation plane closer to the tangent point, where the multi-path effect is absent.

- The Fresnel inversion (Mortensen and Høeg, 1998) makes use of several samples covering one Fresnel zone and several zones overlapping. This makes inversion with high vertical resolution possible.

- Radio holographic inversion (Hocke et al., 1999; Gorbunov et al., 2000) performs a sliding aperture spectral analysis to identify the rays.

- Canonical transform (Gorbunov, 2001) uses a mathematical transform, closely related to the Fourier transform, to perform a back propagation in a more stable way.

One strong observational indication of multi-path is found in GPS/MET and CHAMP occultation data as the amplitude measurements often show large variations at the last 10 seconds, usually corresponding to the lower-most $10 - 15$ km.

The approximate distances involved are estimated previously to $R_{GT} \approx 26000$ km and $z \approx 3000$ km. Denoting the maximal ray separation Δh the delay caused by taking the 'deroute' is (to the first order):

$$\Delta L = \frac{1}{2}\Delta h(\frac{1}{R_{GT}} + \frac{1}{z})$$

which for a maximal separation of $\Delta h = 1$ km is $\Delta L = 0.19$ m - very close to one wavelength. In the time elapsed during the deroute (about 10^{-9} s if only the geometric delay is considered) the LEO has moved only 0.005 mm which has no effect on the ability to receive the ray, and a superposition of the two rays is observed.

Another visualisation of multi-path is involving wavefronts as illustrated in figure 3.5. The front is 'folded' becoming 'self-intersecting' as it passes an obstacle - in this case some region of larger refractive index. At any observer position in the shaded cone there are three directions which are perpendicular to the wave front and hence are seen as images or rays. The rays might not reach the observer at the same time, but as pointed out above, the time difference in the case of GPS occultation measurements is so small that the rays seem to reach the receiver simultaneously. The cone is called the caustic. Inside the caustic the concept of wavefronts and rays is not reliable, so the inversion method 'back propagation' has been developed to trace the individual rays to a region outside the caustic, closer to the tangent-point of the rays (Gorbunov et al., 2000). Unfortunately this is not always possible if the structure of the caustic(s) is complicated.

For studies of the phenomenon a ray-tracer can do a decent job in resolving if multi-path occurs (but not the complete solution of ray-paths), but for operational use the time required for a ray-tracer to search the entire space of ray directions is so large that other methods have to be developed (Cupillard, 1999).

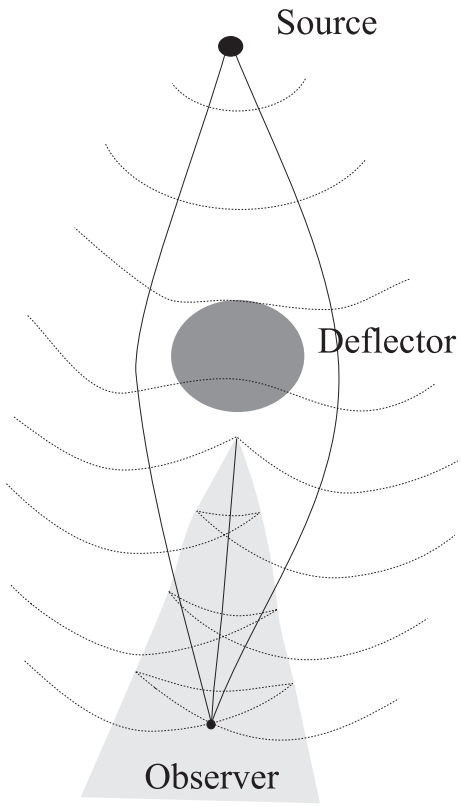

Figure 3.5: The concept of multi-path with a wavefront. The wavefront is symbolised by dashed lines, rays are solid lines defined by being perpendicular to the wavefronts (from the viewer three rays are observed, one being the result of the 'folded' wavefront). The light gray region marks the caustic where more than one ray reach every point.

3.6 Examination of one refractivity field

On the basis of a global refractivity field generated from a global weather model (in this case from ECMWF at February 11th 2001 12:00 UTC) a lower limit on the occurance of critical refraction and atmospheric multi-path can be estimated. Due to the limited resolution (0.5 by 0.5 degree) the searched structures can be more frequent than derived from the global field, as even very small scale gradients can cause them. The field is generated from temperature, pressure and humidity fields and calculated from equation 3.1. The result is a refractivity field with 259200 'profiles' each consisting of 64 levels. Examples of the appearance of the interpolated 1500 m level is found in figure 3.6, and for 500 and 5000 m in figure 3.7.

Distribution functions of the refractivity is bimodal at many heights, especially the lower ones, as seen in figure 3.8. The high refractivity peak originates from the polar region and the low refractivity peak from the mid latitude and polar regions with a rather sharp border at around 30 degrees. The high-refractivity peak weakens

for higher layers in the atmosphere because the water vapour plays a less important role in the total refractivity.

In the map many small scale variations are observed, such as water vapour transport from equator to the poles along thin streams.

In the entire refractivity field a search for multi-path is performed, based on the following criteria (Kursinski et al., 2000):

$$\frac{d^2N}{dr^2} < 0 \text{ and } \frac{d|N|}{dr} > 0$$

The search criteria were fulfilled in ≈ 570 data points corresponds to about 0.2% of the Earth surface. It is noticed that no multi-path phenomena are found in the polar regions (pole-wards from 60 degrees north and south), and very few occurances are in the region close to equator (in between 10 degrees north and south). The lack of multi-path points in the polar regions is no surprise as the large gradients are mainly a result of water vapour which is almost absent there. More surprising is the lack of multi-path in the equatorial region as huge water vapour gradients could be expected. A possible explanation is that the gridding and/or model physics is not sufficiently detailed to capture all the variations. On the other hand it is possible that the equatorial region is steady enough in temperature and humidity that no large vertical gradients exist.

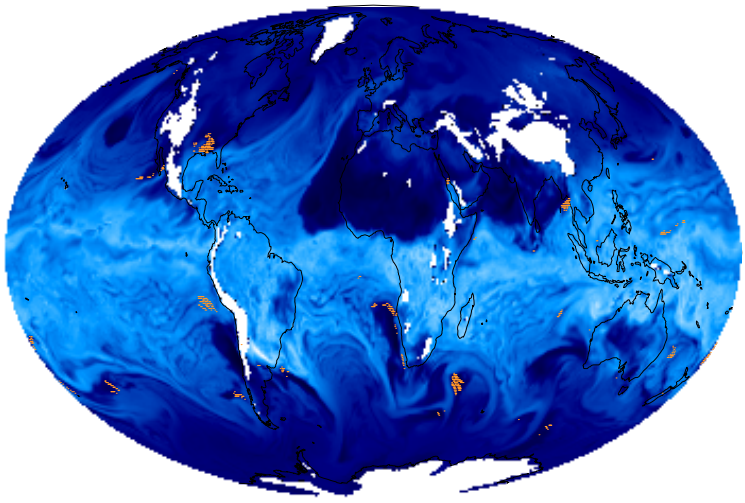

Figure 3.6: Map of the 1500 m level global refractivity field generated from ECMWF temperature, pressure and humidity on February 11th 2001. White regions are where land reaches the interpolation level, dark blue low refractivity and light blue high refractivity. Positions fulfilling multi-path criteria are marked orange.

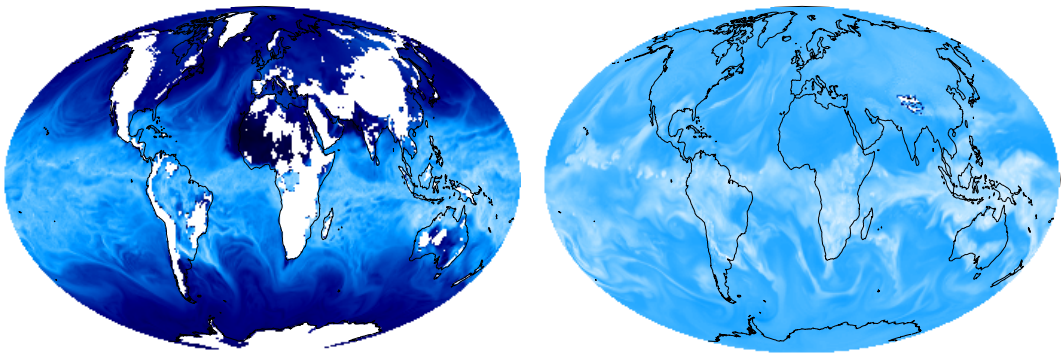

Figure 3.7: Map of the 500 and 5000 m level global refractivity field. Light blue is high refractivity. The multi-path regions are not marked in these maps.

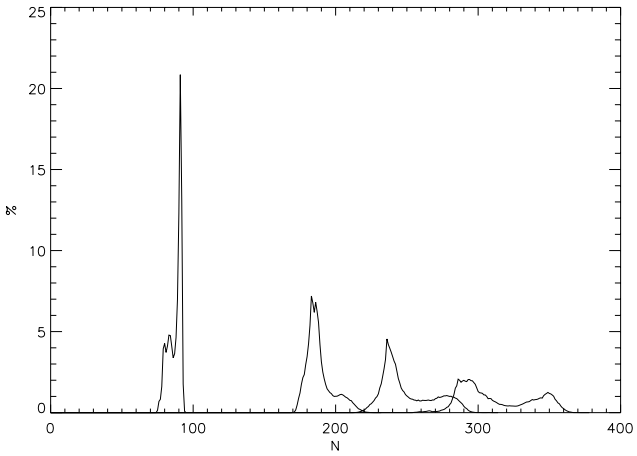

Figure 3.8: Distribution function for refractivity at the four levels 500, 2000, 4000 and 10000 m from the right.

3.6.1 Search for critical refraction in refractivity fields

In the same field a search for critical refraction is also relevant. The outcome of such a search indicates how often signal tracking becomes very difficult as the signal strength is strongly decreased due to defocusing. The criterion is stated above as $\frac{dN}{dr} < -10^{-6}R_c \approx -0.157$ m^{-1}. From this analysis, only a lower limit is put on the area in which critical refraction can occur, similarly, real atmospheric structures exist on scales much smaller than resolved by the model. The search reveals that in the given field critical refraction is found in 7085 bins, corresponding to 2.7% of the bins. The distribution in latitude vs. height with respect to the orography is plotted in figure 3.9 and in latitude-longitude on the map in figure 3.10.

The distribution in height is divided into bins as a result of the height levels of the model field. A huge population is found just below 50 m (more than half the

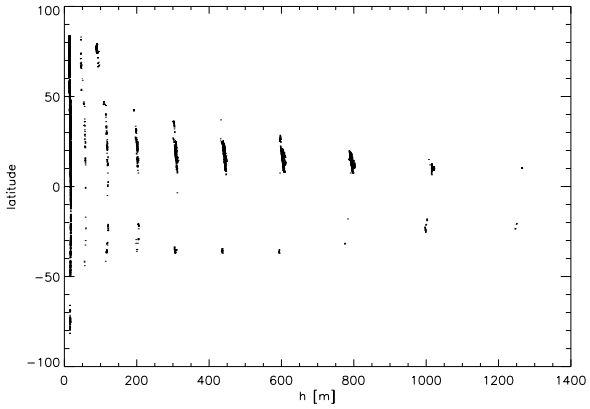

Figure 3.9: Height of critical refraction points as function of latitude.

points). On the map the points are colour coded according to the height of the critical refraction, with red being low (below 50 m), orange being mid (between 50 and 200 m) and yellow above 200 m.

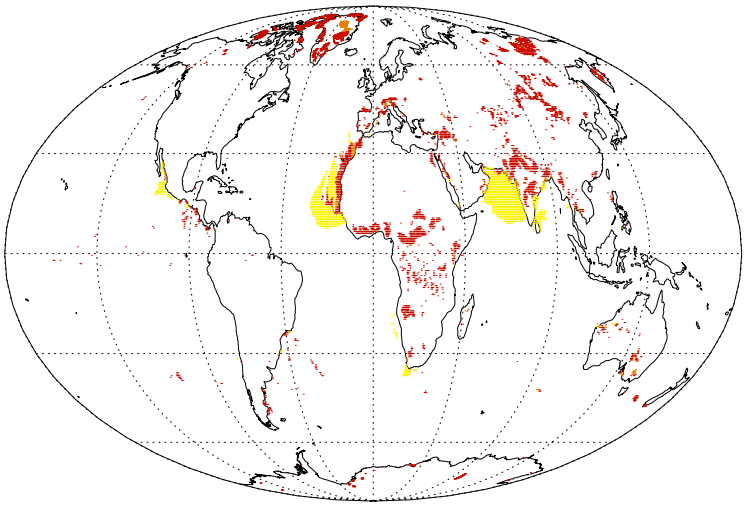

Figure 3.10: Position and (crude) height of lowest critical refraction points. Red being low, orange mid, and yellow high critical refraction points.

Over Greenland much of the low altitude critical refraction is found, and the high altitude critical refraction is found on many west-coasts about $20 - 30°$ northern latitude.

The low altitude critical refraction is probably of no significant influence to occultation measurements as profiles below 50 m are influenced by so many other phenomena disturbing the refraction. Furthermore they might not be reliable in this analysis as they are found in the lowest model level over an area of the world with complicated weather, especially at low heights. The significance of the critical

refraction layer can be examined by the thickness of the layer as illustrated in figure 3.11.

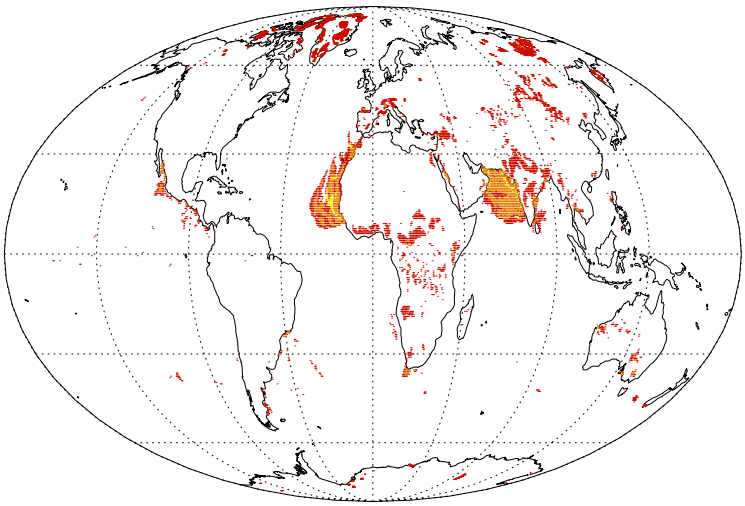

Figure 3.11: Thickness of the critical refraction layer. Red thinner than 50 m, orange between 50 and 200 m and yellow thicker then 200 m.

Many of the regions are covered only by layers of less than 50 m thickness. This is comparable to the raw resolution of the occultation measurements as demonstrated earlier. The large and high critical refraction zones on the west coast of North America, Africa and India are also of significant thickness, making them significant in occultation observations. In addition they extend between many resolution points, adding up to several hundreds of kilometer (Kursinski et al., 2000).

3.6.2 Rejected occultations

In several studies (e.g. (Kursinski and Hajj, 2001; Marquardt et al., 2001)) a fraction of 16 to 21% of all water vapour profiles has been rejected. The rejections are often based on retrieval of negative water vapour pressure which is unphysical. But as the observations are real and show no signs of errors, something interesting is happening in approximately one sixth of all occultations. The reason for the unphysical profiles could be physical properties in the atmosphere making tracking difficult (multipath, cycle slip or similar).

3.7 Open-loop receivers

At present most GPS receivers are of the closed loop type, indicating that the receiver keeps track of the frequency (and amplitude) of the peak of the signal from

each sample to the next. In a highly variable medium the received frequency and amplitude might change considerable from sample to sample, ultimately resulting in lost phase lock, as has been observed for most occultations as they often end several kilometers above the Earth's surface as demonstrated later for both GPS/MET (section 4.1.2) and CHAMP (Section 4.2). This problem can to some extent be dealt with if the receiver is programmed to continue measuring for a given time after lost phase lock or if the loop is sufficiently tolerant. The 'measurement' after lost lock will be an extrapolation but the receiver might regain lock on the signal if the disturbance was only transient. This method is called fly-wheeling. Under most circumstances fly-wheeling will extrapolate from the last observed phase. In case of water vapour present in the atmosphere the bending angle (and hence phase) will increase faster than with a dry atmosphere because of the lower scale height of water vapour. Hence the data coming from fly-wheeling will tend to underestimate the refractivity. This probably is seen in several cases as negative values for water vapour pressure. The derived negative values of water vapour might also be a result of strong gradients in the refractivity making either the inversion go wrong or the receiver to make cycle slips (it looses track of the phase and slip 2π on the phase).

An alternative to fly-wheeling is to sample the entire spectrum within a given frequency range and transmit it for analysis. This 'open loop' approach makes no assumptions for the $n+1$'th sample on the n'th sample, hence the signals should be detected all the way to the surface of the Earth. Unfortunately the bandwidth required for transmitting this type of observation is much higher than for the closed loop receivers. For the early planetary occultation experiments this type of open-loop observations were performed with a subsequent reprocessing of the recorded spectra. In figure 3.12 this type of observation is illustrated, showing a power spectrum at each temporal sample.

Recently several papers have been presented on open loop technique applied to the radio occultation method (Sokolovskiy, 2001) as this method could lead to better temperature and water vapour profiles.

The open-loop mode is especially important when atmospheric multi-path (see section 3.5) is severe. In case of multipath more signals of slightly different frequency interfere at the receiver. Hence a power spectrum of the received signal will reveal more peaks - one for each ray in case the ray-analogy is applicable. Since the signal emitted is continous the observation will allways be a spectrum. Open loop is also called raw sampling, refering to the sampling of non-processed data.

Inversion of open loop observations

With open loop observations the local electromagnetic spectrum is measured, indicating that an inversion method taking into account the entire field propagation could be applicable. A more modest approach could be to make on-ground routines to trace the most dominant frequencies. In this approach the present inversion strategy can to some extend still be used and fast results can be achieved, but much information remains unused.

3.8 Discussion of other methods

Several other methods exist for measuring water vapour profiles in the atmosphere, either in situ or remote by various methods.

A well known method is to lauch a radiosonde which measure the humidity as a balloon ascends and relays the measurements to ground. This type of measurements has a high vertical resolution, on the order of tens of meters. The measurements takes long time as the balloon only has a vertical velocity of about 300 $\mathrm{m\,s^{-1}}$, resulting in a measuring time of more than an hour. During this time the balloon can drift sideways. The measurement quality is rather good, but under cold conditions the instruments can be less reliable. Radiosondes are launched mainly from land, and from the industrialised countries, causing a limited coverage. In short the instrument makes a sample of local measurements over some time, adding up to a

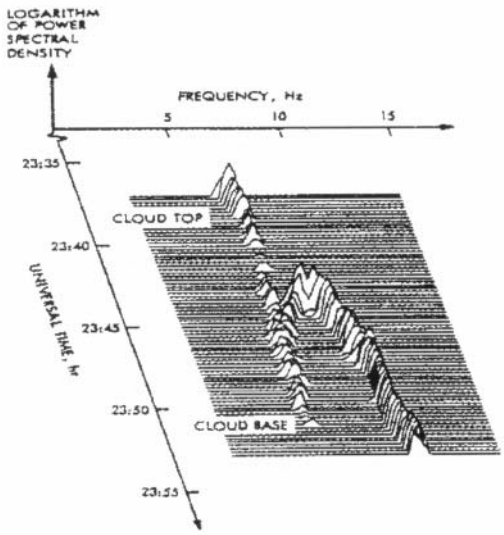

Figure 3.12: Time-sequence of power spectra of open-loop observations from the Voyager 2 mission during Uranus occultation. Notice the multipath phenomenon occuring between 23:44 and 23:52. From (Yunck et al., 2000).

vertical profile with a drift.

Alternatively the satellites often have nadir viewing instruments observing in many spectral bands for determining the conditions in various atmospheric layers. The more bands the more layers, but the inversion of this type of measurements can be complicated with calibrations and assumptions of radiation transfer functions. The method has a good horizontal resolution, but even if the vertical resolution can theoretically be at the kilometer level the inversion can complicate the data interpretation.

As conclusion the various measurements have their own advantages and support each other, either in the resolution or coverage.

Chapter 4

Observations from satellites

A convenient feature of GPS occultation measurements is the reliability of derived temperatures between different receivers due to the measurements being time and not amplitude. This makes it possible to compare measurements from the instruments GPS/MET (USA) and CHAMP (Germany) without further reduction and inter calibration of data to a common reference. In the following the distribution of occultations has been examined for both GPS/MET and CHAMP. The differences mostly reflect the different orbital parameters of the two satellites. Also the penetration depth has been examined for the two satellites, variations here reflect versions of software on the receivers.

Temperature and humidity profiles have been compared for both satellites to corresponding profiles from a global weather model.

Data from Ørsted have not been included due to the problems in the L2 detection which is on a very low level. Furthermore the amount of occultations reaching deep into the atmosphere is very limited.

4.1 GPS/MET

The GPS/MET experiment was launched as a proof of concept for the GPS occultation method. It was carried out by an American group led by the UCAR (University Corporation for Atmospheric Research) and mounted on the satellite MicroLab1, which was launched on April 3rd 1995. The occultations of greatest interest are made in the so-called PrimeTimes where AS (AntiSpoofing - a military coding making it impossible to make fake GPS satellites) was off, as this enabled higher precision in the derived profiles. For an overview of the occultations from the entire GPS/MET project see (Rocken et al., 1997).

4.1.1 Distribution of measurements

One of the benefits of the GPS occultation technique is that the distribution of observations is smooth, as compared to e.g. radiosondes which have a strong over-density in the highly industrialised regions (North America and Europe), a weak over-density in Russia, India and China and a strong under-density on the southern hemisphere and over the oceans (see figure 4.2). Below the various aspects of distribution is measured and illustrated, covering direct maps, smoothness-test, depth-distribution.

Geographical distribution

Below are plots of the distribution for the four PrimeTimes (figure 4.1) and a corresponding plot for radiosondes at one specific time (figure 4.2). The maps are presented in the Mollweide projection as this is area conserving, making the occultation density variations appear directly.

The four primetimes are listed in table 4.1, notice a huge variation of the number of occultations used in each primetime, even though they span about the same time, actually PT4 is containing most occultations but last shortest and PT1 last longest but contains least occultations.

Kolmogorov-Smirnov test

To test if the occultations have a uniform global distribution a Kolmogorov-Smirnov test is appropriate (see e.g. (Press et al., 1992)[ch. 14.3]). As the two coordinates (latitude and longitude) are independent, it can be applied independently in latitude and longitude. To perform the test, a model describing the expected cumulative distribution has to be determined. In latitude a cosines-distribution is expected and in longitude an uniform distribution, leading to the theoretical cumulative distributions

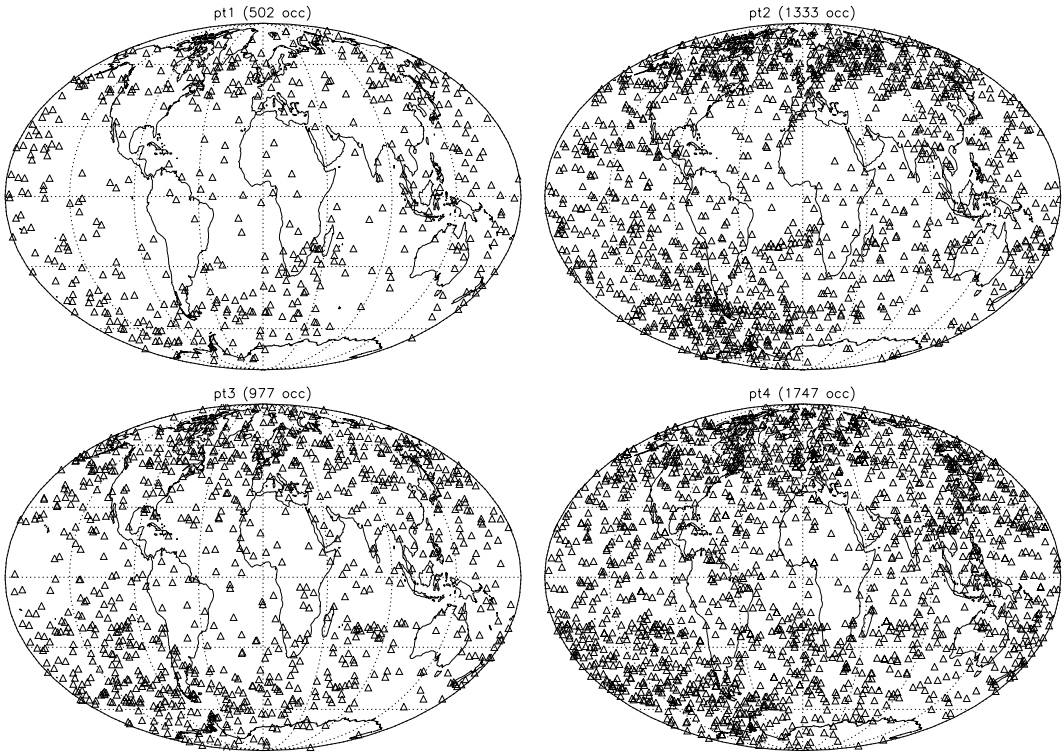

Figure 4.1: Distribution of occultations in the four primetimes.

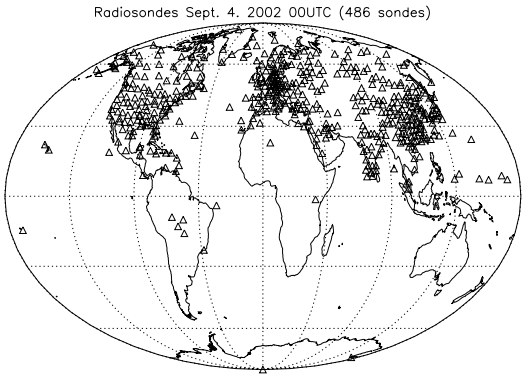

Figure 4.2: Distribution of radiosonde measurements on September 4th 2002, 00 UTC. As radiosondes are being launched from the same stations the distribution does not change much over the years.

in latitude and longitude for an even distribution:

$$P_{lat}(x) = \frac{\sin(x)+1}{2} \quad \text{and} \quad P_{lon}(x) = \frac{x+180}{360}$$

The normalisation is computed in order to have 0 at the South Pole and Greenwich 0-meridian and 1 at the North Pole and the Greenwich 360-meridian.

One parameter derived from the KS-test is the (simple) maximal value D of the absolute difference between the expected and the measured cumulative distribution functions. This can take any value between 0 and 1, with a low value signifying close agreement. Now the significance level $Prob$ of a derived D can be calculated, resulting in $Prob$ being small if the two distributions are different.

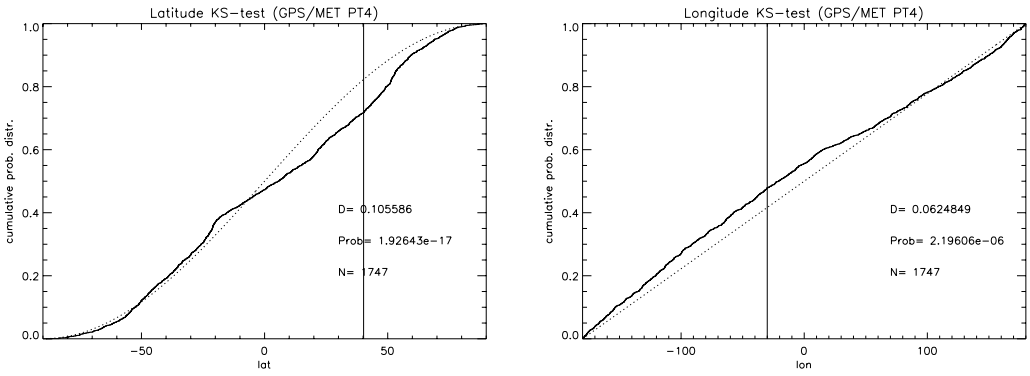

Figure 4.3: Kolmogorov-Smirnov test for PT4. The solid line is the data and dotted line the theoretical distribution. The solid vertical line is the position of maximal difference between the two distributions. D, $Prop$ and N are indicated for each distribution.

The K-S test for the four primetimes are plotted in figures 4.4, 4.5, 4.6 and 4.3 and for one radiosonde (figure 4.7) launch time (several years later, but the distribution has not changed much over the last years). Each plot contains, besides the curves, numbers describing the quality of the fit. The vertical line in each plot

PT	dates	Processed profiles
1	95.111-95.142	502
2	95.170-95.192	1333
3	95.283-95.293	977
4	97.033-97.047	1747

Table 4.1: The time span of the four GPS/MET primetimes listed as year.day-of-year. Not all the days in the time intervals necessarily contain data. Also listed is the number of profiles processed in this study for each primetime

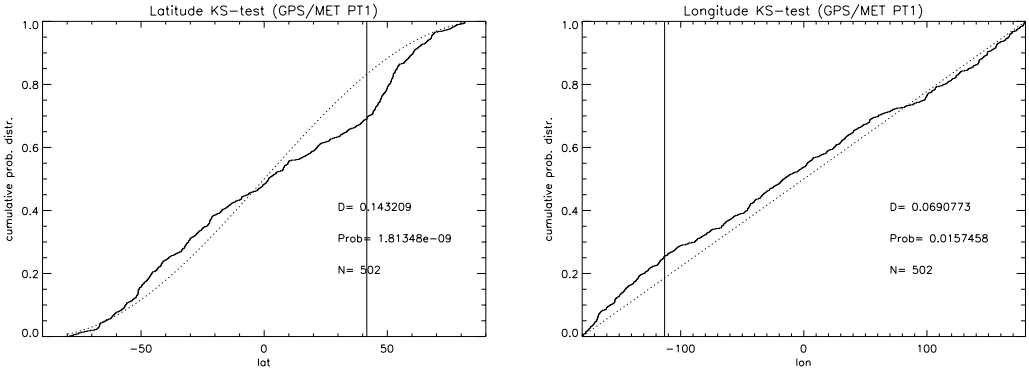

Figure 4.4: Kolmogorov-Smirnov test for PT1. Symbols are as in Figure 4.3.

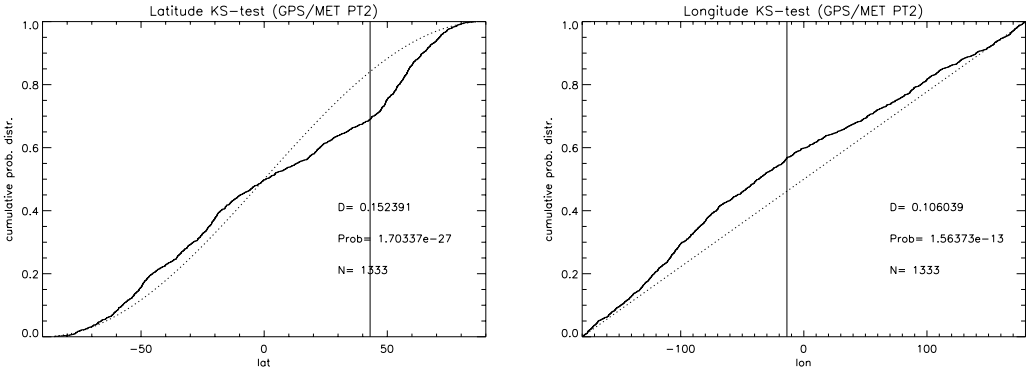

Figure 4.5: Kolmogorov-Smirnov test for PT2. Symbols are as in Figure 4.3.

is the latitude or longitude where D is determined. The numbers are also found in table 4.2.

Apparently the occultations are not spread uniformly on a global scale in a statistically sense, but still the distribution is much more homogeneous than for the radiosondes. The deviation from the expected latitude distribution takes place in the equatorial region where a deficit of occultations is observed. The reason for this deviation from a uniform distribution is the orbit configuration of GPS/MET. The largest distance D is in all cases (except the radiosonde) found close to 40 degrees north, but it has been building up from just below equator. This feature has to be taken into account when the global distribution of useful water vapour profiles is to be examined.

In longitude no general trend is observed except for a weak over density of profiles west of the Greenwich meridian as a result of the under density over Africa. This under density is a result of an not optimal ground station coverage for occultations happening over Africa.

The radiosondes are virtually only measuring over the Northern hemisphere over North America, Europe and East Asia, as also derived from the KS test which

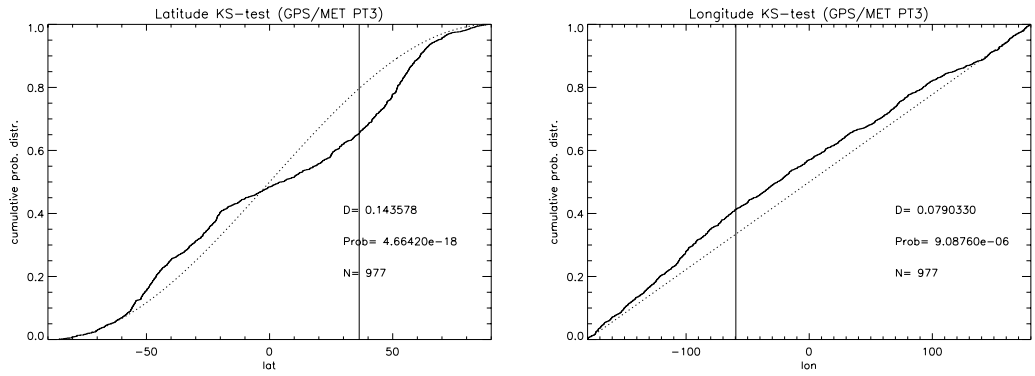

Figure 4.6: Kolmogorov-Smirnov test for PT3. Symbols are as in Figure 4.3.

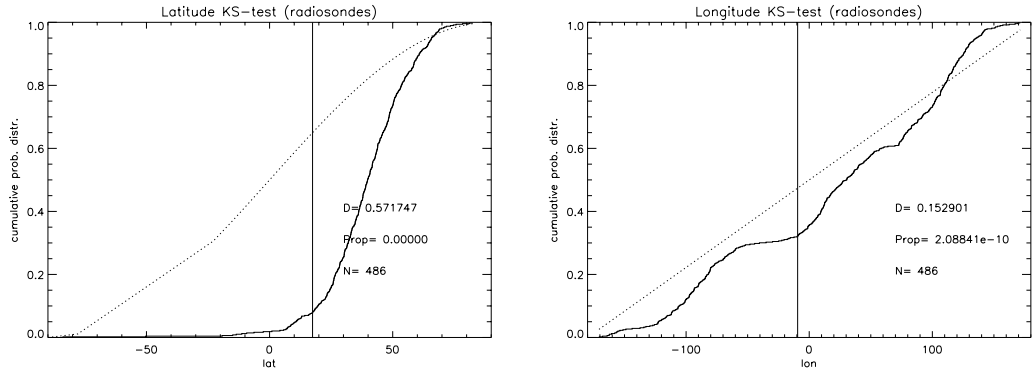

Figure 4.7: Kolmogorov-Smirnov test for radiosondes. Symbols are as in Figure 4.3.

express that the latitude distribution certainly is not even and the longitude distribution being far from even.

4.1.2 Depth of measurements

Ideally all occultations end (or begin in the case of rising occultations) at the surface of the Earth. In reality this is not very often the case as the receiver often is not capable of tracking the signals in the lower troposphere (see section 3.7 about loss of track and open loop receivers) and through the planetary boundary layer (PBL) due to the large irregularities here, caused mainly by water vapour.

Based on this argument it is expected that more occultation measurements reach the ground at the dry regions near the poles than at the moist region near equator. This expectation is fully supported by the statistical distribution of the lowest height reached by each occultation in a given region. The curves for PT4 are found in figure 4.8. The separation on latitude bands has been made at 30° and 60° north and south, resulting in fractional areas A covered by the three regions (on one hemisphere) corresponds to $A_{pol} = 0.07$, $A_{mid} = 0.18$ and $A_{equ} = 0.25$.

Notice that regions expected to be dry (polar regions) have many occultations reaching deep - more than half the occultation end below 1 km. On the other hand the warm equatorial regions (expected to contain much water vapour due to the higher temperature) have most of the occultations ending at $3-4$ km, and very few reaching into the lowest kilometre.

Corresponding statistics for the other three primetimes of GPS/MET reveals almost the same pattern as seen in figures 4.9, 4.10 and 4.11. The variations are results of mainly seasonal variations. Only primetime 2 is special in the large amount of occultation reaching the Earth's surface. This could lead to the thought that fly-wheeling has been implemented during PT2, as the similar examination for CHAMP (see section 4.2) reveals the same result when not removing fly-wheeling samples at the end of the occultations. Modifications like this to the receiver in exactly PT2 is noted in (Kursinski and Hajj, 2001).

To test if the north and south curves are similar in a statistical manner, a χ^2-test is performed, comparing the distribution functions for the two hemispheres. (Press et al., 1992)[eq. 14.3.2] :

$$\chi^2 = \sum_i \frac{(N_i - S_i)^2}{N_i + S_i}$$

since the distributions are normalised. Here N_i is the number of occultations in the ith northern bin and S_i the number in the corresponding southern bin (same absolute latitude). To derive the probability of the two distributions (north and south) being different is then calculated from the incomplete gamma function Q, with ν being the number of degrees of freedom (in this case the number of bins with both distributions being non-zero - minus one for the one degree of freedom 'used' in normalising):

$$Q(\chi^2|\nu) = Q(\frac{\nu}{2}, \frac{\chi^2}{2})$$

hence a small number indicates a significant difference between the two distributions.

	Latitude		Longitude		
	D	Prob	D	Prob	N
PT1	0.143	$1.81 \cdot 10^{-9}$	0.069	0.016	502
PT2	0.152	$1.70 \cdot 10^{-27}$	0.106	$1.56 \cdot 10^{-13}$	1333
PT3	0.144	$4.66 \cdot 10^{-18}$	0.079	$9.09 \cdot 10^{-6}$	977
PT4	0.106	$1.93 \cdot 10^{-17}$	0.062	$2.20 \cdot 10^{-6}$	1747
Radiosonde	0.572	0.00	0.153	$2.09 \cdot 10^{-10}$	486

Table 4.2: The results of the KS-test performed on the four primetimes and one radiosonde launch time.

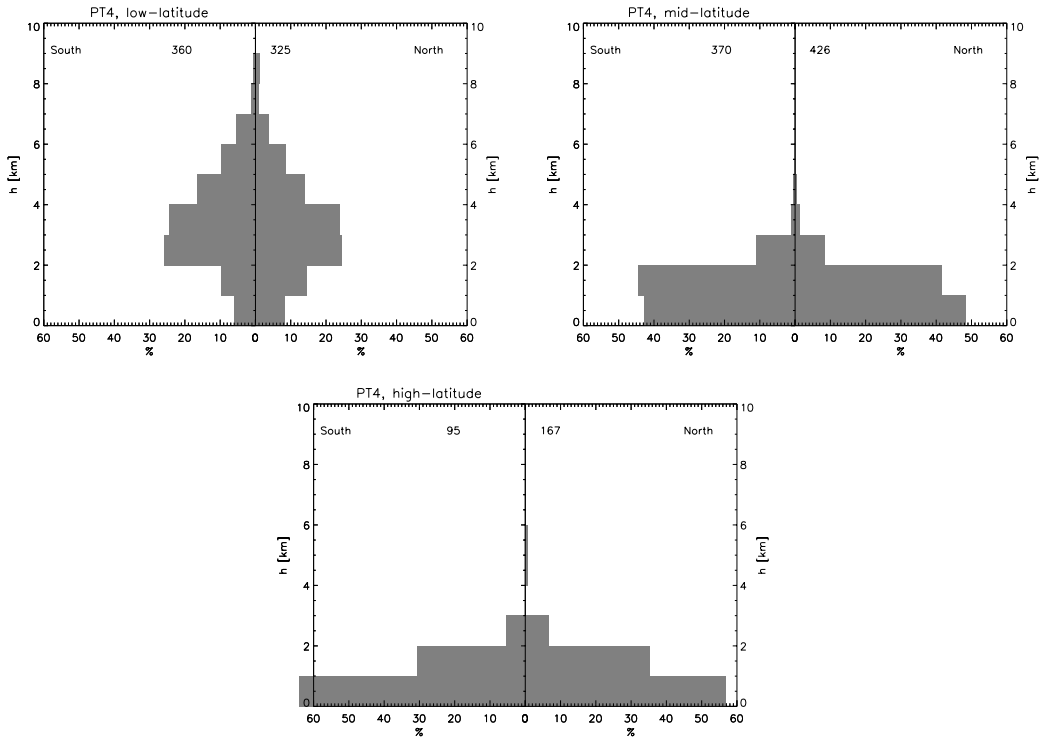

Figure 4.8: Distribution of lowest point in occultations for primetime 4. The three curves represent equatorial, mid-latitude and polar regions. The numbers are fraction in each (1 km) bin as function of height. The number of occultations in each latitude band is printed, but not corrected for the different area covered by the regions.

latitude	PT1 (April 1995)	PT2 (June 1995)	PT3 (Oct. 1995)	PT4 (Feb. 1997)
high	0.000	0.759	0.556	0.710
mid	0.114	0.021	0.373	0.956
low	0.631	0.592	0.125	0.980

Table 4.3: The probability that the north and south distributions are different based on the χ^2 test. A small value indicates that the two distributions are different.

Table 4.3 contains the resulting probabilities. Most of the differences in the reached depth is caused by changes in the on-board software, making inter-primetime comparisons difficult. In general PT4 tends to deliver the same north and south penetration profile as the χ^2-values are close to one.

Some caution has to be made with the derived heights as they are relative to the WGS84 geoide, not the real physical topography of the Earth. If height of the ray tangent point is transformed into topographic heights some differences are seen. Among the more curious ones, is a set of occultations reaching below the surface of

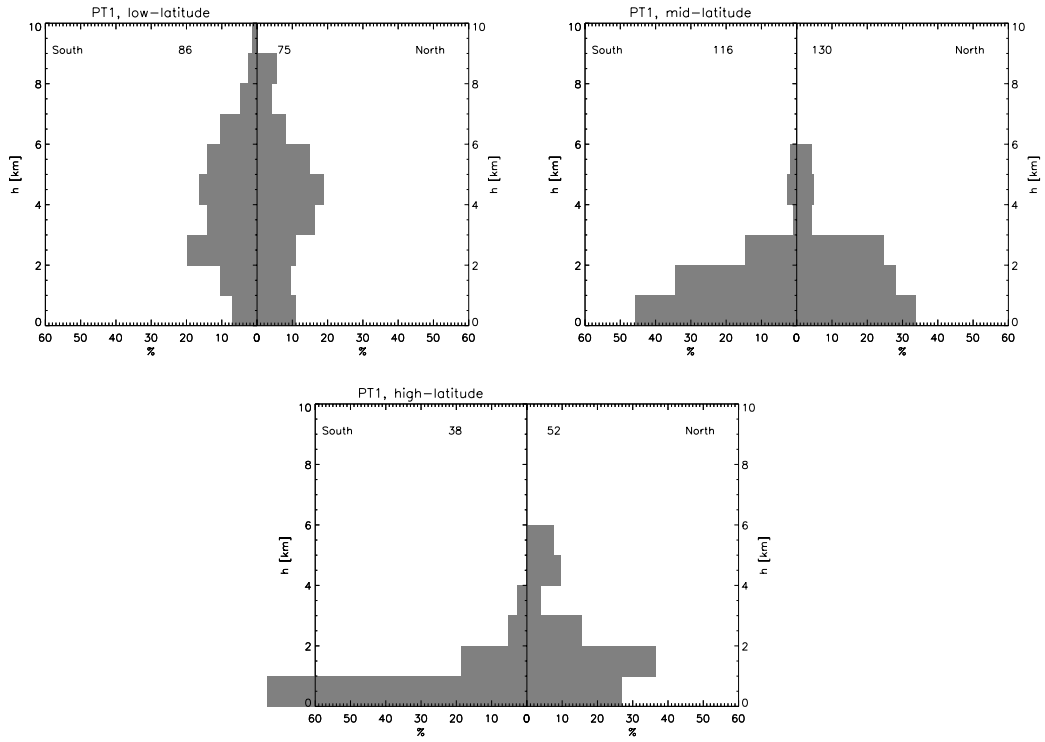

Figure 4.9: Distribution of lowest point in occultations for primetime 1. Notation like figure 4.8.

the Earth.

4.1.3 PT4 humidity profiles

For PT4 humidity profiles have been derived on the basis of ECMWF temperature profiles from the temporal closest model run, but interpolated in space to the occultation position. The derived humidity profiles have been statistically compared to the corresponding profiles from the ECMWF global weather model. The results are plotted in figure 4.12 for all the profiles with Integrated Precipitable Water (IPW) greater than -1 hPa. This selection removes the extreme outliers (see below).

As can be seen the average error increases downwards, even when the outliers with the strong negative humidities have been removed. At maximum the average difference is on the order of 1.5 hPa and the standard deviation of 3 hPa, obtained at about 1 km altitude. This standard deviation grows to 5 hPa at the surface where the average difference has dropped to about 0. There seems to be a negative trend in the statistics, but at no altitude is it significant in the sense that the average difference is larger than one standard deviation. The number of available profiles decrease rapidly below 5 km which is expected as the signal is often lost close to and in the planetary boundary layer.

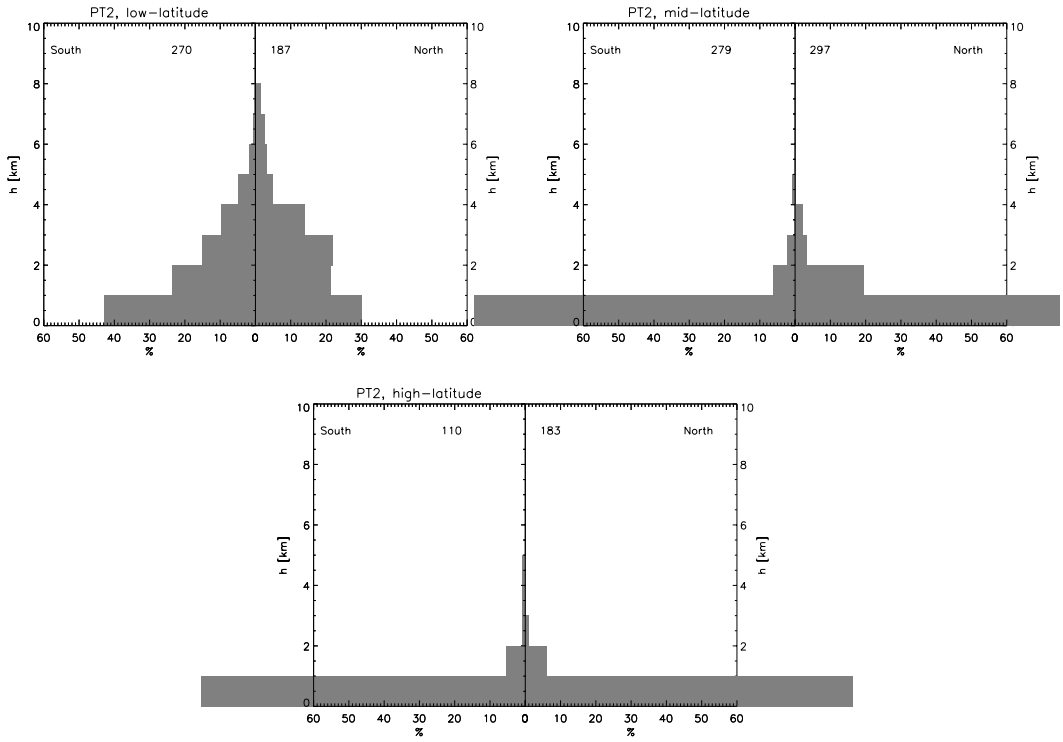

Figure 4.10: Distribution of lowest point in occultations for primetime 2. Notation like figure 4.8.

Outliers

In the sample of GPS/MET PT4 water vapour profiles a substantial fraction have unphysical properties, such as strong over-saturation or negative water vapour pressure. The explanation can to some extend be noise since the derived moisture profiles depend upon the model temperature profiles which have known errors in the range $1-2$ K, resulting in errors of up to 1 hPa. But even taking this into account leaves some profiles which would require temperature errors an order of magnitude larger which is highly unlikely, an example is given in figure 4.13, most likely caused by receiver tracking problems.

For PT4 all occultations with the water vapour pressure below -2 hPa at the lowest occultation point is plotted in figure 4.14. They are smoothly distributed and make up a fraction of 6% of all the PT4 occultations. This number is a factor 2-3 lower than what is found in other studies, but they also included other selection criteria. Furthermore the limit of -2 hPa might be narrowed down to -1 hPa, if the noise estimate is to be used strictly, which would increase the fraction to about 9%. Also this limit is taken at the bottom, which leaves room for the profile to be more negative at higher altitudes.

In figure 4.15 the Kolmogorov-Smirnov test is performed on the sample of out-

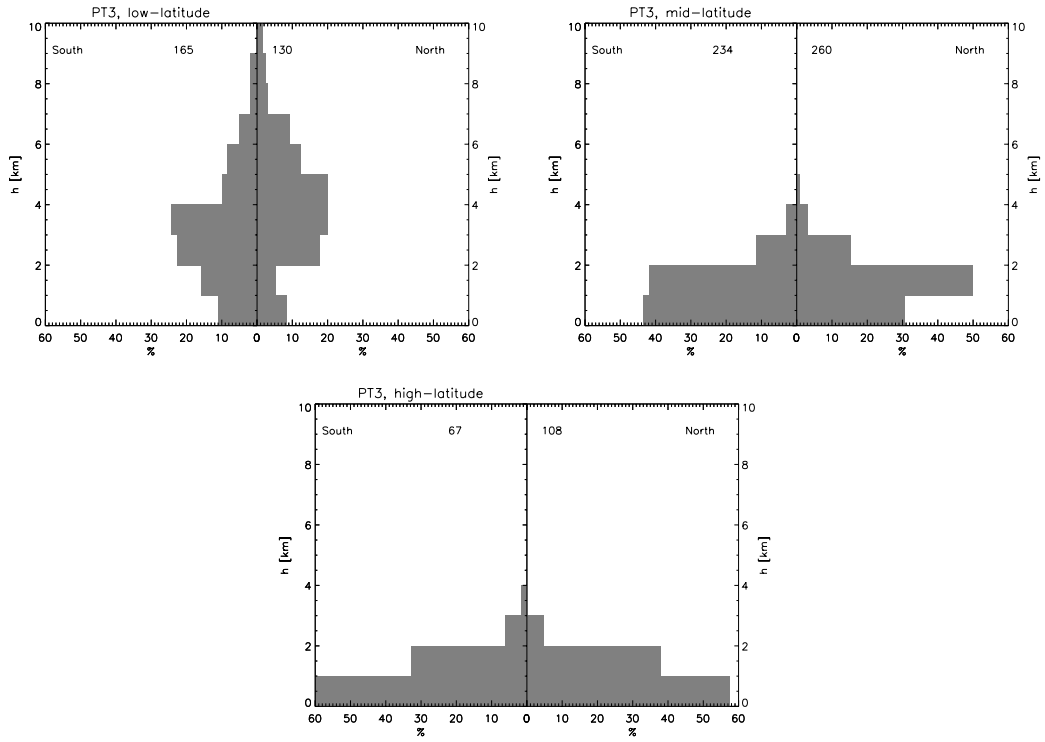

Figure 4.11: Distribution of lowest point in occultations for primetime 3. Notation like figure 4.8. A total of 964 profiles.

liers. The distributions are found to be non-uniform with an over-density at the Pacific and the southern hemisphere. In these regions the numerical weather models are known to be least reliable which could explain at least some of the large negative water vapour pressures.

These problems can often be traced back to the excess Doppler shift (dL/dt) which is often seen to flatten out or decrease at some point, either at the very end or at some time during the last 10 s. Errors in the orbits would map directly into the excess Doppler shift but no such errors or discontinuities of the time derivate is seen.

Explanations for the cases could be strong multi-path, but this would more likely be observed as very noisy phase observations and not smooth variations. An alternative explanation is the receiver misinterpreting the received signal, but detailed testing of this hypothesis requires insight into the receiver software.

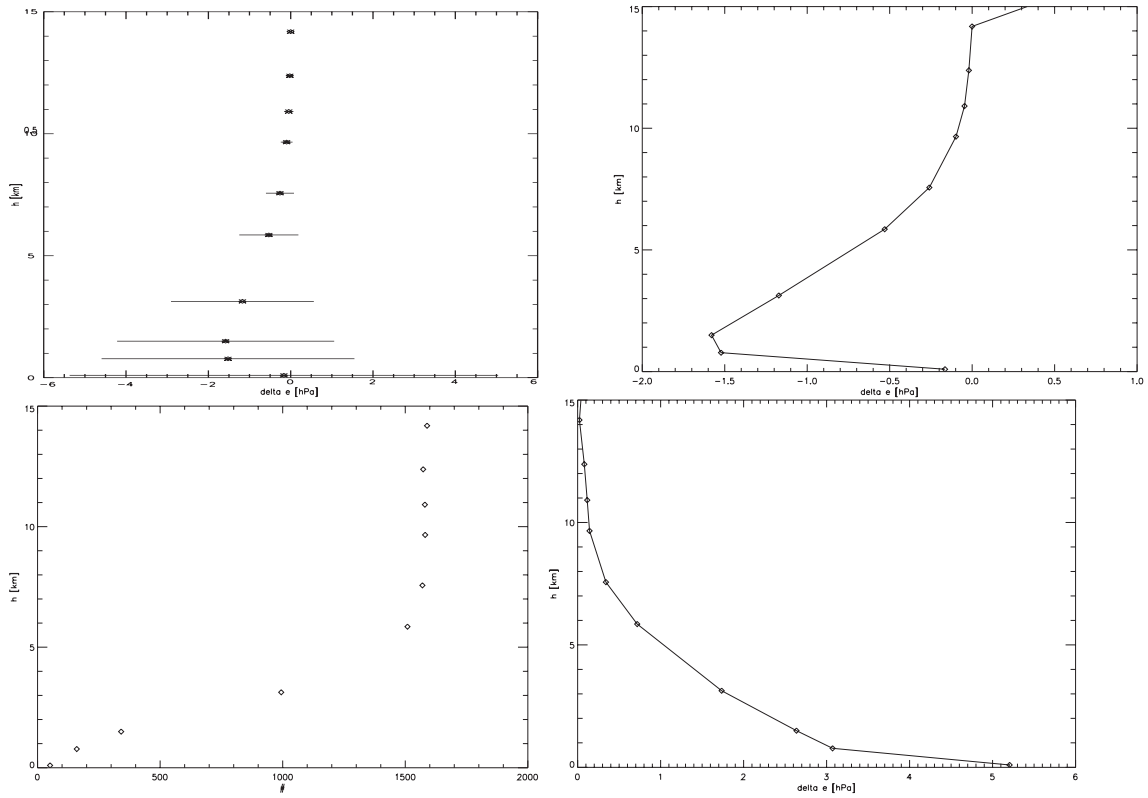

Figure 4.12: PT4 vs. ECMWF humidity statistics, all as function of height for a sample of up to 1500 profiles. Top left the standard deviation on the average difference, top right the average difference, bottom left the number of profiles and bottom right the standard deviation alone.

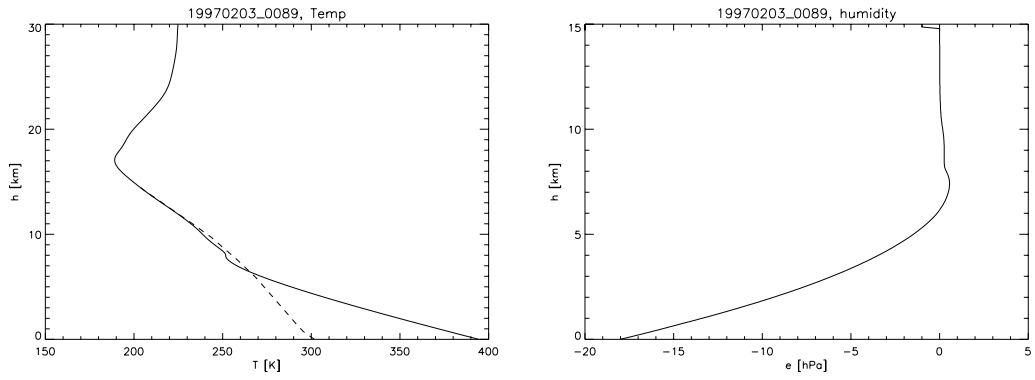

Figure 4.13: Example of a profile with large negative water vapour pressure, along with the corresponding temperature profile (solid line is occultation dry temperature and dashed line the ECMWF temperature). The profile is number 0089 on February 3rd 1997.

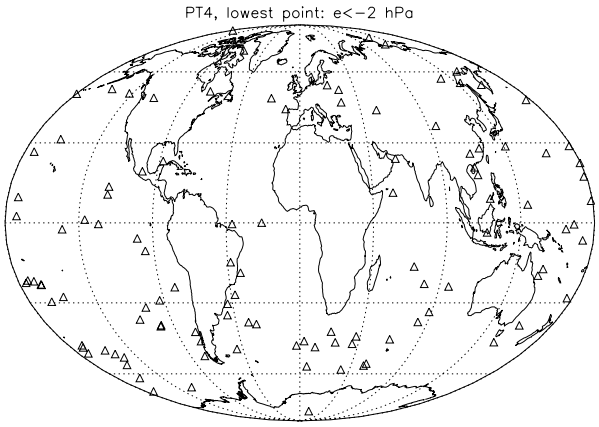

Figure 4.14: The global distribution of all profiles in PT4 which have water vapour pressure below −2 hPa at the lowest occultation point.

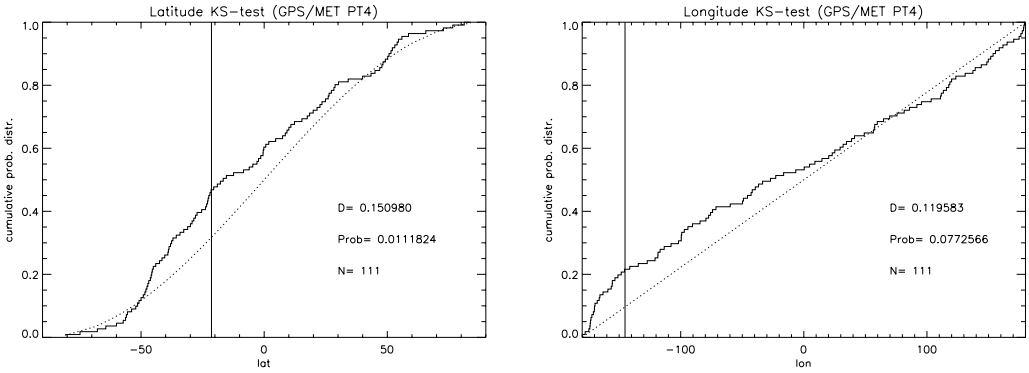

Figure 4.15: Kolmogorov-Smirnov test for PT4 outliers. Symbols are as in Figure 4.3.

4.2 CHAMP

CHAMP is a German geodetic satellite launched on July 15th 2000. It carries instruments for precise measurements of the geopotential field (accelerometers, laser reflector and GPS receivers) and instruments to perform both GPS occultation measurements and GPS Earth surface reflection measurements. It carries two BlackJack receivers and two occultation antennas, one rear viewing (for setting occultations) and one nadir viewing (for surface reflections). The satellite is operated from GeoForschungsZentrum Potsdam in Germany.

Much of the work done on CHAMP data is presented at the CHAMP 1st Science Meeting (CSM1) with a proceeding contribution found in Appendix B. This work will be discussed below and some results from additional data will also be examined. Further analysis is found in e.g. (Wickert et al., 2001)

4.2.1 Discussion of CSM1 contribution

A sample of 768 occultations from summer 2001 has been inverted to temperature and humidity profiles on basis of ECMWF temperature profiles. The temperature profiles from the occultation measurements are found to agree statistically with corresponding ECMWF profiles to within ≈ 1 K in the lower stratosphere. The disagreements found below the stratosphere is the result of tropospheric water vapour contributing significantly to the refractivity. At high altitudes the initialisation of the integrations give large discrepancies, but the effect is being damped exponentially. Hence the temperature at altitudes containing water vapour is unaffected by the initialisation problem. The water vapour has been derived through the direct (suboptimal) method with external information of temperature coming from ECMWF models. Since the water vapour content is highly latitude depending the statistical analysis has been performed in three bands separating the moist low latitude and dry high latitude by a mid-latitude band. Only the low latitude sample has an average difference exceeding 1 hPa in water vapour pressure.

Analysis of the penetration depth reveals that at the low latitudes only about 50% reach the surface, whereas about 80% reach the ground at the remaining globe. This result is good news, except for the fact that in many cases the lower occultation measurements are fly-wheeling data points which are not independent atmosphere measurements but rather depending on the receiver programming.

4.2.2 Distribution of measurements

CHAMP delivers on routine basis occultations and has done so since the beginning of 2001. For this work one month of occultations have been selected - from November 2001. It consists of 2332 profiles, which on average is 77 per day. This rather low number is the result of a few per day failing processing and changes in software resulting in periods with non-optimal recording of occultations.

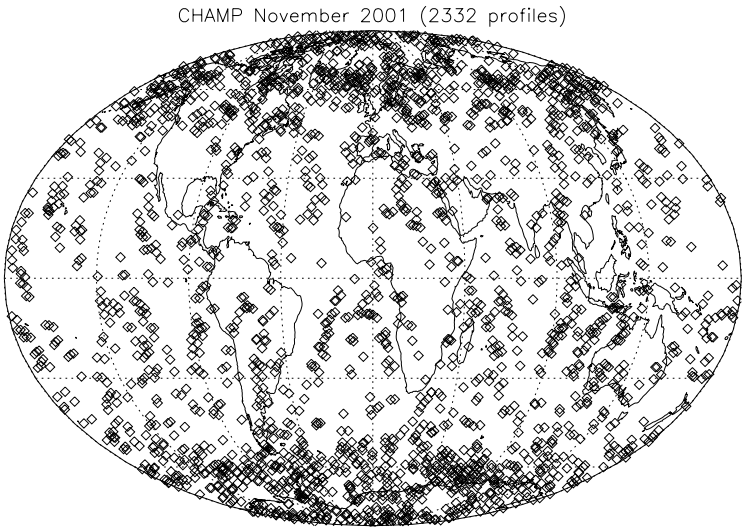

Figure 4.16: Distribution of occultations for CHAMP in November 2001.

4.2.3 Kolmogorov-Smirnov test

In the same way as the GPS/MET primetimes were examined for global smoothness, also occultations from CHAMP, November 2001 have been tested. The CHAMP orbit is nearly polar (inclination 87°) and with initial orbital height of 454 km with a steady decrease due to drag forces between the satellite and the ionosphere. Two parameters drive the significantly higher longitude *Prob* for CHAMP compared to that of GPS/MET: the orbit geometry and the dense network of ground stations. The latitude distribution shows even more pronounced variations than that of GPS/MET due to the polar orbit of CHAMP.

The curves are found in figure 4.17, and the fitting numbers in table 4.4. The distribution in latitude is found to have a zero probability of being of the modelled type. This can be explained by the satellite orbiting in an almost polar orbit which then crosses the poles much more frequently than a specific position on equator, and with the front looking antenna more polar occultations will happen than equatorial occultations. A zero model probability indicates that the occultations are far from optimal in the distribution if they are to be used in weather prediction.

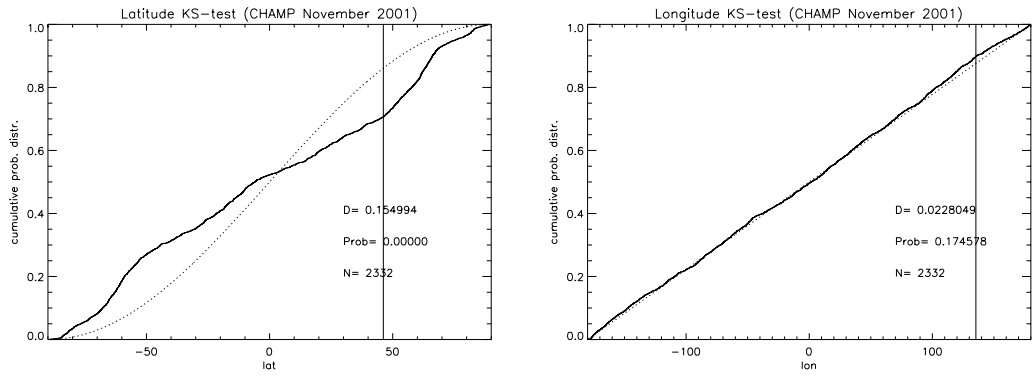

Figure 4.17: Kolmogorov-Smirnov test for CHAMP in November 2001. Symbols as in Figure 4.3.

	Latitude		Longitude		
	D	Prob	D	Prob	N
November 2001	0.155	0.000	0.023	0.175	2332

Table 4.4: The results of the KS-test performed on the November occultations from CHAMP.

CHAMP conclusion

CHAMP is delivering occultations on routine basis. The high precision orbital parameters which are necessary for the inversion are delivered fast as the satellite is mainly a geodetic mission. The orbit is very different from that of GPS/MET both in height and inclination. Usually such a low orbit height is not desired for occultation missions as the drag forces complicate the orbit determination, shorten the mission lifetime and complicates both ionospheric occultation inversion and ionosphere correction of neutral atmosphere profiling. The high inclination is a result of a down-link station at high latitude. Occultation profiles are from CHAMP delivered at changing rate depending on the software development of the BlackJack receiver, but the quality is on the same level as GPS/MET (Rocken et al., 1997) with close to zero temperature bias and a standard deviation at the order of 1 K in the lower stratosphere. This is remarkably as CHAMP is operating with AS on, where as GPS/MET has AS off in the primetimes.

4.3 Future aspects

The future looks bright for limb sounding in general, and GNSS limb sounding in particular as the hardware is relatively cheap and the data is stable over time. But still several aspects could be improved:

On the receiver side the question of implementing open loop and/or examine the implications of fly wheeling to probe the deep atmosphere has to be examined. Also the time for tracing rising occultations should be approaching, this alone would double the amount of occultations, but also require either open loop or more wide closed loop receivers. To further increase the amount of occultations the European Galileo GNSS system should be implemented in the receivers - this would increase the number of occultations by about a factor two as it is to consist of 30 satellites. To specifically increase the information on water vapour, microwave links around the 22 GHz feature could be developed and inversion routines of this type of measurements be established.

One major inversion issue is the 10 to 20 percent of occultations which fall outside the inversion processing. This problem might partly be a receiver issue, but could also originate in the early inversion or in atmospheric properties. Multi-path seems to be rather frequent in the measurements especially in the planetary boundary layer. This has to be either corrected for or a multi-path tolerant inversion has to be developed. For real-time use an automated inversion processing chain should be established. This is being prepared for the EUMETSAT GRAS Meteorology SAF with data from the future EPS/Metop satellites.

Regarding assimilation the implementation of a real time system, definition of error matrices (very important) and investigation of the data level to assimilate (humidity, temperature, refractivity, bending angle or even excess phases) are the main issues. Data probably should be assimilated 'early' (meaning with as little pre-processing as possible), preferably already at the phase-level to minimise the amount of assumptions. On the other hand an 'early' assimilation requires more computer time, but this seems to be a problem that decreases with time, unless the increase in computer power is used for increasing the model resolution with more grid points.

The received signals contain more information than used in the atmospheric profiling. As the atmospheric signatures in the signals were once considered noise on geodetic measurements, the signals from reflections on sea and ice surfaces are now considered noise on atmospheric measurements. These reflection signals might be extracted for deriving sea/ice surface altitudes and roughness for the benefit of ocean research, wind stress measurements and climate investigations (e.g. sea rise and ice melting).

Repeated measurements of the same atmospheric section would increase the knowledge of the speed of atmospheric processes. This could be done by equipping a two-satellite constellation like GRACE with occultation receivers virtually performing the same occultation with just a tiny shift in time and position. Furthermore the distance between the two receivers should be similar to the horizontal resolution (approximately 200 km).

All the aspects above are possible to assess with the present technology.

Chapter 5

Conclusions

A method of deriving water vapour in the troposphere has been established with GPS occultation experiments.

In this work only the direct iterative inversion method of refractivities has been applied, with external information being temperatures from the ECMWF dataset. Questions could be raised on the use of method and external data source, but the method has proven stable even though it is not statistical optimal. At present, data from ECMWF appears to be of very high quality on global scale, with highest errors on the southern hemisphere due to a severe lack of input data.

With the present accuracy of the values of the refractivity parameters a precision of about 3% can be established. Before the profiles can be derived several obstacles have to be overcome, regarding tracking and interpretation of the received signal. Under quiet atmospheric conditions signal tracking in the stratosphere and high troposphere seems successful, but problems might arise in and close to the boundary layer causing a significant fraction of occultations to end here and not at the surface.

With data from both GPS/MET and CHAMP statistical comparisons to global weather fields have been performed, revealing a precision of the derived water vapour profiles below 2 hPa at altitudes above 2 km, with an average difference less than 1.5 hPa. The temperature is determined outside the water containing troposphere to within less than a kelvin in average difference and less than two kelvin standard deviation. In the high stratosphere the occultation temperature departs from the weather model temperature, probably due to initialisation difficulties of the integrations performed in the occultation inversion. Fortunately for water vapour studies this error dampens fast resulting in a reliable temperature below ≈ 30 km, and the most reliable temperatures near tropopause altitudes.

Unfortunately a large fraction (in this work about 10%, in other works even more) of the occultations invert to non-physical atmospheric parameters. The explanation for these results has not been found, but is expected to be either the result of tracking errors in the receivers or very special atmospheric properties. As the phases and Doppler shift of the bad occultations are not showing signs of strong multi-path or other fast phenomena, the receiver explanation seems most probable.

Examination of one refractivity field generated on basis of ECMWF temperature, pressure and humidity fields reveals much structure on all scales. Critical refraction is found over a significant fraction of the globe (2%), but many places in very

low and/or in very thin layers. On the west coast of North America and especially Africa and India huge regions are experiencing critical refraction at heights even above 1 km and in layers extending more than 200 m in thickness.

Acknowledgement

I would like to thank my colleagues, family and friends for support, assistance and encouragement during the project years. Even though not everybody can be mentioned in person, some have made special contributions, first of all my wife Lisbeth for indulgence, assistance and general scientific discussions many evenings.

I have had many conversations with my good friend and colleague Georg on many occultation topics - this has been valuable and rewarding. Also the rest of the occultation group on DMI have contributed to my work through many discussions.

During my visit at GeoForschungsZentrum Potsdam I enjoyed the hospitality of the occultation group, and in particular Christian Marquardt and Jens Wickert - they were very patient with me even though I never started speaking German.

Much of the occultation retrieval software is based on code by Stig Syndergaard. I appreciate the good and thorough work he has done, and the advices on issues regarding the code and inversion given by him.

And finally to my two supervisors, Aksel Walløe Hansen at the Copenhagen University and Per Høeg at the Danish Meteorological Institute for support and supervision, and to the national science foundation and DMI for funding this work.

Abbreviations

ACE+	Atmosphere and Climate Explorer
AM	Atmospheric Multi-path
CHAMP	CHAllenging Minisatellite Payload
CSM1	First CHAMP Science Meeting.
DMI	Danmarks Meteorologiske Institut
ECMWF	European Centre for Medium-range Weather Forecast
EGOPS	End-to-end GNSS Occultation Profile Simulator
EGM96	Earth Gravity Model 1996, geoide
EPS	EUMETSAT Polar System
GRACE	Gravity Recovery And Climate Experiment
GRAS	GNSS Receiver for Atmospheric Sounding
GLONASS	GLObal NAvigation Satellite System
GNSS	Global Navigation Satellite System
GPS	Global Positioning System
GPS/MET	GPS Meteorological (experiment)
IPCC	International Panel for Climate Change
IPW	Integrated Precipitable Water.
KS	Kolmogorov-Smirnov test
LEO	Low Earth Orbit(er)
NWP	Numerical Weather Prediction
PBL	Planetary Boundary Layer
PT	Primetime
SA	Selective Availability
SAF	Satellite Application Facility
URSI	Union Radio-Scientifique Internationale
UTC	Coordinates Universal Time
WGS84	World Geodetic System 1984

Nomenclature

a	Impact parameter, indexed 1, 2 or c for L_1, L_2 and ionosphere corrected.
α	bending angle, indexed 1, 2 or c for L_1, L_2 and ionosphere corrected.
$\vec{v}_{\mathrm{LEO}}$	velocity vector of the LEO.
$\vec{r}_{\mathrm{LEO}}$	position vector of the LEO.
$\vec{v}_{\mathrm{GPS}}$	velocity vector of the GPS.
$\vec{r}_{\mathrm{GPS}}$	position vector of the GPS.
N	Refractivity, $N \equiv 10^6(n-1)$
n	Index of refraction (often only real part n').
c	Speed of light in vacuum ($2.99792458 \cdot 10^8$ $mathrmm\ s$)
λ	Wavelength
v	Velocity (can be a vector).
θ	Angles.
r	Radius (of tangent point) - or mixing ratio.
z	Distance from tangent point to receiver.
k_{1-3}	3 parameters for relating P_d, T, e and N
T	Temperature [K]
P	Pressure [hPa]
p	Partial pressure of dry air [hPa]
e	Partial pressure of water vapour [hPa]
q	Relative humidity [%].
N_e	Electron density [electrons/m^3]
f	Frequency [Hz].
f_1	Frequency of the L_1 signal - 1.57542 GHz
f_2	Frequency of the L_2 signal - 1.2276 GHz
f_5	Frequency of the L_5 signal - 1.17645 GHz.
L	Phase delay [m] (indexed for L1, L2 or ionosphere corrected) - or evaporation energy.
τ	Time-scale
ρ	Density [kg m^{-3}]
g	Acceleration of gravity - ≈ 9.8 m s^{-2}
H_p	Pressure scale height.
$\mathcal{M}$	Water reservoir.
$\mathcal{F}$	Water flux between reservoirs.
L_0 and l_0	Outer and inner scale of turbulence.
D	Parameter in KS-test.
Q	Incomplete Gamma function.
ν	Degrees of freedom.

Bibliography

Ahmad, B. and Tyler, G. (1999). Systematic errors in atmospheric profiles obtained from Abelian inversion of radio occultation data: Effects of large-scale horizontal gradients. *JGR*, 104(D4):3971–3992.

Belloul, M. B. and Hauchecorne, A. (1997). Effect of periodic horizontal gradients on the retrieval of atmospheric profiles from occultation measurements. *Radio Science*, 32(2):469–478.

Bevis, M., Businger, S., and Chiswell, S. (1994). GPS Meteorology: Mapping Zenith Wet Delay onto Precipitable Water. *Journal of Applied Meteorology*, 33:379–386.

Bevis, M., Businger, S., Herring, T. A., Rocken, C., Anthes, R. A., and Ware, R. H. (1992). GPS Meteorology: Remote Sensing of Atmospheric Water Vapor Using the Global Positioning System. *JGR*, 97(D14):15,787–15,801.

Beyerle, G. and Hocke, K. (2001). Observation and simulation of direct and reflected GPS signals in radio occultation experiments. *GRL*, 28(9):1895–1898.

Black, H. D. and Eisner, A. (1984). Correcting Satelite Doppler Data for Tropospheric Effects. *JGR*, 89(D2):2616–2626.

Born, M. and Wolf, E. (1980). *Principles of Optics*. Pergamon Press Ltd., 6.th edition.

Christensen-Dalsgaard, J. (1993). *Lecture notes on Stellar Structure and Evolution*. Institut for Fysik og Astronimi, Aarhus Universitet, 3. edition.

Cupillard, F. (1999). Radio Occultation and Multipath. Technical report, ACRI. available at http://www.acri.fr/gps/gpsro/rapport.pdf.

Dierendonck, A. V. and Hegarty, C. (2000). The New L5 Civil GPS Signal. *GPS World*.

Elliot, J. (1979). Stellar occultation studies of the Solar Syetem. *Ann. Rev. Astron. Astrophys.*, 17:445–475.

Eshleman, V. R., Tyler, G. L., Anderson, J. D., Fjeldbo, G., Levy, G. S., Wood, G. E., and Croft, T. A. (1977). Radio Science Investigations with Voyager. *Space Science Reviews*, 21:207–232.

Eyre, J. R. (1994). Assimilation of radio occultation measurements into numerical weather prediction systems. Technical Report 199, ECMWF, Reading, UK.

Fälthammar, C.-G. (1992). *Space Physics*. Department of Plasma Physics, Royal Institute of Technology, Sweden, 1.st edition.

Fjeldbo, G. and Eshleman, V. (1969). Atmosphere of Venus as studied with the Mariner 5 dual radio-frequency occultation experiment. *Radio Science*, 4(10):879–898.

Fjeldbo, G., Kliore, A. J., and Eshleman, V. R. (1971). The Neutral Atmosphere of Venus as Studied with the Mariner V Radio Occultation Experiment. *The Astronomical Journal*, 76(2):123–140.

Foelsche, U. (1999). *Tropospheric water vapor imaging by combination of ground-based and spaceborne GNSS sounding data*. PhD thesis, IMG, Univertitat Graz.

Forster, P. and Shine, K. P. (2002). Assessing the climate impact of trends in stratospheric water vapor. *GRL*, 29(6):10–1–10–4.

Fox-Rabinovitz, M. S. and Lindzen, R. S. (1993). Numerical Experiments on the Consistent Horizontal and Vertical Resolution for Atmospheric Models and Observing Systems. *Mon. Weather Rew.*, 121:264–271.

Garrison, J., Komjathy, A., Zavorotny, V., and Katzberg, S. (2002). Wind Speed Measurement Using Forward Scattered GPS Signals. *IEEE Trans.*, 40(1):50–65.

Gorbunov, M., Gurvich, A., and Kornblueh, L. (2000). Comparative analysis of radioholographic methods of processing radio occultation data. *Radio Science*, 35(4):1025–1034.

Gorbunov, M. E. (2001). Radioholographic methods for processing radio occultation data in multipath regions. Scientific Report 01-02, Danish Meteorological Inst.

Gorbunov, M. E., Gurvich, A. S., and Bengtsson, L. (1996a). Advanced Algorithms of inversion of GPS/MET satellite data and their application to reconstruction of temperature and humidity. Technical Report 211, Max-Planck-Institut für Meteorologie.

Gorbunov, M. E. and Sokolovskiy, S. V. (1993). Remote sensing of refractivity from space for global observations of atmospheric parameters. Technical Report 119, Max-Planck-Institut für Meteorologie.

Gorbunov, M. E., Sokolovskiy, S. V., and Bengtsson, L. (1996b). Space Refractive Tomography of the Atmosphere: Modeling of direct and inverse problems. Technical Report 210, Max-Planck-Institut für Meteorologie.

Healy, S. (2001). Radio Occultation bending angle and impact parameter errors caused by horizontal refractive index gradients in the troposphere: A simulation study. *JGR*, 106(D11):11,875–11,889.

Hinson, D., Simpson, R., Twicken, J., Tyler, G., and Flasar, F. (1999). Initial results from radio occultation measurements with Mars Global Surveyor. *JGR*, 104(E11):26,997–27,012.

Hinson, D., Tyler, G., Hollingsworth, J., and Wilson, R. (2001). Radio occultation measurements of forced atmospheric waves on Mars. *JGR*, 106(E1):1463–1480.

Hinson, D. P. and Tyler, G. L. (1982). Spatial irregularities in Jupiter's upper ionosphere observed by Voyager radio occultations. *JGR*.

Hocke, K. (1997). Inversion of GPS meteorology data. *Ann. Geophysicae*, 15:443–450.

Hocke, K., Pavelyev, A. G., Yakovlev, O., Barthes, L., and Jakowski, N. (1999). Radio Occultation Data Analysis by the Radioholographic Method. *JASTP*. submitted.

Høeg, P., Hauchecorne, A., Kirchengast, G., Syndergaard, S., Belloul, B., Leitinger, R., and Rothleitner, W. (1995). Derivation of Atmospheric Properties using a Radio Occultation Technique. Technical Report 95-4, DMI. ISBN: 87-7478-331-9.

Høeg, P. and Kirchengast, G. (2002). ACE+, Atmosphere and Climate Explorer. ESA Proposal.

Igarashi, K., Pavelyev, A., Hocke, K., Pavelyev, D., and Wickert, J. (2001). Observation of wave structures in the upper atmosphere by means of radio holographic analysis of the radio occultation data. *Adv. Space Res.*, 27(6-7):1321–1326.

Jarlemark, P. O. J. (1997). *Analysis of Temporal and Spatial Variations in Atmospheric Water Vapor Using Microwave Radiometry*. PhD thesis, School of Electrical and Computer Engineering, Chalmers University.

Kliore, A. J., Cain, D. L., Fjeldbo, G., L.Seidel, B., and Sykes, M. J. (1972). The Atmosphere of Mars from Mariner 9 Radio Occultation Measurements. *Icarus*, 17:484–516.

Kuo, Y.-H., Zou, X., Chen, S. J., Huang, W., Guo, Y.-R., Anthes, R. A., Exner, M., Hunt, D., Rocken, C., and Sokolovskiy, S. (1998). A GPS/MET Sounding through an Intense Upper-level Front. *BAMS*, 79(4):617–626.

Kursinski, E., Hajj, G., Leroy, S., and Harman, B. (2000). The GPS Radio Occultation Technique. *TAO*, 11(1):53–114.

Kursinski, E. R. and Hajj, G. A. (2001). A comparison of water vapor derived from GPS occultations and global weather analyses. *JGR*, 106(D1):1113–1138.

Kursinski, E. R., Hajj, G. A., Bertiger, W. I., Leroy, S. S., Meehan, T. K., Romans, L. J., Schofield, J. T., McCleese, D. J., Melbourne, W. G., Thornton, C. L., Yunck, T. P., Eyre, J. R., and Nagatani, R. N. (1996). Initial Results of Radio Occultation Observations of Earth's Atmosphere Using the Global Positioning System. *Science*, 271:1107–1110.

Leroy, S. S. (1997). Measurement of geopotential heights by GPS radio occultation. *JGR*, 102(D6):6971–6986.

Liebe, H. (1989). MPM - an Atmospheric Millimeter-wave Propagation Model. *International Journal of Infrared and Millimeter waves*, 10(6):631–650.

Lindal, G. F. (1992). The Atmosphere of Neptune: An Analysis of Radio Occultation Data Acquired with Voyager 2. *The Astronomical Journal*, 103(3):967–982.

Lindal, G. F., Lyons, J. R., Sweetnam, D. N., Eshleman, V. R., Hinson, D. P., and Tyler, G. L. (1987). The atmosphere of Uranus: Results of radio occultation measurements with Voyager 2. *JGR*, 92:14987–15001.

Lindal, G. F., Sweetnam, D. N., and Eshleman, V. R. (1985). The atmosphere of Saturn: An analysis of the Voyager radio occultation measurements. *The Astronomical Journal*, 90(6):1136–1146.

Lipa, B. and Tyler, G. L. (1979). Statistical and Computational Uncertainties in the Atmospheric Profiles from Radio Occultation: Mariner 10 at Venus. *Icarus*, 39:192–208.

Lowe, S. T., LaBrecque, J. L., Zuffada, C., Romans, L. J., Young, L. E., and Hajj, G. A. (2002). First spaceborne observation of an Earth-reflected GPS signal. *Radio Science*, 37(1):7–1 – 7–28.

Luntama, J.-P. (1997). *Atmospheric Profiling with Radio Occultation*. PhD thesis, Helsinki University of Technology, Department of Electrical and Communications Engineering.

Marouf, E. A., Tyler, G. L., and Rosen, P. A. (1986). Profiling Saturn's Rings by Radio Occultation. *Icarus*, 68:120–166.

Marquardt, C., Labitzke, K., Reigber, C., Schmidt, T., and Wickert, J. (2001). An Assessment of the Quality of GPS/MET Radio Limb Soundings During February 1997. *Phys. Chem. Earth (A)*, 26(3):125–130.

Mockler, S. B. (1995). Water Vapor in the Climate System. http://www.agu.org/sci_soc/mockler.html, AGU, 2000 Florida Ave., Washington, DC 20009. ISBN: 0-87590-865-9.

Mortensen, M. D. and Høeg, P. (1998). Inversion of GPS occultation measurements using Fresnel diffraction theory. *Geophys. Res. Let.*, 25(13):2441–2444.

Palmer, P., Barnett, J., Eyre, J., and Healy, S. (2000). A nonlinear optimal estimation inverse method for radio occultation measurements of temperature, humidity and surface pressure. *JGR*, 105(D13):17,513–17,526.

Parkinson, B. W. and Spilker, J. S. J., editors (1996). *Global Positioning System: Theory and Applications*, volume I and II of *Progress in Astronautics and Aeronautics*. American Institute of Aeronautics and Astronautics. ISBN: 1-56347-106-X and i-56347-107-8.

Peixoto, J. P. and Oort, A. H. (1992). *Physics of Climate*. Springer.

Press, W., Teukolsky, S., Vetterling, W., and Flannery, B. (1992). *Numerical Recipies in FORTRAN*. Cambridge University Press, 2nd edition.

Rasmussen, F. B. (1991). Noter til varmelære.

Rius, A., Ruffini, G., and Cucurull, L. (1997). Improving the vertical resolution of ionospheric tomography with GPS occultations. *GRL*, 24(18):2291–2294.

Rocken, C., Anthes, R., Exner, M., Hunt, D., Sokolovskiy, S., Ware, R., Gorbunov, M., Schreiner, W., Feng, D., Herman, B., Kuo, Y.-H., and Zou, X. (1997). Analysis and validation of GPS/MET data in the neutral atmosphere. *JGR*, 102(D25):29,849–29,866.

Ruffini, G., Cardellach, E., Rius, A., and Aparicio, J. M. (1999). Remote Sensing of the Ocean by Bistatic Radar Observation: a Review. Technical Report ESD-ion019-99, IEEC.

Salby, M. L. (1996). *Fundamentals of Atmospheric physics*. Academic Press.

Shindell, D. T. (2001). Climate and ozone response to increased stratospheric water vapor. *GRL*, 28(8):1551–1554.

Sokolovskiy, S. (2000). Inversion of radio occultation amplitude data. *Radio Science*, 35(1):97–105.

Sokolovskiy, S. (2001). Modelling and inverting radio occultation signals in the moist troposphere. *Radio Science*, 36(3):441–458.

Solheim, F., J.Vivekanandan, Ware, R., and Rocken, C. (1999). Propagation delays induced in GPS signals by dry air, water vapor, hydrometeors, and other particulates. *JGR*, 104(D8):9663–9670.

Steiner, A. K. (1998). *High Resolution Sounding of Key Climate Variables Using the Radio Occultation Technique*. PhD thesis, Institute für Meteorologie und Geophysik, Universiät Graz.

Strohbehn, J. W. (1968 and 1969). Line-of-sight Wave propagation Through the Turbulent Atmosphere. *Proceedings of the IEEE*.

Syndergaard, S. (1998). Modeling the impact of the Earth's oblateness on the retrieval of temperature and pressure profiles from limb sounding. *Journal of Atm. and Solar-Terrestrial Phys.*, 60(2):171–180.

Syndergaard, S. (1999). *Retrieval Analysis and Methologies in Atmospheric Limb Sounding Using the GNSS Radio Occultation Technique*. PhD thesis, Copenhagen University, Physics. Printed as DMI Scientific Report 99-6, ISBN: 87-7478-394-7.

Syndergaard, S. (2000). On the ionosphere calibration in GPS radio occultation measurements. *Radio Science*, 35(3):865–883.

Tatarski, V. I. (1961). *Wave propagation in a Turbulent Medium*. McGraw-Hill.

Thayer, G. (1974). An improved equation for the radio refractive index of air. *Radio Science*, 9(10):803–807.

Tyler, G. L., Sweetnam, D. N., Anderson, J. D., Borutzki, S. E., Campbell, J. K., Eshleman, V. R., Gresh, D. L., Gurrola, E. M., Hinson, D. P., Kawashima, N., Kursinski, E. R., Levy, G. S., Lindal, G. F., Lyons, J. R., Marouf, E. A., Rosen, P. A., Simpson, R. A., and Wood, G. E. (1989). Voyager Radio Science Observations of Neptune and Triton. *Science*, 256:1466–1473.

Vorob'ev, V. V. and Krasil'nikova, T. G. (1994). Estimation of the Accuracy of the Atmospheric Refractive Index Recovery From Doppler Shift Measurements at Frequencies Used in the NAVSTAR System. *Physics of the Atm. and Ocean*, 29(5):602–609. English translation from Russian Ed. Sept.-Oct. 1993.

Webb, S., editor (1988). *The physics of medical imaging*. Institute of Physics Publishing, Institute of Physics Publishing, Techno House, Redcliff Way, Bristol.

Wesely, M. (1976). The Combined Effect of Temperature and Humidity Fluctuations on Refractive Index. *J. App. Met.*, 15:43–49.

Wickert, J., Reigber, C., Beyerle, G., König, R., Marquardt, C., Schmidt, T., Grunwald, L., Galas, R., Meehan, T. K., Melbourne, W. G., and Hocke, K. (2001). Atmosphere sounding by GPS radio occultation: First results from CHAMP. *GRL*, 28(17):3263–3266.

Wyngaard, J., Seaman, N., Kimmel, S., Otte, M., Di, X., and Gilbert, K. (2001). Concepts, observations, and simulation of refractive index turbulence in the lower atmosphere. *Radio Science*, 36(4):643–669.

Wyngaard, J. C. and LeMone, M. (1980). Behavior of the Refractive Index Structure Parameter in the Entraining Convective Boundary Layer. *Journal of the Atmospheric Sciences*, 37(7):1573–1585.

Yan, H., Huang, D., and Huang, C. (1999). Sequential atmospheric profiles near a fixed location derived from GPS-LEO occultation measurements. *Geophys. Res. Let.*, 26(4):451–453.

Yunck, T., Liu, C.-H., and Ware, R. (2000). A History of GPS Sounding. *TAO*, 11(1):1–20.

Zou, X., Vandenberghe, F., Wang, B., Gorbunov, M., Kuo, Y.-H., Sokolovskiy, S., Chang, J., Sela, J., and Anthes, R. (1999). A ray-tracing operatur and its adjoint for the use of GPS/MET refraction angle measurements. *JGR*, 104(D18):22,301–22,318.

Appendix A

A.1 Different measures of gas

As this thesis is mainly dealing with water vapour measured as a partial pressure or absolute humidity and some prefer relative humidity, dew-point temperature or some other unit, this section contains considerations on the various transformations (see also (Foelsche, 1999, sect. 1.1.1)). Also some remarks on the physics behind each measure is given.

A.1.1 Water Vapour pressure

e is the partial pressure of the water vapour. In case it is 0 hPa the air is dry. The water vapour partial pressure is independent of the other pressure contributors of the atmosphere according to Dalton's law* which states that the total pressure in a gas is the sum of all partial pressures by the individual constituents:

$$p = \Sigma_i p_i$$

The saturated partial pressure of water vapour is described by the Clausius-Clapeyron equation†.

A.1.2 Dew-point temperature

T_c is the temperature at which condensation occurs for air cooled at constant pressure and water vapour content. From this the water vapour pressure can be derived by inserting T_c into the equation 2.2 for e (for equilibrium with respect to liquid water)

A.1.3 Saturated vapour pressure

e_s is the water vapour pressure at which a equilibrium with an other phase of water is established (for a given temperature). Most common is the liquid water equilibrium, for which the equation is given in equation 2.2). That saturated water vapour pressure has been reached does not imply that no evaporation takes place from the solid or liquid phase, merely that there is a equilibrium between the amount of water being evaporated and that being condensed.

A.1.4 Specific (or absolute) humidity

q is the ratio of the mass of water vapour to the total air mass in in an air parcel. It is expressed in kg kg^{-1} or g kg^{-1}. This measure is often used as it is maintained in an air

*John Dalton, Sept. 6th 1766 - July 27th 1844, English chemist. Also the first to make a scientific description of colour blindness.

†Rudolf Julius Emmanuel Clausius, January 2nd 1822 - August 24th 1888. Polish/German physicist.
Benoist Paul Emile Clapeyron, February 26th 1799 - January 28th 1864. French ingeneer.

parcel if no phase transission in experienced.

A.1.5 Relative humidity

r is the ratio of measured vapour pressure to the saturated vapour pressure (at the same temperature). It is expressed as a percentage:

$$r = \frac{e}{e_s} 100\%$$

At 100% water vapour is at saturated pressure. In general the value is close to 80% in the atmosphere close to the ground.

A.1.6 Integrated water vapour

Integrated water vapour (or integrated precipitable water) is a column measurement of the water present in the atmosphere. Usually it is calculated towards zenith from a given position. This measurement is derived from ground based GPS measurements. $IPW = \int_{h_0}^{h_1} \rho_v dh$ with ρ_v being the water vapour density, h_0 the lower limit (often the ground level) and h_1 the upper limit (often at infinity), making the expression into:

$$IPW = \int_0^\infty \rho_v dh$$

With ground based measurements the IPW is measured as a signal delay added to the hydrostatic dry delay, and this delay has to be converted into IPW (Bevis et al., 1992).

A.2 US Standard Atmosphere

A convenient transformation between geometric heights and pressure levels can be performed through the US Standard Atmosphere (e.g. at http://nssdc.gsfc.nasa.gov/space/model/atmos/us_ which behaves as illustrated in figure A.1. The model is an average one dimensional atmosphere profile at 45° latitude. The model contains no information on water vapour

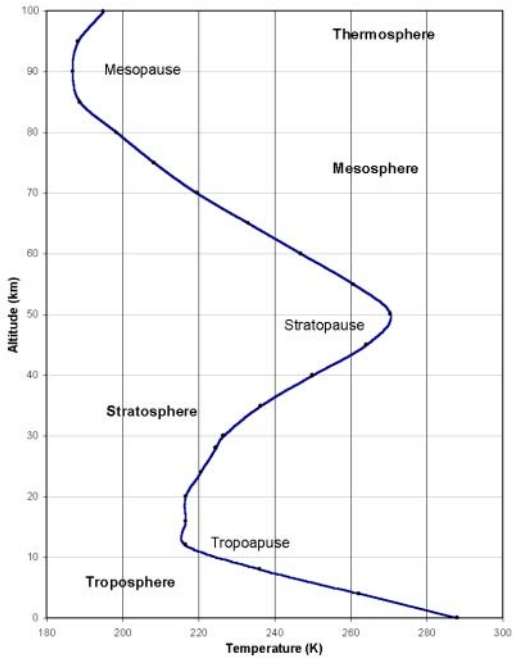

Figure A.1: The US Standard Atmosphere 1976. The points are the defined levels, and the line is interpolated. Added are the names of the atmospheric layers.

Appendix B

Proceedings contribution for CSM1

This appendix contains the conference contribution for the 1st CHAMP Science Meeting (CSM1), held January 21th to January 25th 2002 at GeoForschungsZentrum Potsdam, Germany. The paper had two anonymous internal referees.

Comparison of DMI Retrieval of CHAMP Occultation Data with ECMWF

Jakob Grove-Rasmussen

Danish Meteorological Institute, Lyngbyvej 100, DK-2100 Copenhagen, Denmark
jgr@dmi.dk

Summary. At DMI a processing chain for GPS radio occultation measurements has been made. It has been used on both GPS/MET and Ørsted data for retrieving both temperature in the stratosphere and troposphere as well as water vapour in the troposphere. For nine days of CHAMP data the Ørsted data processing chain for GPS radio occultation retrieval has been applied. The resulting profiles have been compared to corresponding ECMWF profiles of water vapour and temperature, resulting in a statistical description of the general agreement between the two datasets.

Key words: GPS, occultation, validation, humidity

List of Abbreviations and Symbols

- CHAMP CHAllenging Microsatellite Payload
- DMI Danish Meteorological Institute
- ECMWF European Centre for Mediumrange Weather Forecast
- GPS Global Positioning System
- LEO Low Earth Orbit
- SNR Signal-to-noise ratio
- N Refractivity ($N = 10^6(n-1)$)
- n Index of refraction
- P Dry pressure (hPa)
- e Water vapour partial pressure (hPa)
- T Temperature (K)

1 Radio occultation methodology

Profiles of the atmospheric parameters pressure, temperature and humidity can be derived from measurements of changes in the signals from GPS satellites setting behind the limb of the Earth, as observed from a receiver on-board a LEO satellite [4]. The observed parameter is the complex microwave signal, which contains information on the changes with height of the refractive index of the atmosphere. Knowing the geometry of the occultation, i.e. position and velocity of both satellites, the bending angle of each ray can be derived assuming a spherically symmetric atmosphere. This bending angle profile can, through the Abel transform, be inverted to a profile of

the refractive index n representing the atmosphere at the position of the ray tangentpoint.

The refractivity $N = 10^6(n-1)$ of the atmosphere contains contributions from 3 sources: ionosphere, neutral dry atmosphere and water vapour. Where the first contribution can be isolated, and to a large extend be removed using two frequencies due to its dispersive nature, the two other contributions form an ambiguity problem. They contribute to the refractivity as [7]:

$$N = k_1 \frac{P}{T} + k_2 \frac{e}{T} + k_3 \frac{e}{T^2}$$

with P being the dry pressure, e the water vapour partial pressure, T the temperature and $k_1 = 77.60 \pm 0.05$ K hPa^{-1}, $k_2 = 70.4 \pm 2.2$ K hPa^{-1} and $k_3 = (3.739 \pm 0.012) \cdot 10^5$ K^2 hPa^{-1} [1]. The k_2-term is very small and often neglected or merged into k_3.

Using this expression together with the ideal gas law and the hydrostatic equation the temperature profile can be calculated assuming a dry atmosphere ($e = 0$). The amount of water vapour can subsequently be extracted from the data by use of external information, e.g. temperature and/or humidity. Two methods are commonly in use for this: the iterative method which does not take into account the errors, and the 1d-var method which extracts information in a statistical optimal way [5].

2 Temperature profile statistics

All occultations available from CHAMP [8] in the period May 27th to June 2nd and August 26th and 27th have been inverted through the DMI inversion routines from excess phases and orbits, to temperature and humidity profiles [3]. The humidity profiles reveal that a fraction of the occultations contains information which transforms into huge negative water vapour pressure using the iterative inversion method. This result is unphysical and represents an interpretation challenge.

A subsample of 768 profiles (see distribution in fig. 1) has been selected for this study and comparison temperature profiles are extracted from ECMWF, based on the analysis output closest in time, resulting in a maximum time difference of 1.5 hour, and interpolated to the occultation position. The geometric interpolation is linear between the closest four grid points. The model resolution is 1 degree in both latitude and longitude and 21 pressure levels up to 1 hPa (corresponding to approximately 50 km), distributed with 11 levels in the lower decade (1000 to 100 hPa) and 5 in each up the two upper decades. The difference is made as $\Delta T = T_{occ} - T_{ECMWF}$ [6], see fig. 2.

Between 9 and 34 km altitude the average temperature difference is close to or below 1 K, and between 9 and 18 km the standard deviation is below 2.5 K Above 34 km the reason for the large error and standard deviation is

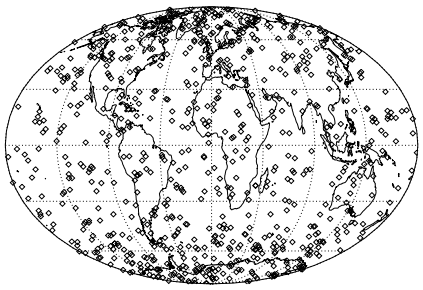

Fig. 1. Global distribution of the selected 768 CHAMP GPS occultation profiles.

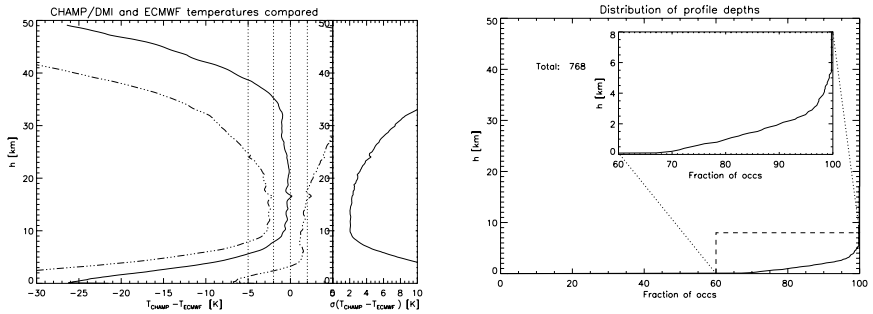

Fig. 2. Left: Mean difference between occultation derived temperature and ECMWF temperature (solid line in left part), along with the standard deviation (plotted both individual in the right part and as dotted-dashed lines relative to the mean difference in the left part). Right: Number of available profiles as function of height.

expected to arise from the initialisation of the integration. The problem is expected to be solved by an improved climatological constrain of the upper boundary. Below 9 km the large mean error difference and standard deviation arise from the presence of water vapour, which is assumed non-present in the inversion. At around 17 km altitude (above the tropopause) a small irregularity of about 1 K is noticed. An almost similar feature is found at the same altitude in [8] in the low latitude region, but no general conclusion can be drawn as the two curves are containing different information (fig. 2 contains a global average).

In the right panel of fig. 2 the penetration depth of the sample of occultations is plotted. A huge fraction of about 70 % reach close to the ground, and all occultations end below 6 km. This result is most promising for the capability of the CHAMP BlackJack receiver.

3 Water vapour statistics

The same set of occultation profiles has been inverted to water vapour profiles through the iterative method [2] at altitudes below 15 km. This method does not take into account the total error budget but gives a reliable calculation of water vapour pressure. The profiles have been compared to ECMWF humidity profiles (available up to 10 hPa) and averaged in 3 latitude intervals (high-, mid- and low-latitude). This has been done to separate the effect of huge changes in atmospheric structure with latitude, having the warm humid atmosphere at the equator the cold atmosphere at the poles.

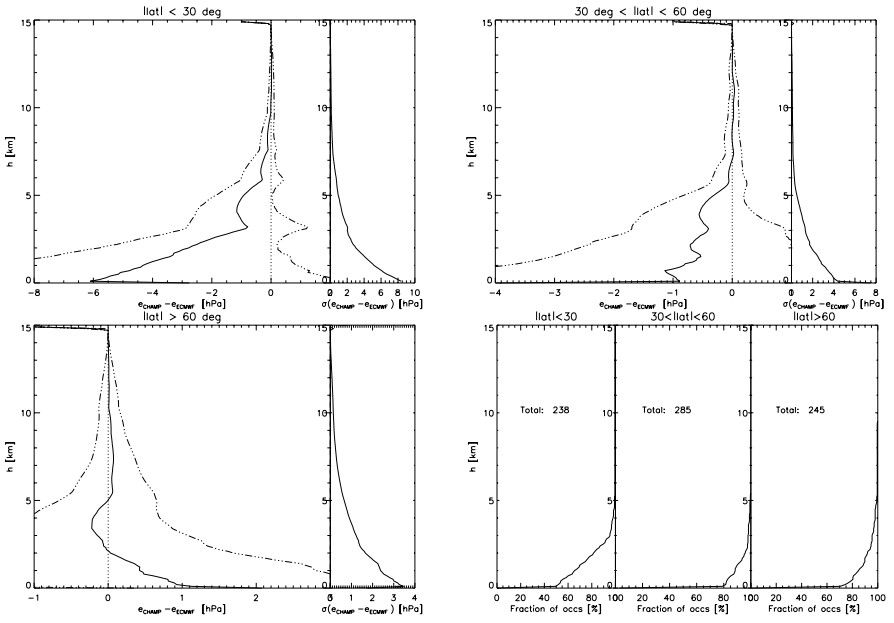

Fig. 3. Upper panels and lower left: Mean water vapour pressure difference as compared to ECMWF in the 3 latitude bands. Line styles as in fig. 2. Lower right panel: penetration depth in the 3 latitude bands.

Statistical comparison of the derived water vapour profiles to the humidity profiles from ECMWF reveals (fig. 3) a significant average difference below 5 km, especially at low latitudes. Here also a large standard deviation is calculated which is of comparable size to the average difference, which implies a significant bias. At high latitudes the average difference is below 1 hPa, shifting from negative to positive around 2 km. The mid-latitudes show an increasing average difference, ending around 1 hPa at the surface.

4 Discussion and conclusions

The average temperature difference is close to or below 1 K throughout the lower part of the stratosphere, only increasing in case of water vapour or problems in the upper boundary initialisation. This result is comparable to corresponding procedures performed on GPS/MET observations [6][plate 11].

Variations are found with latitude in the water vapour statistics, the low latitude occultations having the largest average difference and standard deviation, −6 and 9 hPa respectively near the surface. This relatively large error needs further investigation but could arise from measuring in a very moist region where the vater vapour partial pressure can be high, and atmospheric multipath phenomena can occur and cause interpretation problems of the measured excess phase.

The penetration depth of the occultations looks promising but is partly the result of the use of fly-wheeling in the receiver in case of loss of phase lock. In this situation the receiver continues to give an output based on extrapolation from the last sample with phase lock. In case of fly-wheeling the SNR is very low, which indicates that SNR-wheighting should be used in the inversion. In the equatorial region the tracking is, as expected due to expected large humidity gradients, more often lost before the ground is reached (see fig. 3 lower right panel).

5 Acknowledgment

This work was funded by the Danish National Science Foundation under the ESA follow-up research programme. The author wish to thank B. Amstrup for the ECMWF data preparation and G.B. Larsen for rewarding comments.

References

1. Bevis, M., Businger, S., and Chiswell, S. (1994). GPS Meteorology: Mapping Zenith Wet Delay onto Precipitable Water. *Journal of Applied Meteorology*, 33:379–386.
2. Gorbunov, M. E. and Sokolovskiy, S. V. (1993). Remote sensing of refractivity from space for global observations of atmospheric parameters. Technical Report 119, Max-Planck-Institut für Meteorologie.
3. Høeg, P., Larsen, G. B., Benzon, H.-H., Grove-Rasmussen, J., Syndergaard, S., Mortensen, M. D., Christensen, J., and Schultz, K. (1998). GPS Atmosphere Profiling Methods and Error Assessments. Technical Report 98-7, DMI. ISBN: 87-7478-374-2.
4. Melbourne, W. G., Davis, E. S., Duncan, C. B., Hajj, G. A., Hardy, K. R., Kursinski, E. R., Meehan, T. K., Young, L. E., and Yunck, T. P. (1994). The Application of Spaceborne GPS to atmosphere Limb Sounding and Global Change Monitoring. Technical Report 94-18, JPL, NASA.

5. Palmer, P., Barnett, J., Eyre, J., and Healy, S. (2000). A nonlinear optimal estimation inverse method for radio occultation measurements of temperature, humidity and surface pressure. *JGR*, 105(D13):17,513–17,526.
6. Rocken, C., Anthes, R., Exner, M., Hunt, D., Sokolovskiy, S., Ware, R., Gorbunov, M., Schreiner, W., Feng, D., Herman, B., Kuo, Y.-H., and Zou, X. (1997). Analysis and validation of GPS/MET data in the neutral atmosphere. *JGR*, 102(D25):29,849–29,866.
7. Thayer, G. (1974). An improved equation for the radio refractive index of air. *Radio Science*, 9(10):803–807.
8. Wickert, J., Reigber, C., Beyerle, G., König, R., Marquardt, C., Schmidt, T., Grunwald, L., Galas, R., Meehan, T. K., Melbourne, W. G., and Hocke, K. (2001). Atmosphere sounding by GPS radio occultation: First results from CHAMP. *GRL*, 28(17):3263–3266.

DANISH METEOROLOGICAL INSTITUTE

Scientific Reports

Scientific reports from the Danish Meteorological Institute cover a variety of geophysical fields, i.e. meteorology (including climatology), oceanography, subjects on air and sea pollution, geomagnetism, solar-terrestrial physics, and physics of the middle and upper atmosphere.

Reports in the series within the last five years:

No. 97-1
E. Friis Christensen og C. Skøtt: Contributions from the International Science Team. The Ørsted Mission - a pre-launch compendium

No. 97-2
Alix Rasmussen, Sissi Kiilsholm, Jens Havskov Sørensen, Ib Steen Mikkelsen: Analysis of tropospheric ozone measurements in Greenland: Contract No. EV5V-CT93-0318 (DG 12 DTEE):
DMI's contribution to CEC Final Report Arctic Trophospheric Ozone Chemistry ARCTOC

No. 97-3
Peter Thejll: A search for effects of external events on terrestrial atmospheric pressure: cosmic rays

No. 97-4
Peter Thejll: A search for effects of external events on terrestrial atmospheric pressure: sector boundary crossings

No. 97-5
Knud Lassen: Twentieth century retreat of sea-ice in the Greenland Sea

No. 98-1
Niels Woetman Nielsen, Bjarne Amstrup, Jess U. Jørgensen: HIRLAM 2.5 parallel tests at DMI: sensitivity to type of schemes for turbulence, moist processes and advection

No. 98-2
Per Høeg, Georg Bergeton Larsen, Hans-Henrik Benzon, Stig Syndergaard, Mette Dahl Mortensen: The GPSOS project
Algorithm functional design and analysis of ionosphere, stratosphere and troposphere observations

No. 98-3
Mette Dahl Mortensen, Per Høeg: Satellite atmosphere profiling retrieval in a nonlinear troposphere
Previously entitled: Limitations induced by Multipath

No. 98-4
Mette Dahl Mortensen, Per Høeg: Resolution properties in atmospheric profiling with GPS

No. 98-5
R.S. Gill and M. K. Rosengren: Evaluation of the Radarsat imagery for the operational mapping of sea ice around Greenland in 1997

No. 98-6
R.S. Gill, H.H. Valeur, P. Nielsen and K.Q. Hansen: Using ERS SAR images in the operational mapping of sea ice in the Greenland waters: final report for ESA-ESRIN's: pilot projekt no. PP2.PP2.DK2 and 2nd announcement of opportunity for the exploitation of ERS data projekt No. AO2..DK 102

No. 98-7
Per Høeg et al.: GPS Atmosphere profiling methods and error assessments

No. 98-8
H. Svensmark, N. Woetmann Nielsen and A.M. Sempreviva: Large scale soft and hard turbulent states of the atmosphere

No. 98-9
Philippe Lopez, Eigil Kaas and Annette Guldberg: The full particle-in-cell advection scheme in spherical geometry

No. 98-10
H. Svensmark: Influence of cosmic rays on earth's climate

No. 98-11
Peter Thejll and Henrik Svensmark: Notes on the method of normalized multivariate regression

No. 98-12
K. Lassen: Extent of sea ice in the Greenland Sea 1877-1997: an extension of DMI Scientific Report 97-5

No. 98-13
Niels Larsen, Alberto Adriani and Guido DiDonfrancesco: Microphysical analysis of polar stratospheric clouds observed by lidar at McMurdo, Antarctica

No.98-14
Mette Dahl Mortensen: The back-propagation method for inversion of radio occultation data

No. 98-15
Xiang-Yu Huang: Variational analysis using spatial filters

No. 99-1
Henrik Feddersen: Project on prediction of climate variations on seasonel to interannual timescales (PROVOST) EU contract ENVA4-CT95-0109: DMI contribution to the final report: Statistical analysis and post-processing of uncoupled PROVOST simulations

No. 99-2
Wilhelm May: A time-slice experiment with the ECHAM4 A-GCM at high resolution: the experimental design and the assessment of climate change as compared to a greenhouse gas experiment with ECHAM4/OPYC at low resolution

No. 99-3
Niels Larsen et al.: European stratospheric monitoring stations in the Artic II: CEC Environment and Climate Programme Contract ENV4-CT95-0136. DMI Contributions to the project

No. 99-4
Alexander Baklanov: Parameterisation of the deposition processes and radioactive decay: a review and some preliminary results with the DERMA model

No. 99-5
Mette Dahl Mortensen: Non-linear high resolution inversion of radio occultation data

No. 99-6
Stig Syndergaard: Retrieval analysis and methodologies in atmospheric limb sounding using the GNSS radio occultation technique

No. 99-7
Jun She, Jacob Woge Nielsen: Operational wave forecasts over the Baltic and North Sea

No. 99-8
Henrik Feddersen: Monthly temperature forecasts for Denmark - statistical or dynamical?

No. 99-9
P. Thejll, K. Lassen: Solar forcing of the Northern hemisphere air temperature: new data

No. 99-10
Torben Stockflet Jørgensen, Aksel Walløe Hansen: Comment on "Variation of cosmic ray flux and global coverage - a missing link in solar-climate relationships" by Henrik Svensmark and Eigil Friis-Christensen

No. 99-11
Mette Dahl Meincke: Inversion methods for atmospheric profiling with GPS occultations

No. 99-12
Hans-Henrik Benzon; Laust Olsen; Per Høeg: Simulations of current density measurements with a Faraday Current Meter and a magnetometer

No. 00-01
Per Høeg; G. Leppelmeier: ACE - Atmosphere Climate Experiment

No. 00-02
Per Høeg: FACE-IT: Field-Aligned Current Experiment in the Ionosphere and Thermosphere

No. 00-03
Allan Gross: Surface ozone and tropospheric chemistry with applications to regional air quality modeling. PhD thesis

No. 00-04
Henrik Vedel: Conversion of WGS84 geometric heights to NWP model HIRLAM geopotential heights

No. 00-05
Jérôme Chenevez: Advection experiments with DMI-Hirlam-Tracer

No. 00-06
Niels Larsen: Polar stratospheric clouds microphysical and optical models

No. 00-07
Alix Rasmussen: "Uncertainty of meteorological parameters from DMI-HIRLAM"

No. 00-08
A.L. Morozova: Solar activity and Earth's weather. Effect of the forced atmospheric transparency changes on the troposphere temperature profile studied with atmospheric models

No. 00-09
Niels Larsen, Bjørn M. Knudsen, Michael Gauss, Giovanni Pitari: Effects from high-speed civil traffic aircraft emissions on polar stratospheric clouds

No. 00-10
Søren Andersen: Evaluation of SSM/I sea ice algorithms for use in the SAF on ocean and sea ice, July 2000

No. 00-11
Claus Petersen, Niels Woetmann Nielsen: Diagnosis of visibility in DMI-HIRLAM

No. 00-12
Erik Buch: A monograph on the physical oceanography of the Greenland waters

No. 00-13
M. Steffensen: Stability indices as indicators of lightning and thunder

No. 00-14
Bjarne Amstrup, Kristian S. Mogensen, Xiang-Yu Huang: Use of GPS observations in an optimum interpolation based data assimilation system

No. 00-15
Mads Hvid Nielsen: Dynamisk beskrivelse og hydrografisk klassifikation af den jyske kyststrøm

No. 00-16
Kristian S. Mogensen, Jess U. Jørgensen, Bjarne Amstrup, Xiaohua Yang and Xiang-Yu Huang: Towards an operational implementation of HIRLAM 3D-VAR at DMI

No. 00-17
Sattler, Kai; Huang, Xiang-Yu: Structure function characteristics for 2 meter temperature and relative humidity in different horizontal resolutions

No. 00-18
Niels Larsen, Ib Steen Mikkelsen, Bjørn M. Knudsen m.fl.: In-situ analysis of aerosols and gases in the polar stratosphere. A contribution to THESEO. Environment and climate research programme. Contract no. ENV4-CT97-0523. Final report

No. 00-19
Amstrup, Bjarne: EUCOS observing system experiments with the DMI HIRLAM optimum interpolation analysis and forecasting system

No. 01-01
V.O. Papitashvili, L.I. Gromova, V.A. Popov and O. Rasmussen: Northern polar cap magnetic activity index PCN: Effective area, universal time, seasonal, and solar cycle variations

No. 01-02
M.E. Gorbunov: Radioholographic methods for processing radio occultation data in multipath regions

No. 01-03
Niels Woetmann Nielsen; Claus Petersen: Calculation of wind gusts in DMI-HIRLAM

No. 01-04
Vladimir Penenko; Alexander Baklanov: Methods of sensitivity theory and inverse modeling for estimation of source parameter and risk/vulnerability areas

No. 01-05
Sergej Zilitinkevich; Alexander Baklanov; Jutta Rost; Ann-Sofi Smedman, Vasiliy Lykosov and Pierluigi Calanca: Diagnostic and prognostic equations for the depth of the stably stratified Ekman boundary layer

No. 01-06
Bjarne Amstrup: Impact of ATOVS AMSU-A radiance data in the DMI-HIRLAM 3D-Var analysis and forecasting system

No. 01-07
Sergej Zilitinkevich; Alexander Baklanov: Calculation of the height of stable boundary layers in operational models

No. 01-08
Vibeke Huess: Sea level variations in the North Sea – from tide gauges, altimetry and modelling

No. 01-09
Alexander Baklanov and Alexander Mahura: Atmospheric transport pathways, vulnerability and possible accidental consequences from nuclear risk sites: methodology for probabilistic atmospheric studies

No. 02-01
Bent Hansen Sass and Claus Petersen: Short range atmospheric forecasts using a nudging procedure to combine analyses of cloud and precipitation with a numerical forecast model

No. 02-02
Erik Buch: Present oceanographic conditions in Greenland waters

No. 02-03
Bjørn M. Knudsen, Signe B. Andersen and Allan Gross: Contribution of the Danish Meteorological Institute to the final report of SAMMOA. CEC contract EVK2-1999-00315: Spring-to.-autumn measurements and modelling of ozone and active species

No. 02-04
Nicolai Kliem: Numerical ocean and sea ice modelling: the area around Cape Farewell (Ph.D. thesis)

No. 02-05
Niels Woetmann Nielsen: The structure and dynamics of the atmospheric boundary layer

No. 02-06
Arne Skov Jensen, Hans-Henrik Benzon and Martin S. Lohmann: A new high resolution method for processing radio occultation data

No. 02-07
Per Høeg and Gottfried Kirchengast: ACE+: Atmosphere and Climate Explorer

No. 02-08
Rashpal Gill: SAR surface cover classification using distribution matching

No. 02-09
Kai Sattler, Jun She, Bent Hansen Sass, Leif Laursen, Lars Landberg, Morten Nielsen og Henning S. Christensen: Enhanced description of the wind climate in Denmark for determination of wind resources: final report for 1363/00-0020: Supported by the Danish Energy Authority

No. 02-10
Michael E. Gorbunov and Kent B. Lauritsen: Canonical transform methods for radio occultation data

No. 02-11
Kent B. Lauritsen and Martin S. Lohmann: Unfolding of radio occultation multipath behavior using phase models

No. 02-12
Rashpal Gill: SAR ice classification using fuzzy screening method

No. 02-13
Kai Sattler: Precipitation hindcasts of historical flood events

No. 02-14
Tina Christensen: Energetic electron precipitation studied by atmospheric x-rays

No. 02-15
Alexander Mahura and Alexander Baklanov: Probablistic analysis of atmospheric transport patterns from nuclear risk sites in Euro-Arctic Region

No. 02-16
A. Baklanov, A. Mahura, J.H. Sørensen, O. Rigina, R. Bergman: Methodology for risk analysis based on atmospheric dispersion modelling from nuclear risk sites

No. 02-17
A. Mahura, A. Baklanov, J.H. Sørensen, F. Parker, F. Novikov K. Brown, K. Compton: Probabilistic analysis of atmospheric transport and deposition patterns from nuclear risk sites in russian far east

No. 03-01
Hans-Henrik Benzon, Alan Steen Nielsen, Laust Olsen: An atmospheric wave optics propagator, theory and applications

No. 03-02
A.S. Jensen, M.S. Lohmann, H.-H. Benzon and A.S. Nielsen: Geometrical optics phase matching of radio occultation signals

No. 03-03
Bjarne Amstrup, Niels Woetmann Nielsen and Bent Hansen Sass: DMI-HIRLAM parallel tests with upstream and centered difference advection of the moisture variables for a summer and winter period in 2002

No. 03-04
Alexander Mahura, Dan Jaffe and Joyce Harris: Identification of sources and long term trends for pollutants in the Arctic using isentropic trajectory analysis

No. 03-05
Jakob Grove-Rasmussen: Atmospheric Water Vapour Detection using Satellite GPS Profiling

No. 03-06
Bjarne Amstrup: Impact of NOAA16 and NOAA17 ATOVS AMSU-A radiance data in the DMI-HIRLAM 3D-VAR analysis and forecasting system - January and February 2003